Gate-tunable Scanning Tunneling Microscope as a tool for performing single-molecule chemistry

Thèse N° 7557

Présentée le 19 septembre 2019

à la Faculté des sciences de base
Laboratoire de science à l'échelle nanométrique
Programme doctoral en science et génie des matériaux

pour l'obtention du grade de Docteur ès Sciences

par

Shai MANGEL

Acceptée sur proposition du jury

Prof. J. Brugger, président du jury
Prof. K. Kern, directeur de thèse
Prof. T. Weitz, rapporteur
Dr T. Kumagai, rapporteur
Prof. . H. Brune, rapporteur

2019

ÉCOLE POLYTECHNIQUE
FÉDÉRALE DE LAUSANNE

Contents:

List of figures:

List of acronyms:

STM- Scanning Tunneling Microscope

AFM- Atomic Force Microscope

EEF- External electric field

G:FET- Graphene Field Effect Transistor

SPM-Scanning probe microscope

DOS- Density of states

STS- Scanning tunneling spectroscopy

IETS- Inelastic tunneling spectroscopy

NDR- Negative differential resistance

CVD- Chemical vapor deposition

HOPG- Highly oriented pyrolytic graphite

UHV-Ultra High Vacuum

FFT- Fast Fourier Transform

PMMA- poly methyl methacrylate

APS- ammonium persulfate

H_2Pc- free-base phthalocyanine

HOMO-Highest occupied molecular orbital

LUMO- Lowest unoccupied molecular orbital

RTN- Random telegraphic noise

DFT- Density function theory

ROI- Region of interest

"Science, like the Mississippi, begins in a tiny rivulet in the distant forest. Gradually other streams swell its volume. And the roaring river that bursts the dikes is formed from countless sources."

Abraham Flexner, 1939

Abstract:

The ability to interrogate single molecules at the atomic scale is a fundamental necessity for constructing the molecularly based electronics of the future. Especially of interest is the ability to tune the relevant chemical reactions by applying an external perturbation to the system. Such perturbations may include the influence of an external electric-field (EEF) or electrostatic doping with a backgate voltage. An excellent tool to perform these feats is the scanning tunneling microscope (STM), which enables characterization with atomic-scale spatial resolution and is able to produce a highly oriented EEF due to its super-fine tip apex. The tip-induced EEF can be altered by modifying the tip-sample distance. To separate the tip movement from other parameters, one can combine an STM and a graphene-based field effect transistor (G-FET). This enables one to not only tune the tip-sample distance in an autonomous way but also electrostatically dope the system in a reversible manner. In the following thesis we will demonstrate our capability to probe and manipulate single molecule chemistry by using two separate methods that utilize the full potential of our setup. The first method allows us to alter the tip-induced electric field by turning the feedback loop off after applying the gate voltage, which subsequently modifies the tip-sample distance due to the change in the sample local density of states. This was used to control the tautomerization reaction of free-base phthalocyanine (H_2Pc) molecules. An applied back-gate voltage tunes the tip-induced electric field, which modifies the activation barrier for tautomerization. The electric field effect was correlated to the molecular orientation and tilting angle of the molecules. Our findings were in excellent agreement with density function theory calculations. The second method enables us to control the doping levels of the surface by turning the feedback loop off before applying the gate voltage, which leaves the tip-sample distance fixed throughout a measurement, and allows us to observe the effects that follow from only charging the surface. This method was used to tune the bond length of hydrogen molecules physisorbed on top of a graphene surface. The accumulated charge changes the interaction of the hydrogen molecules with the surface, we were able to increase or decrease the bond length as a function of gate voltage. The analysis of this system was facilitated by employing both the Baratoff-Persson and the Gupta models. The work presented here unveils our device's unique capabilities and demonstrate our abilities to not only measure but also perform and manipulate chemical reactions at the atomic scale.

Keywords: Scanning tunneling microscope, G-FET, Gate-STM, tip-induced electric field, surface doping, tautomerization, free-base phthalocyanine, molecular hydrogen, bond length modification

Zusammenfassung:

Die Fähigkeit einzelne Moleküle auf der Skala einzelner Atome zu untersuchen, ist eine grundlegende Notwendigkeit für die Erschaffung zukünftiger molekülbasierter Elektronik. Insbesondere die Möglichkeit relevante chemische Reaktionen durch externe Anregungen zu beeinflussen ist von großem Interesse. Beispiele dieser Anregungen sind externe elektrische Felder (EEF) oder elektrostatisches Dotieren mit Hilfe einer Gate-Spannung. Ein exzellentes Werkzeug für diese Experimente ist das Rastertunnelmikroskop (STM). Es ermöglicht atomare räumliche Auflösung und aufgrund seiner sehr scharfen Spitze stark gerichtete EEF. Spitzeninduzierte EEF können durch den Spitze-Probe Abstand variiert werden. Um Änderungen dieses Abstandes von anderen Parametern zu trennen, kann ein STM kombiniert mit einem auf Graphen basierten Feldeffekttransistor (G-FET) verwendet werden. Dies ermöglicht nicht nur die unabhängige Änderung des Spitze-Probe Abstandes, sondern auch eine reversible elektrostatische Dotierung. In dieser Arbeit demonstrieren wir die Möglichkeit, auf zwei unabhängigen Methoden basierend, die Chemie einzelner Moleküle zu messen und zu manipulieren. Die erste Methode ermöglicht es uns, das spitzeninduzierte EEF zu verändern, indem die Rückkopplung des Spitze-Probe Abstandes abgeschaltet wird, nachdem die Gate-Spannung angelegt wurde, welche aufgrund ihres Einflusses auf die lokale Zustandsdichte den Spitze-Probe Abstand verändert. Dies wurde verwendet, um die Tautomerationsreaktion von Phthalocyanin (H_2Pc) Molekülen zu kontrollieren. Eine an das Gate angelegte Spannung verändert das spitzeninduzierte elektrische Feld, welches die Aktivierungsenergie der Tautomerisierung verändert. Der elektrische Feldeffekt konnte mit der Orientierung und dem Neigungswinkel der Moleküle korreliert werden. Unsere Ergebnisse zeigen eine ausgezeichnete Übereistimmung mit Dichtefunktionaltheorie-Rechnungen. Das zweite Verfahren gibt uns Kontrolle über die Dotierungslevel der Oberfläche, indem die Rückkopplung ausgeschaltet wird, bevor die Gate-Spannung angelegt wird. Hierdurch ist der Spitze-Probe Abstand während der gesamten Messung konstant und wir können Effekte beobachten, die nur auf die Ladung der Oberflache zurückzuführen sind. Mit dieser Methode haben wir die Bindungslängen von auf einer Graphenoberfläche physisorbierten Wasserstoffmolekülen verändert. Die angesammelte Ladung ändert die Interaktion der Wasserstoffmoleküle mit der Oberflache und wir konnten die Bindungslänge in Abhängigkeit der Gate-Spannung verkürzen oder verlängern. Die Analyse des Systems wurde anhand des Baratoff-Persson und des Gupta-Modells durchgeführt. Die hier präsentierte Arbeit zeigt die einzigartigen Möglichkeiten, die unser experimenteller Aufbau eröffnet und demonstriert, dass wir fähig sind, chemische Reaktionen nicht nur auf atomarer Größenskala zu messen, sondern auch zu manipulieren.

Schlüsselwörter: Rastertunnelmikroskopie, G-FET, Gate-STM, spitzeninduziertes elektrisches Feld, Oberflächendotierung, Tautomerisierung, Phthalocyanin, molekularer Wasserstoff, Bindungslängenmodifikation

Chapter1:

Introduction:

As the size of electronic device components and integrated circuits continue to miniaturize according to Moore's law, one can assume that they will eventually converge towards molecular based electronics. Single molecule electronics can be broadly described as any electronic device which leverages the manifest properties of single molecules for its functionality. This idea was first promulgated by Feynman in 1959 at the annual meeting of the American Physical Society at Caltech. He suggested that atoms and molecules can be used to construct electronic devices, and could even eventually replace the technology at that time. Since then, leaps of progress have been made in the design and fabrication of molecular-based devices. Prominent examples now include molecular transport, where an electrical charge is transported through a molecular-based channel [1-3], molecular sensors, which are able to detect and indicate with sensitivity and specificity at the molecular scale [4,5], and molecular storage devices and spintronics, which now exhibit unprecedented high-density data storage capabilities [6-8]. Albeit, in order to construct devices at the nanoscale that can act as integrated components for future devices, further and deeper understanding of the physics and chemistry on the scale of single molecules is needed.

One of the tools available to glean such insight is the Scanning Tunneling Microscope (STM). The STM was first introduced in 1982 by Binning and Rohrer [9-11], and quickly followed by the development of the Atomic Force Microscope (AFM) in 1986 [12]. STM enables the probing of electronic structure on a local level at unprecedented atomic resolution, while AFM enables the probing of nonconductive materials. Furthermore, it has been shown that AFM can also be used to image atomic bonds with exceptional spatial resolution [13,14]. The use of surface sensitive techniques with atomic resolution not only allows one to manipulate molecules at will, but also activate reactions with local control. One can also alter the molecule's environment by manipulating atoms and adjacent molecules nearby [15-17]. This ability allows one to explore in detail the relationship between an adsorbed molecule and its local environment. As an example, Kügel et al. have shown that by placing a single silver atom at various positions around an H_2Pc molecule, the stability of its two tautomers and their switching rate could be tuned. In another experiment, Liljeroth et al. demonstrated the coupling between several naphthalocyanine molecules. By using STM, they were

able to place three molecules next to each other and induce switching at one target molecule by injecting electrons into an adjacent molecule.

The ability to study single molecule chemistry is crucial for understanding phenomena unique to nanoscale systems. STM enables characterization of these systems because spectroscopic measurements can be performed with spatial resolution at the nanoscale and combined together with topographic imaging. Since the fundamentals of chemistry are rooted in the electronic interactions between atoms and molecules, the ability to observe them by directly measuring their electronic and vibrational states [18-20], conformation change [21,22], energy transfer [23] and electrical conductivity [24,25] at atomic resolution is invaluable. Moreover, it is expected that one can manipulate or control a reaction through modification of its electronic structure by applying a strong, oriented electric field. We will segue into how electric fields affect chemical reactions with some examples.

Electric fields have always been involved in catalyzing an array of reactions as its presence can reduce the energy of intermediate states along a reaction pathway. A prominent example is the stabilization of intermediate ionic structures of certain enzymes through organization of polar groups which electrostatically catalyze the reaction [26,27]. Another example of a naturally used electric field was shown recently in the unidirectional proton transfer of photosynthesis [28]. However, in order to truly understand the effect of a highly oriented external electric field (EEF) on a molecule, one should have a thorough insight into the molecule's orientations. This is of the utmost importance because the stabilization of intermediate states by an EEF is mainly based on the interaction between the EEF and molecule's dipole which depends on its orientation. Therefore STM, which allows us to define the exact orientation of a molecule, is an outstanding tool to study the effect of an EEF on chemical reactions. Furthermore, since the STM tip apex is atomically sharp, it offers an unprecedented possibility to generate a controllable, highly oriented EEF. This field can be used to promote various reactions at the single molecule level. As an example, Alemani et al. have demonstrated that the reversible isomerization reaction of azobenzene can be done on Au(111) by inducing strong electric field with voltage ramps at the tip [21]. Recently Pham et al. have shown that by doping graphene with N atoms they were able to shift the molecular levels of TCNQ molecules and perform a selective reduction of a single TCNQ molecule by using a tip-induced EEF [29] . In an STM setup, manipulation of the tip-induced electric field is executed by changing the tip-sample distance. However, in order to vary the tip-sample distance one also should change the set-point current or the bias-voltage. This situation makes the process of isolating and examining the influence of an electric field on a specific reaction extremely challenging to interpret. Therefore, in order to

disentangle the tip-sample distance from other set-point parameters (current and voltage) a gate-tunable STM was used.

In 2008 Zhang et al. presented for the first time, the combination of a gate-STM and a Graphene Field Effect Transistor (G-FET).[30] In this set-up one can apply a back gate voltage to a highly doped Si layer which is separated from the top graphene layer by an isolating thick SiO_2 layer. This structure acts as a plate capacitor, causing an accumulation or depletion of charge carriers at the graphene layer as function of the applied gate-voltage (an elaborated explanation is provided in *chapter 2.2.1*). In this seminal paper, Zhang et.al presented the ability to follow the shift in the graphene local density of states by tracking the movement of the graphene Dirac point across several spectra taken in different gate-voltages. The development of the gate-STM opened the door to a variety of experiments since it enables the operator to modify the electrostatic doping levels of the surface in situ. Several prominent examples of this modification include the ability to tuned the electronic structure of a single Co adatom by applying a back-gate voltage and reversibly ionized it [31], and the influence of charged impurities on the graphene electronic landscape as a function of spatial distance[32]. An occurring problem with the aforementioned system was the local inhomogeneous charging of the surface due to the surface corrugation and charge traps in the SiO_2 layer [33]. The solution for this problem was found in the form of integrating an underlying layer of the flat dielectric material hBN, which is shown to improve the surface charging substantially[34,35] [34]. This new configuration allowed to perform more elaborate experiments that exploit the new layered device properties such as the charging and discharging of inherent defects in the underlying hBN [36] or the ability to perform controlled pattering on the surface at the nanoscale [37]. Furthermore, by applying a gate-voltage of sufficient magnitude, one can shift the energetic bands of a molecule, charging it in the process [38,39].

In this thesis we will utilize the exceptional capabilities of our gate-STM by combing it with modified G-FET devices in order to perform single molecule experiments. In the work presented in *chapter 4* we will demonstrate how by tuning the local density of states of the graphene surface, we were able to change the tip-sample distance, thus, tune the tip-induced electric field independently of the current and bias voltage. We will show a direct influence of the electric field on the tautomerization process at base-free phthalocyanine molecules adsorbed on a graphene/SiO_2/Si device. In the work presented in *chapter 5* we will show by the use of a model system of molecular hydrogen on top of a graphene/hBN/SiO_2/Si device, our capabilities to tune the molecule's bond length by means of electrostatic doping of the surface. In *chapter 7* we will discuss our future plans to construct a new G-FET device, which is based on eliminating the presence of SiO_2 as the dielectric component, by

substituting it with atomically thin hBN layers. These methods enhance our field effect, which will allows us to induce stronger charging for the same bias voltage. Furthermore, by constructing several devices with dielectric layers at different thicknesses, we will be able correlate the exact amount of the induced charging and the tip movement to the insulting layers' thickness. We will also present some preliminary results from our recent experiments at the end of the chapter.

Chapter 2:

Theory:

2.1 Scanning tunneling microscope:

Due to the abrupt termination of material at the interface between the bulk and the environment, surfaces of materials differ from their bulk form in many important properties. In order to probe their unique properties, surface sensitive instruments were developed. The Scanning Tunneling Microscope (STM) was introduced in 1982 by G. Binnig and W. Rohrer at the IBM Research Laboratory, which resulted in them receiving the physics Nobel Prize in 1986 [11,40]. It was the first scanning probe microscope (SPM) that was sensitive to the local density of states (DOS) of a surface at the atomic scale. This development enabled not only the ability to probe the surface or any of its adsorbed topographic features, but also its electronic structure, and in some cases even manipulate such properties in a very localized way. Today, STM has expanded its applicability to even include characterizing the fluorescence and superconductivity of complex materials. Furthermore, in recent years, STM instruments have been combined with the atomic force microscope (AFM) so that complementary force mapping can now be done in conjunction with STM.

Since STM is the primary tool being used in the following thesis a brief introduction to its principals and modes of operation is provided.

2.1.1 Principals:

In our daily life which is governed by the rules of classical physics, when an object encounters a potential barrier with an energy higher than its own it is blocked and restricted from penetrating it. Not so in the case of the quantum realm, where objects with a small mass such as electrons possesses wave like properties and obey the Schrödinger equation, can penetrate such a potential. This phenomenon, called tunneling, is the basis upon which an STM operates. As an example, a one-dimensional electron with a wave function $\psi(z)$ and energy ε penetrating through a potential U will decay according to $\psi(z) = \psi(0)e^{-kz}$ (figure 2.1) where k is the wave-function decay constant. In an STM the same process also occurs, where the electron now travels from a metallic tip through a potential of an electrically insulating medium (such as vacuum or air) into a conductive sample,

under the influence of a bias voltage. Therefore one can describe the tunneling current as $I \propto e^{-2kz}$, where the decay constant is now defined by the surface work-function φ as $k = \frac{\sqrt{2m\varphi}}{\hbar}$ and z is the tip-sample separation distance. Due to the relationship between I and z, the measured current will change by an order of magnitude as the tip-sample separation distance (z) changes by only 1 Å. This sensitivity gives the STM its superb atomic resolution and surface sensitivity.

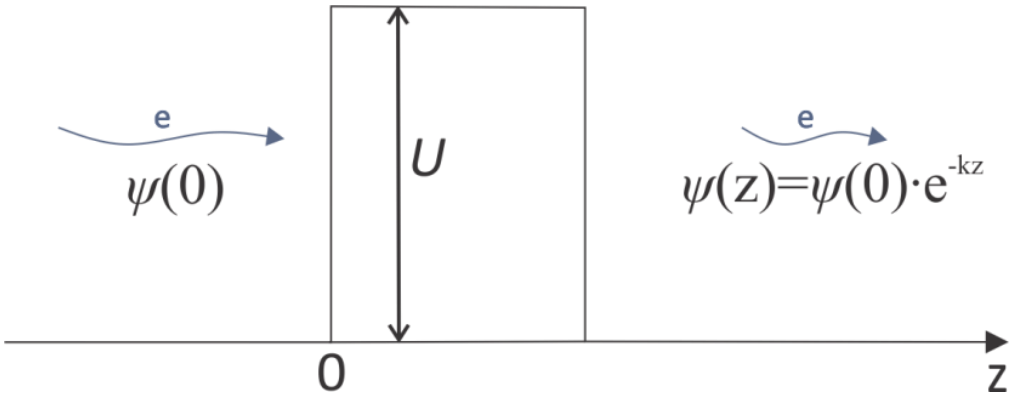

Figure 2.1: An illustration showing the tunneling process of an electron with a wave function $\psi(z)$ through a potential barrier U.

The first to provide a general expression for the tunneling current between two metals through a barrier was Bardeen [41], which can be described by[20,42]:

(2.1)

$$\mathrm{I} = \frac{4\pi\mathrm{e}}{\hbar}\int_0^{\mathrm{eV}} \rho_\mathrm{t}(\mathrm{E_F} - \mathrm{eV}_b + \varepsilon)\rho_\mathrm{s}(\mathrm{E_F} + \varepsilon)|\mathrm{M}|^2 \mathrm{d}\varepsilon$$

Here ρ_t and ρ_s are the densities of states of the tunneling tip and surface respectively, E_F the Fermi level, V_b the applied voltage and M is the tunneling matrix element between the tip and the surface, which by definition, depends on the electron's wave function. One should note that the process depicted in equation (2.1) is correct in the limits of low temperatures and small bias voltages and under the assumption of an elastic tunneling process, i.e. the energy possessed on the tip ε_t is equal to the energy it will possess after tunneling to the surface ε_s. A more elaborate explanation of an inelastic tunneling process will be provided in *chapter 2.1.2*.

In order to obtain a tunneling current, the tip is brought close to the surface by using a piezo-element until it reaches the tunneling regime ($d \leq 10$ Å). The sample is then scanned by the tip

while the tunneling current between the tip and sample is measured. The tip is located on another piezo-element which controls the tip movement along the z-direction with pm precision. The STM can typically operate in two main modes i.e. constant current and constant height. In the constant current mode, a feedback loop keeps the measured current at a specific set point by modifying the tip height throughout the scanning (using the aforementioned piezo-element). In constant height mode, the feedback loop is turned off and the tip is maintained at a specific height throughout the scanning while the current variations are recorded. Due to the sub-nanometric distance of the tunneling regime both modes (especially the constant height mode) demand a system that is mechanically and electronically stable. Therefore, it is necessary to isolate the system from any external interference, such as external vibrations or crosstalk originating from the measurement peripherals. A more detailed explanation of our instrument noise isolation is provided in *chapter 3.1*.

2.1.2 Scanning tunneling spectroscopy:

A more quantitative and experimentally compatible approach was suggested in 1983 by Tersoff-Hamann [20,42] who considered the case of a spherical tip terminated by a single atom which can then behave as an s-wave. By assuming the tunneling [4142]matrix element M is constant under the influence of an applied bias voltage [41] it can be taken out of the integral in *equation 2.1*. A second assumption is the tip's DOS is flat, therefore constant around the Fermi level. Therefore, any change in the tunneling current as a function of the bias voltage, i.e. the surface conductance, depends only on the surface DOS and can be derived from *equation 2.1* as:

(2.2)

$$\frac{dI}{dV_B} \propto \rho_s(E_F + eV, r_0)$$

This equation describes the proportional relationship between the measured differential conductance and the surface density of states, which allows one to probe the surface energy landscape by measuring the tunneling current as the bias voltage is swept. This is the basis for scanning tunneling spectroscopy (STS), which can be used for measuring various electronic and vibronic states of a sample or an adsorbent and will be used extensively throughout the following thesis. Since an important assumption is that the tip has a flat and homogenous DOS, a thorough and methodical procedure for preparing tips on a metallic surface is used and is provided in *chapter 3.3*.

Inelastic tunneling spectroscopy:

One of Bardeen's key assumptions is that the tunneling current is an elastic process. However, for some specific surfaces and molecules the tunneling process can also include a secondary channel that is of an inelastic nature. In an inelastic tunneling process the transmitted electron with sufficient energy loses some of its energy due to phononic interactions (as it shown for graphene in *chapter 2.2.2*) or due to excitation of specific molecular modes before tunneling to the surface (as it shown in details in chapter 5). Figure 2.2 shows an illustration of the elastic tunneling process (figure 2.2a) in which the electron is tunneled from the tip to the surface through the potential barrier without any energy lose and the inelastic tunneling process (figure 2.2b) in which the tunneled electron lose an energy in a magnitude of ΔE. Since the recorded tunneling current is an integral over all contributions up to the measured energy range, an opening of another tunneling channel (the inelastic channel) will manifest as an increase in the I(V) curve slope, and its differential conductivity will exhibit a symmetric "step-like" feature at the threshold of conductance (Figure 2.3 a and c respectively). Those specific transitions can be detected by using inelastic tunneling spectroscopy (IETS). This method is extremely sensitive [44]to even the slightest variations in the current signal [45].

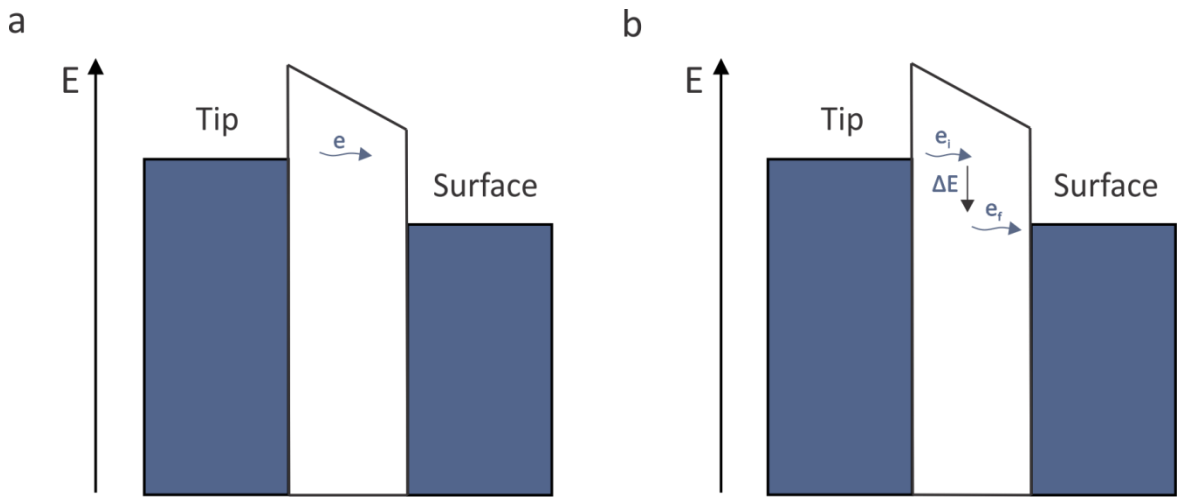

Figure 2.2: An illustration of a) elastic tunneling process and b) inelastic process in which the electron is tunneling from the tip to the surface through a potential barrier.

Saturated inelastic tunneling spectroscopy:

Usually in IETS the tunneling time between two consecutive electrons (t_I) is much longer than the lifetime of the excited state in the molecule (τ^*) i.e. $t_I \gg \tau^*$. Nevertheless, as it was previously reported [46,47] in some circumstances the excited state lifetime can be on the order of the tunneling current i.e. $t_I \approx \tau^*$, thus, an electron from the tip will not be able to tunnel into the occupied state due to the Pauli exclusion principle. Since the inelastic channel is saturated (hence the name saturated-IETS) its overall contribution to the total current will be diminished. Thus, the I(V) curve slope will exhibit a decrease in its slope.

Negative differential conductivity:

In some specific circumstances (which are related to the molecule's electronic structure) the presence of an inelastic channel can change the conductivity of the elastic channel. Thus, one can observe a decrease in current despite an increase in the voltage. Negative differential resistance (NDR) was observed first in an STM junction by In-Whan Lyo et al. over specific sites on boron-exposed silicon(111) surfaces [48]. The occurrence of NDR is usually ascribed to the excitation and relaxation of localized molecular vibration modes. When the conductance from the molecule's excited state (σ^*) is bigger than the conductance of its ground state (σ_g) i.e. $\sigma^* \gg \sigma_g$, the I(V) curve will show a small decrease (Figure 2.3b) and correspondingly the dI/dV curve will show dips in the threshold energies[49] (Figure 2.3d). This specific case is called negative differential conductivity. A more elaborate discussion and the different models describing the exact process are provided in *chapter 5*, where we observe a negative differential conductivity in molecular hydrogen physisorbed on our sample.

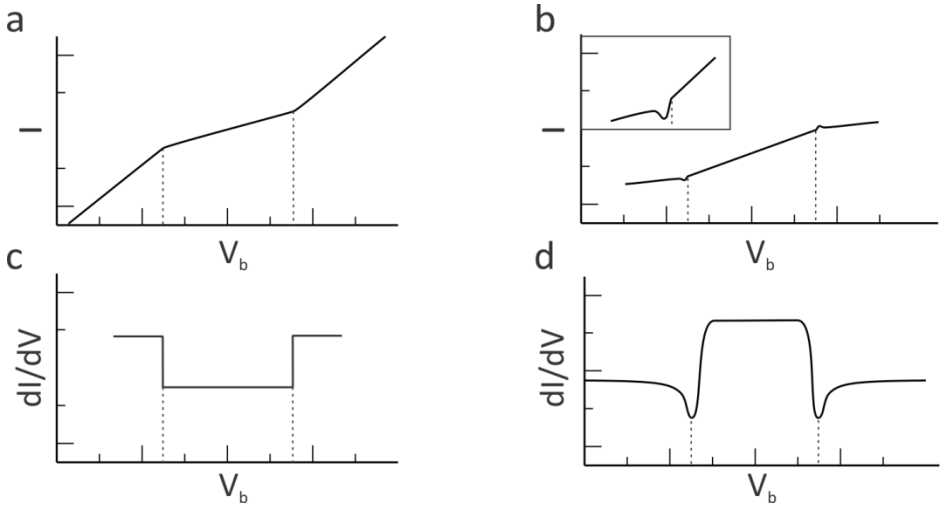

Figure 2.3: a) I(V) curve of an inelastic tunneling process, the increase in the current slope due to the opening of the inelastic channel is clear. b) I(V) curve of an NDR process. Inset: a magnification of the threshold area. c) A dI/dV curve of an inelastic tunneling process show the step-like increase at the threshold energies. d) A dI/dV curve of a negative conductance saturated process. The two dips in the threshold energies are shown.

2.2 Graphene theory:

Since all of the experiments in this work involve a graphene-FET based device, an overview of graphene and it unique properties and electronic structure is given.

Graphene is a single layer of carbon atoms arranged in a hexagonal structure and connected with σ-bonds through sp^2 orbitals with a bond length of 142pm. Graphene layers are known as the building blocks of graphite, which is constructed of several stacks of layers bonded by weak van der Waals interactions with an inter-planar spacing of 335pm [50] (figure 2.4). Although it was isolated for the first time in 2005 by Andre Geim and Konstantin Novoselov [51], its electronic structure was already predicted in the 40's through the use of tight binding theory [52]. Due to its unique electric properties, chemical stability and the fact that it can be modified by means of conventional lithography, graphene draws a lot of attention as an integral component of new electronic devices. Today, the most common methods to produce graphene are by chemical vapor deposition (CVD) on top of a metal thin sheet (usually Cu) or by mechanical exfoliation from highly oriented pyrolytic graphite (HOPG) using scotch tape. As mentioned above the electronic properties of graphene differ dramatically from the properties of graphite. In order to access its exceptionally high current density and mobility and understand how we can utilize them to our advantage, one should examine the graphene band structure and physics.

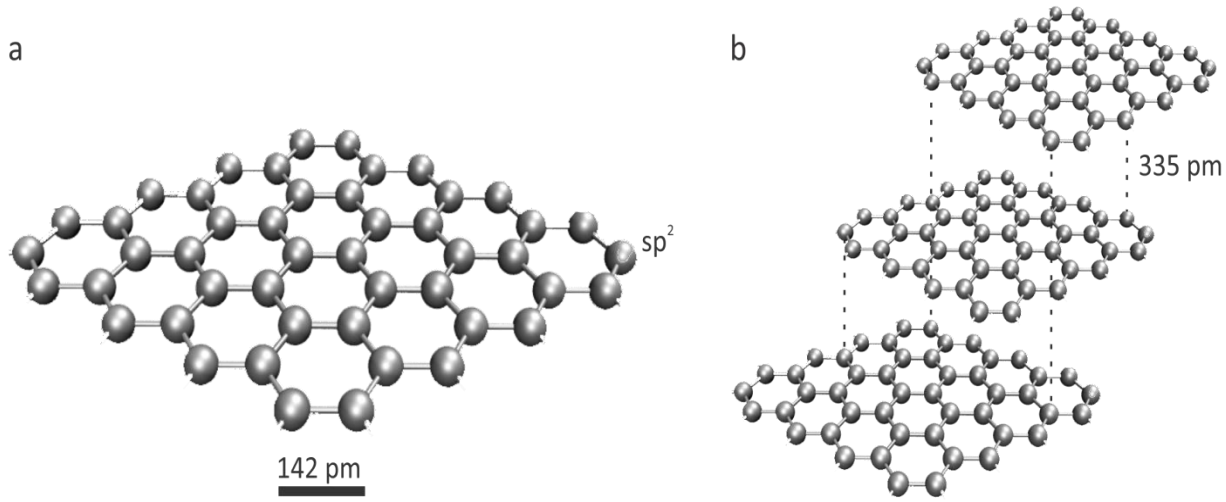

Figure 2.4: An illustration of a single atomic layer of graphene (a) and Graphite (b) constructed of several graphene layers interacting with each other through van der Waals interactions.

The graphene honeycomb structure is constructed from two sub-lattices which can be notated as A and B with the corresponding lattice vectors a_1, a_2 and δ_1, δ_2, δ_3 and its corresponding Brillouin zone can be described by using the reciprocal-lattice vectors b_1 and b_2 (figure 2.5a,b). The Brillouin zone of graphene has a six-fold symmetry, and the K and K' points located in its vertices are of particular importance. By using tight-binding theory one can calculate the graphene band structure E_k (figure 2.5c), which has a distinctive cone-like shape at the K and K' points (magnification in figure 2.5c). When expanding the full band structure around the K or K' points one can expect a dispersion of:

(2.5)

$$E_{\pm}(q) \approx \pm v_f|q| + O(\frac{q^2}{K^2})$$

where q is the electron momentum with respect to the Dirac point and v_f is the Fermi velocity taken as $V_f = 1.0 \cdot 10^6 \ \frac{m}{s}$ as it was first calculated by Wallace in 1947. That differs from what is usually observed by the fact that the Fermi velocity is independence of the energy or momentum, therefore the energy dispersion is linear. Furthermore, due to their unique energy dispersion the electrons located near the K and K' points can be described by the massless Dirac equation, thus the vicinity of those points called the Dirac cones.

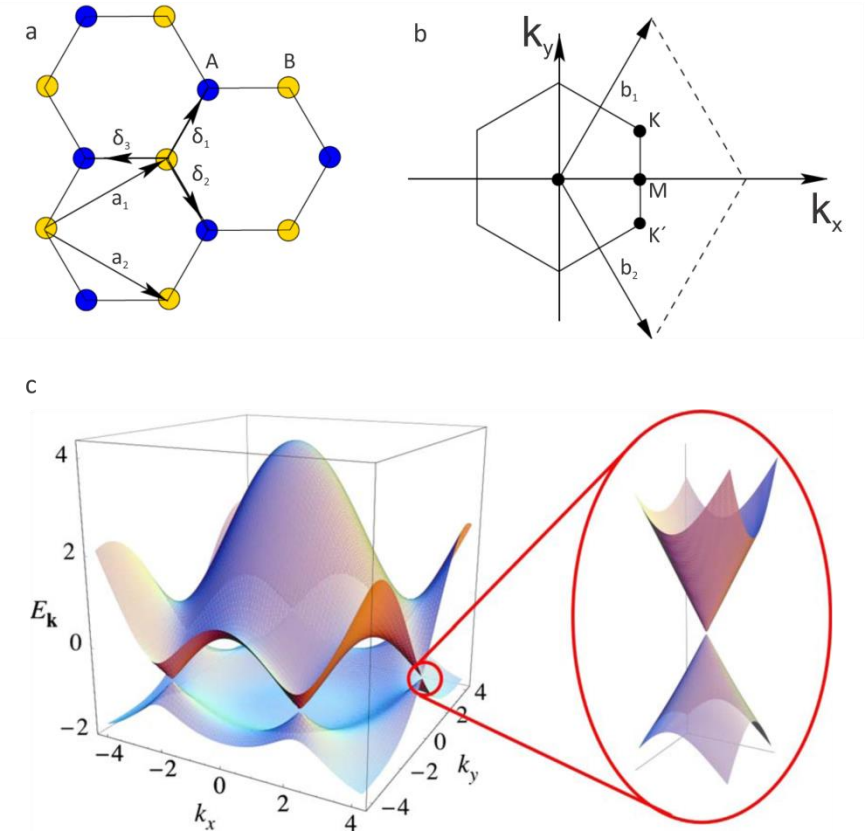

Figure 2.5: a) The graphene lattice structure constructed of the two sub-lattices A and B with the corresponding lattice unit vectors a_1, a_2 and δ_1, δ_2, δ_3. b) The corresponding Brillouin zone presenting K and K' points where the Dirac cones are located. c) The graphene electronic band structure with magnification of one of the Dirac cones [53].

2.2.1 STM on Graphene-FET:

A field effect transistor (FET) is defined as an electrical component which uses an induced electric field and an accompanied potential differential to modulate the current flow in a specific channel. A common FET device consists of 3 electrodes or terminals. Two of them (named source and drain) are connected via a semiconductor channel (figure 2.6a). The third electrode named the gate is separated from the channel by an insulating layer (thus forming a capacitor structure) and allows modification of the charge transport through the channel by changing the voltage differential. The structure of a typical graphene-FET (G-FET) is similar with the exception that instead of the semiconductor channel now it is graphene that connects the source to the drain (figure 2.6b). Since graphene is a single atom thick layer it presents unprecedented sensitivity to any change in its charge carrier density, which makes the G-FET device optimal for different sensing applications, and as we will show in the thesis, a unique platform for modulating surface reactions.

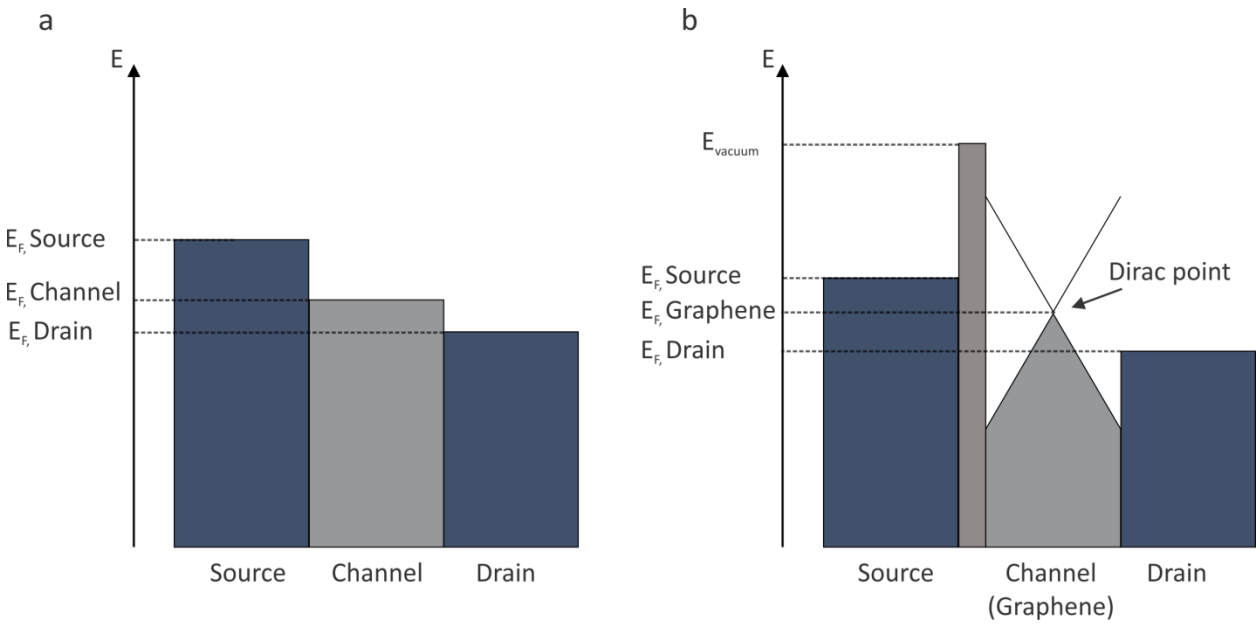

Figure 2.6: A schematic energy band diagram of a typical FET (left) and the analog graphene-FET (right). Applying gate voltage modified the channel Fermi energy thus modulate the current flow through it.

In the presented thesis we will use an STM compatible G-FET (figure 2.7). Here, the tip and the bias connection act as the source and drain in our system, and the graphene channel acts as the modulated channel. The graphene is separated from the bottom gate electrode by an isolating layer of approximately 300nm SiO_2. Applying a voltage to the gate electrode changes the number of the charge carriers in the highly doped Si, inducing charge accumulation on the Si/SiO_2 interface. That in turn causes an equivalent charge accumulation on the graphene channel, modifying it electronic landscape by electrostatic doping it, the process of which will be elaborated in the next segment. This apparatus allows us to manipulate surface reactions of molecules and single atoms adsorbed on the surface at the atomic level.

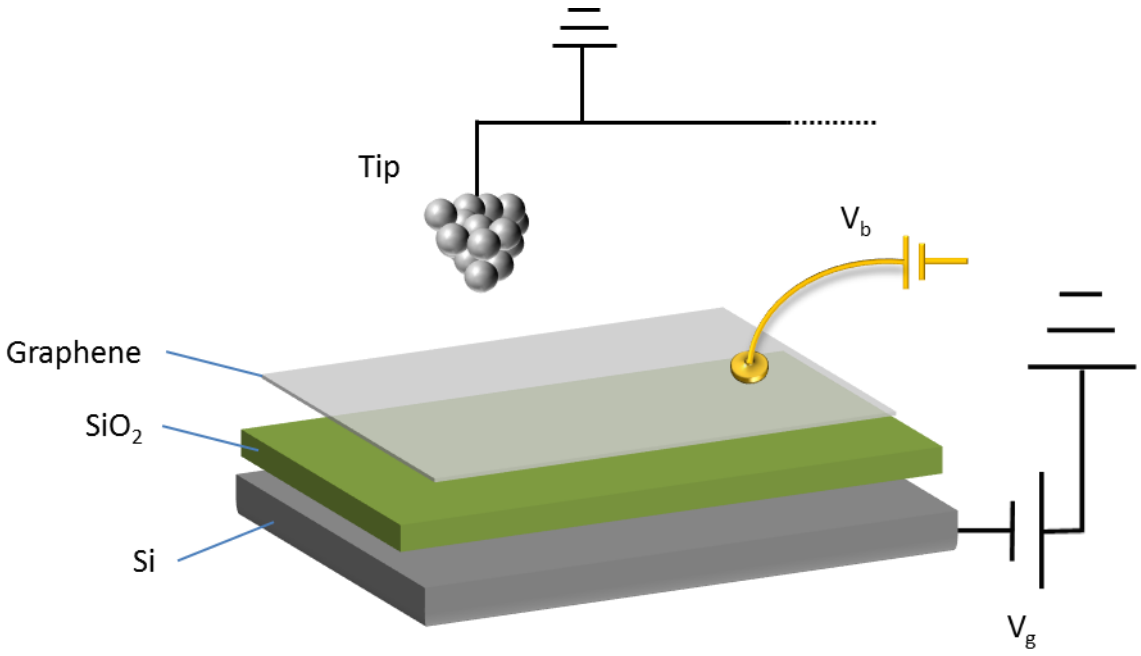

Figure 2.7: A schematic illustration of our G-FET device in an STM setup.

2.2.2 Graphene in an STM:

Since the energy dispersion of graphene next to the Dirac point can be described by *equation 2.5* in the vicinity of the K and K' points the DOS of graphene is proportional to its energy [50], therefore in the case of elastic tunneling one should expect a dI/dV spectrum taken on the graphene to be V-shaped (figure 2.8a). However, as it was shown in the past [30] due to considerations of momentum and energy conservation, we should expect a second order phonon-assisted inelastic tunneling process to dominant over the elastic process below a threshold of $\hbar\omega$ (figure 2.8b). In the latter, the tunneled electron will lose energy in the magnitude of $\hbar\omega \approx 65\ meV$ due to a transition from the σ^* state to an π state, resulting in a symmetric pseudo-bandgap in the center of the spectrum around, V_b=0 V, and the DOS will be shifted in $\pm\hbar\omega$. As it can be clearly seen, the minimum in the conductance (which is the Dirac point) is still expected to be observed in the spectrum but it will be slightly shifted due to the opening of the gap. As was expected, the pseudo-bandgap was observed in our spectroscopic measurements for both the graphene/SiO_2/Si and the graphene/hBN/SiO_2/Si devices.

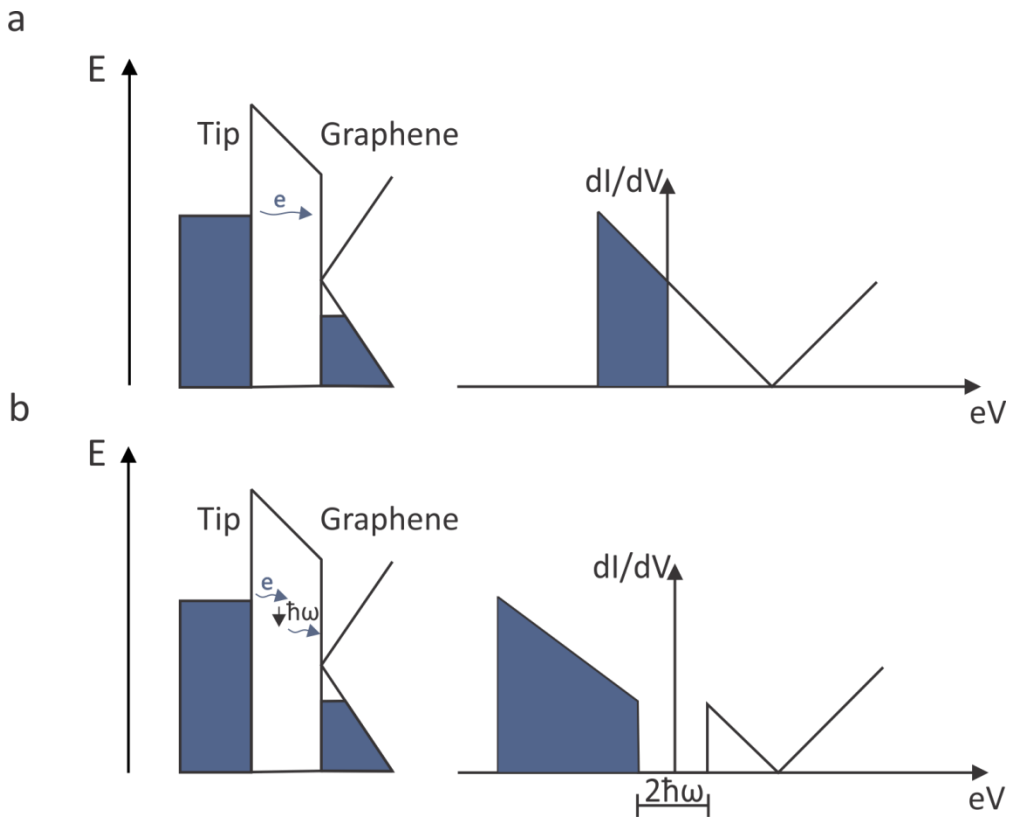

Figure 2.8: Elastic and inelastic tunneling processes into graphene. a) An elastic tunneling process in which the electron is tunneling from the tip into the graphene, due to the graphene's linear DOS the resulted dI/dV spectrum is V-shaped with a minimum in of the conductance at the Dirac point. b) An inelastic tunneling process in which the tunneled electron lose energy in the magnitude of $\hbar\omega$, resulting in a pseudo-bandgap at the magnitude of $2\hbar\omega$ centered around the Fermi level.

2.2.3 Electrostatic doping of Graphene:

Before utilizing our system, one should understand the behavior of the graphene channel under the influence of the gate voltage. In the case of an isolated graphene layer the Dirac points lie at the Fermi energy of the material. Applying a gate voltage allow us to electrostatically dope the graphene layer, thus shifting the Dirac point with respect to the Fermi energy (figure 2.9). As a positive voltage is applied to the gate electrode it will cause a charge accumulation on the interface between the doped Si and the SiO_2 interface, which causes negative charge carriers to accumulate on the graphene surface, which shifts the Dirac point below the initial Fermi level. The inverse process occurs when a negative gate voltage is applied (figure 2.9).

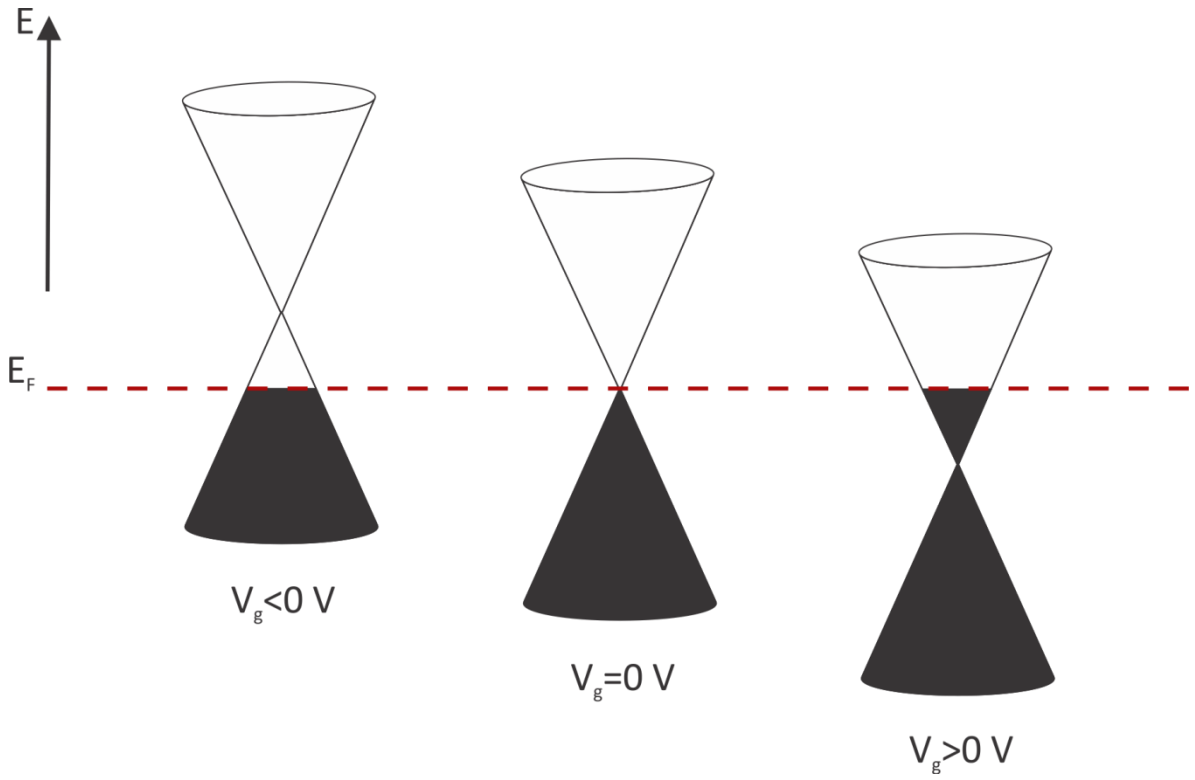

Figure 2.9: A schematic illustration presenting the DOS of graphene at different doping conditions. The Fermi level shifts with respect to the Dirac point as a function of the applied gate-voltage.

The change in the charge carrier density n in the graphene layer as a function of the gate voltage can be described through the relationship [53]:

(2.6)

$$n = \alpha V_g$$

Here α is the graphene charge carrier coupling coefficient for the gate voltage. Since the gate system can be viewed as a plate capacitor, the coupling coefficient can be described as [53,54]:

(2.7)

$$\alpha = \frac{\varepsilon_0 \varepsilon}{de}$$

Here ε_0 and ε_{SiO_2} are the vacuum and the SiO_2 permittivity constants respectively, e is the electron charge and d is the thickness of the dielectric material.

The energetic shift of the Dirac point with respect to the Fermi level $E_{D,}$ can be calculated through:

(2.8)

$$E_D = \hbar v_f \sqrt{\pi \alpha |V_g - V_0|}$$

Where $\hbar$ the reduced Planck constant, v_f is the Fermi velocity taken as $V_f = 1.0 \cdot 10^6 \ \frac{\mathrm{m}}{\mathrm{s}}$ and V_0 is the shift in the Dirac point originating from the substrate's intrinsic doping. Therefore, one can follow the Dirac point movement as we apply a gate-voltage. Equation 2.8 is used for all our devices in order to correlate our Dirac shift to the applied gate-voltage.

Chapter 3:

Experimental:

3.1 Gate-Tunable STM:

All of our experiments were performed on a home-build STM with an additional connection which allows us to apply a back gate voltage to the back of the sample. In the following sections I will give an overview of the overall modifications made to our STM instrument, the structure of our graphene based device and its behavior under an external electric field.

3.1.1 STM set-up:

All experiments were performed on a home built STM located in the *Precision Laboratory* at the Max-Planck-Institute for Solid State Research. An illustration of our device is shown in figure 3.1. The instrument is built on an actively damped concrete block which is located in an electromagnetically and acoustically isolated box. It is further isolated from the concrete block with passive dampers and the STM head is further isolated by yet another set of passive dampers. This allows us to perform our measurements with atomic precision. The instrument consists of two main chambers which are maintained under UHV conditions. The sample is introduced to the preparation chamber (left side in figure 3.1) through a differential load lock and can be moved inside the instrument by using a manipulator with the ability to rotate 360^{o}. Once inserted in the manipulator the sample can undergo several treatments which include surface cleaning and evaporation of a specific molecular system onto the sample. The surface cleaning can be done by means of sputtering the surface with Ar ions and annealing via electron bombardment and radiation of the sample holder. Due to the sensitivity and complexity of our sample it is important that the annealing process be done in a controlled manner and regulated continually, mainly through monitoring the temperature. To optimize this crucial process, the annealing procedure has been automated using Python code (Appendix B). When needed, the sample can be transferred by the manipulator into the STM chamber (right side in figure 3.1). Once it is inserted into the chamber, the sample is in contact with a liquid helium bath cryostat, which is isolated from ambient by a liquid nitrogen cryostat. This

allows the system to be measured at temperatures as low as 4.8K and at pressures lower than $p = 10^{-12}\ mbar$.

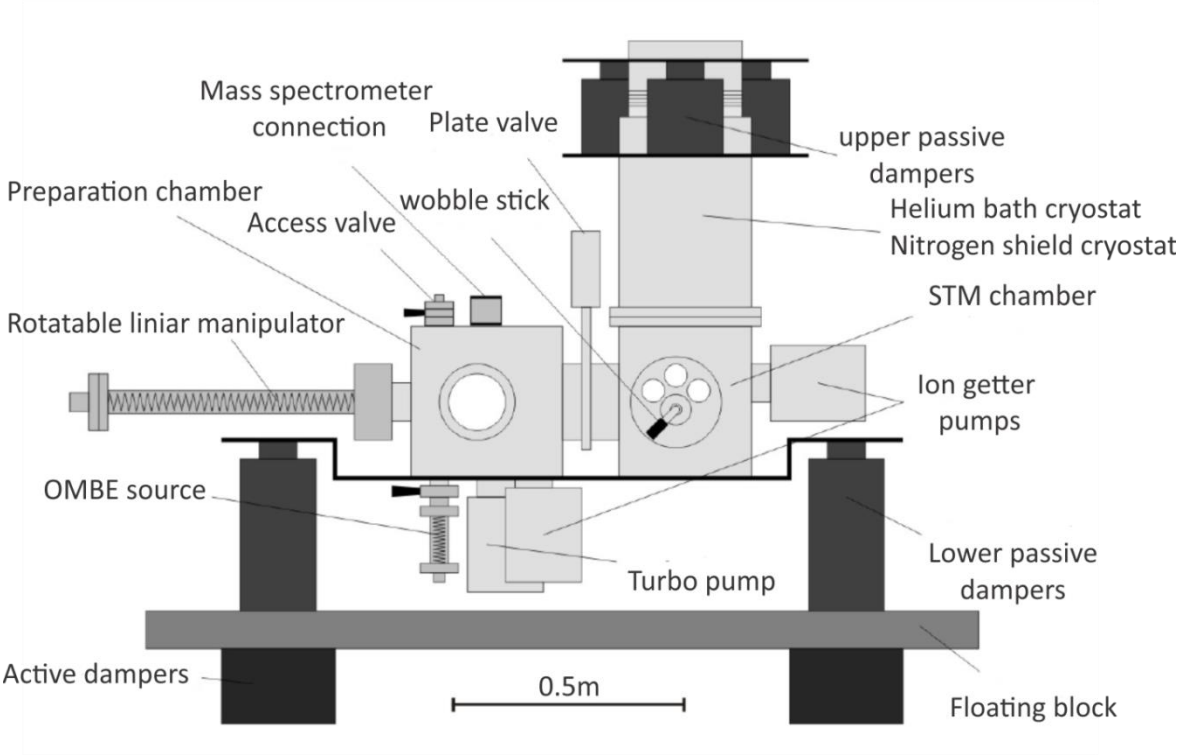

Figure 3.1: A scheme of the home-built Gate-STM being used throughout the thesis.

In order to ensure a precise control of the sample stage and the tip movements all components are controlled by means of piezo-active elements as seen in figure 3.2. The tip is mounted on top of an Attocube piezo, which allow us to quickly approach the sample with the assistance of optical access as well as perform the fine movements needed for the scan. Once the tip is located close to the surface, the final approach is controlled by the *Nanonis* system with a feedback loop. All movements in the x and y axis (coarse and fine) are done by two sets of shear piezos which are connected to the sample stage.

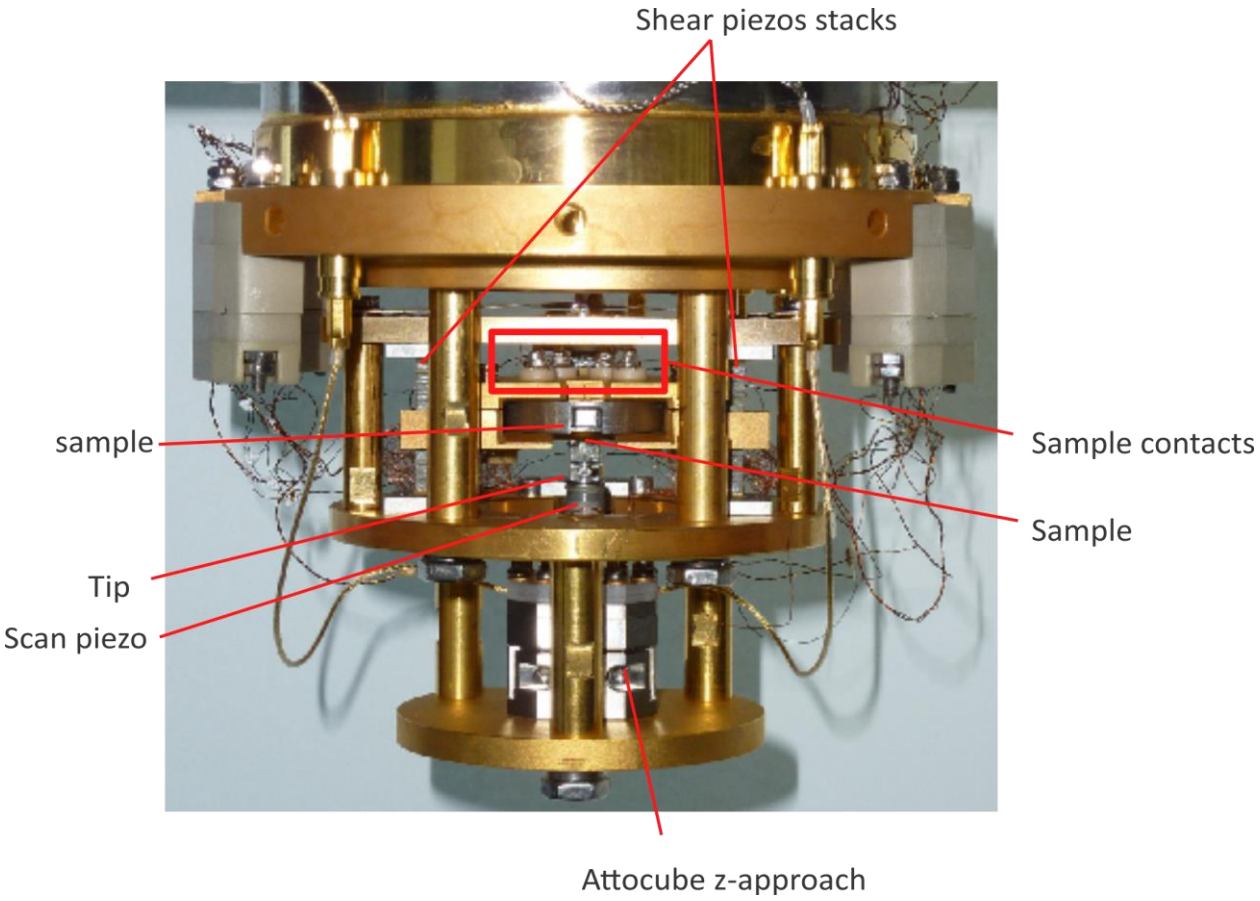

Figure 3.2: Our STM head, the sample and its connections and the tip are indicated in the image, also visible are the shear piezo-elements and the tip mounted on the Attocube piezo.

3.1.2 Optical access:

Due to the complex conditions of the graphene surface i.e. organic solvents residues and holes in the graphene layer, a high resolution optical access to the sample is crucial to prevent the tip from crashing into the SiO_2 substrate. Figure 3.3 shows an optical image taken in our STM chamber. Once the sample is inserted to the STM chamber a clear reflection of the tip is visible (figure 3.3a) that enables us to perform safe and quick approaches to the system and revisit high quality areas on the sample. Furthermore, in order to revisit high quality areas on the surface without retracting the tip, we calibrated the coarse piezo movement by taking a series of optical images and correlate it to the tip movement. (See Appendix A).

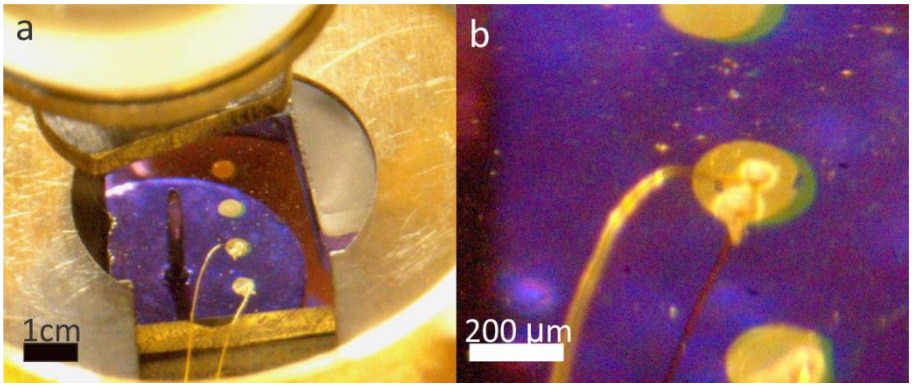

Figure 3.3: An optical image of the tip above our sample (a), the wired gold pads are visible. Our maximal optical zoom allows us to achieve resolution of down to 50µm (b).

3.1.3 The modified sample holder:

In order to utilize the ability to apply a back gate voltage to the sample within an STM, one can construct a modified sample holder that isolates the back electrode from the rest of the sample holder. Figure 3.4 illustrates the design of the sample holder that has been used in our experiments. The sample is glued to the sample stage with a UHV compatible conducting glue and pressed from the top by a molybdenum spring and top plate while still being isolated by an upper sapphire spacer. The back gate voltage is applied to the sample through the sample stage which is isolated from the rest of the sample holder by an additional sapphire spacer. The bias voltage is applied to the sample surface through an isolated gold electrode. The bias is applied through connecting 17µm thick Au wires to pre-evaporated Au/Cr pads on the surface (figure 3.3).

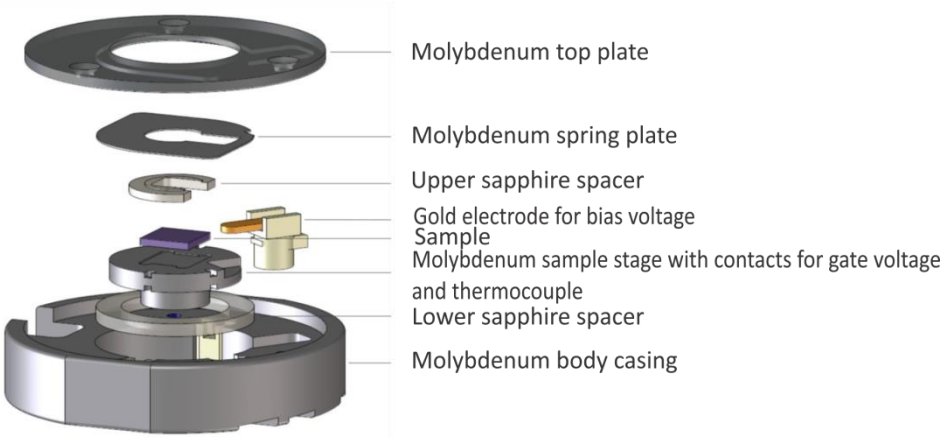

Figure 3.4: A schematic of the back-gate modified sample holder.

3.2 Graphene-based FET:

In the following chapter I will overview the different G-FETs being used in this thesis and how we fabricated and characterized them. For each system the characterization process has been carried out through the use of several instruments. First, optical microscopy was used to evaluate the overall quality of the device, i.e. if the surface is intact or whether it contains holes/cracks, and to observe the presence of residues of the etched metal foil and organic solvents. Second, we used AFM in order to investigate the surface corrugation and cleanliness at the micrometer scale. All the device's electronic and topographic features were characterized at the atomic scale using STM. Complementary spectroscopic methods have been used to provide additional information on the composition and electronic structure of the systems. Raman spectroscopy has been used to identify the presence of different components in our device by detecting their "fingerprint" spectrum. STS measurements were used in order to characterize the electronic structure of the devices and their doping level. As was described in *chapter 2.2.1*, our graphene-FET device has to be constructed out of three main components. The substrate has to be conductive since it functions as the device back gate electrode. The insulating layer, which acts as the dielectric material in a plate capacitor structure, separates the graphene layer from the substrate. In most known systems these first two requirements can be easily fulfilled by choosing a standard Si wafer, since it is accompanied by a naturally oxidized layer of SiO_2, acting as the insulating layer, and the graphene sheet acting as the FET conduction channel. Throughout all our experiments we used highly p-doped Si wafers with an oxidized layer of 300 nm SiO_2 as our substrate and dielectric material, respectively. The graphene monolayers were grown via chemical vapor deposition (CVD) on Cu foil. Although several commercial products have been tried, the highest quality devices were fabricated by using home-grown graphene. All the devices being presented here have been fabricated by the chemical transfer of the graphene sheet onto the SiO_2/Si substrate. We chose the chemical transfer method since it provide large scale graphene sheets. This will allow us to approach the surface with the STM tip more easily, preventing any unwanted tip crashes on the insulating SiO_2 layer. However, this procedure can cause defects and impurities in the graphene monolayer such as residues of the metal foil and of the organic solvents being used in the procedure. The cleaning procedure after transfer is crucial for the overall quality of the device. Therefore, several transfer methods and cleaning procedure were used and optimized in order to improve the device quality. During my Ph.D. the device quality has been continually improved, enabling us to perform more elaborate and controlled experiments. The graphene/SiO_2/Si devices presented here were used for the experiments shown in *chapter 4*.

The roughness of the underlying SiO_2 substrate is known to cause corrugation in the capping graphene layer, subsequently causing inhomogeneous charge distribution on the graphene surface. The presence of a thin layer of hBN beneath the graphene sheet is known to improve the charge distribution in the system [34,35] and passivates the SiO_2 dangling bonds [55], resulting in an overall improvement of the graphene doping levels and electrical properties [56,57]. Therefore, we improve the transfer and cleaning procedures of CVD-grown hBN [58] and add it as an intermediate step before the graphene transfer. The graphene/hBN/SiO_2/Si devices presented here were used in the experiments shown in *chapter 5*.

The fabrication of the G-FET systems via the wet transfer method was always constructed of several repeated steps. Here, the general concept of the steps is provided followed by a specific recipe for each of the G-FET devices. The variations between the recipes are mainly due to different precursor materials and were tuned through trial and error during the Ph.D.

Coating with protective polymer:

Graphene grows on both sides of a metal foil (usually Cu) during CVD growth. This can be inhibited before the etching procedure by protecting one of the sides by coating it with an organic polymer. In the majority of our experiments we used the organic polymer poly-methyl-methacrylate (PMMA). The polymer fulfills a double role, not only as a protective layer for the graphene, but also as mechanical stabilizer which enables an easier handling of the graphene sheet. During our device fabrication we experimented with several sorts of polymers: different in chain lengths (50k, 200k and 950k) and concentration (3.5% and 5%). One expects better mechanical stabilization with longer chains and higher concentration of the sample. On the other hand, this lowers polymer solubility and the cleaning procedure of the polymer will be more complicated. In order to achieve a homogenous, stable but not too thick layer of the organic polymer we used a drop cast and spin-coater in the procedure.

Etching of the Cu/Fe foil:

Before lifting the polymer/2D stack one needs to etch the underlying foil. During the etching process the coated graphene layer is gently placed in an ammonium persulfate acid (APS-$NH_4S_2O_8$) solution. The exact duration of the etching process depends on the thickness of the metal foil and the concentration of the etching solution. If the etching is insufficient some metallic residues may

remain which can cause surface corrugation and induce doping in the GEFT device. An excessive etching can damage the 2D layer and contribute to its doping level as well. Therefore, specific etching parameters have been chosen after repeated trial and error experiments. Furthermore, after each etching process one should rinse the sample thoroughly in order to reduce any doping effects or corrugation due to the etching process.

Lifting the 2D material with the substrate:

When the etching is complete the 2D stack is being lifted by the substrate. After each lifting process, it is important to anneal the stacked in a controlled manner in order to remove any water residues and to improve the adhesion between the different layers.

Removal of the protective polymer:

The removal of the protective polymer is the most critical part in the device production since a clean and flat surface is crucial for all STM measurements. Throughout all of the experiments several methods have been tested such as catalytic-activity based removal using a platinum plate or solvent based removal using organic solvents such as acetone or isopropanol. Suitable duration and solvent concentration were selected after several trial and error experiments. The recipes presented in this thesis are our optimized procedures.

3.2.1 Graphene/SiO_2/Si:

Preparation:

- A piece of graphene/Cu was cut by using a scalpel and fixed to a plastic support with a duct tape.
- A droplet of poly methyl methacrylate (PMMA) with chain length of 200K and concentration of 3.5% was added and spin-coated.
- The PMMA was dried on top of a hot plate for 4 min at 70°C.
- After the removal of the tape, the bottom graphene was etched in a nitric acid solution (HNO_3, 0.3M) for 3 min.
- The Cu foil was etched in an ammonium persulfate (APS- $NH_4S_2O_8$) acid (1M) for 0.5-2h.
- The graphene sheet was transferred into deionized water, the step was repeated twice.
- The SiO_2/Si substrate was cleaned by means of oxygen plasma treatment for 10 min.
- The etched PMMA/graphene was lifted by the SiO_2/Si substrate and the stack was blow dried perpendicular to the surface.
- The PMMA/graphene /SiO_2/Si sample was annealed on top of a hot plate at 30°C for a few minutes and transferred to an oven at 300 °C for 2.5 hours in order to remove any water residues and enhance the adhesion between the graphene and the substrate.
- PMMA removal: The sample was bathed in Acetone/N-Ethylpyrrolidone (NEP) at room temperature for 10 min, followed by a second bath in Toluene at room temperature for 10 min.
- PMMA removal: The sample was placed facing down on top of a platinum plate and annealed in an oven for 1.5 hours at 400 °C.

- The sample was then transferred into a UHV chamber and annealed at 430^{o} for 12 hours.

Characterization:

Each sample was characterized using spectroscopic and microscopic techniques from the micro- to the nano-scale.

Optical microscopy:

After lifting the sample with a SiO_2/Si substrate an optical image has been taken before and after the removal of the PMMA in order to verify the sample quality (figure 3.5a and figure 3.5b respectively). Since the presence of PMMA increases the doping level of graphene and decreases its charge carrier mobility [56], it is crucial for the performance of our device to remove the PMMA residues. A thorough cleaning procedure of the sample is critical, but too aggressive cleaning procedures can damage the graphene layer. As the PMMA is being rinsed it can rip part of the graphene with it, creating large holes and gaps in it. In figure 3.5a the PMMA can be recognized by its bright rainbow-like colors. Although, it is clear that the majority of the PMMA was removed (figure 3.5b) we still have some residues which enables us to see the underlining graphene through its contrast (turquoise color on the surface). The PMMA residues will be removed by several cycles of annealing conducted in Ultra-High-Vacuum (UHV) conditions, as elaborated more specifically later in *chapter 4*.

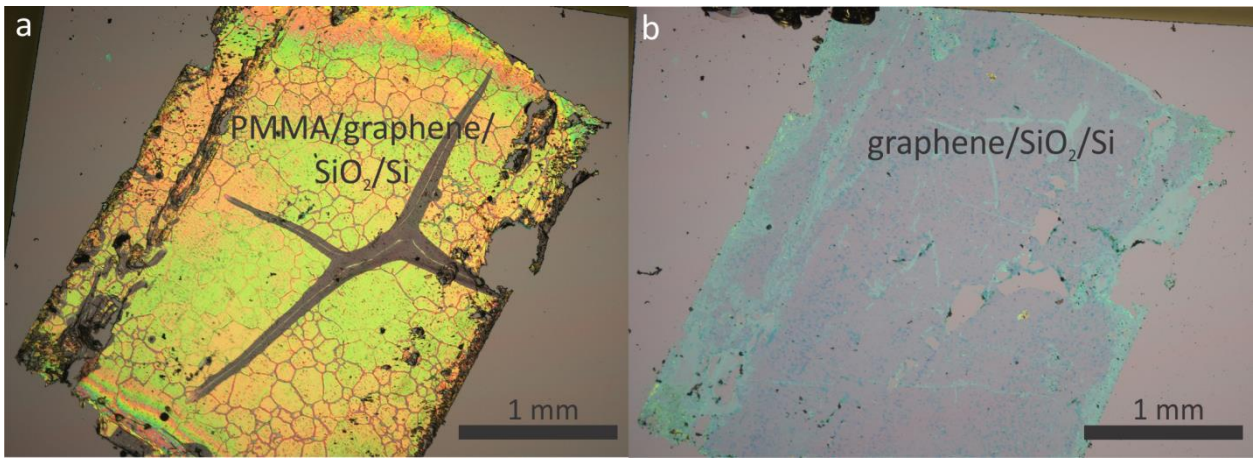

Figure 3.5: Optical microscope images of our graphene/SiO_2/Si device before a) and after b) PMMA removal. The dark turquoise spots are multilayer graphene nucleation sites.

Raman spectroscopy:

Raman spectroscopy measurements were performed in order to confirm the existence and quality of the graphene layer by detecting and locating the G and D modes. The G mode is a first order Raman band resonance and originates from the C-C stretching mode in sp^2 hybridized carbon materials. The D mode originates from the structural disorder in graphene. The spectroscopic features in the spectrum do not only serve as a "fingerprint" for graphene but can also indicate the presence of generic defects and its doping level [59,60]. Figure 3.6 presents Raman spectra taken with a 532 nm laser on our sample. Figure 3.6a presents the characteristic features of a pristine graphene layer, with the 2D and G peaks appearing at $2686\ \mathrm{cm}^{-1}$ and $1582\ \mathrm{cm}^{-1}$ respectively which is in good agreement with the reported literature [59,60]. Figure 3.6b (red rectangular at figure 3.6a) presents the specific range of the G and D peaks, the high ratio between the peaks intensities evidence the high quality of the sample. The inset displays a magnification of peak D and its fit (green curve), the peak is centered at $1352\ \mathrm{cm}^{-1}$ which is in good agreement with literature [59,60]. For all of the spectra the noise was subtracted through a spinal manual method and the fitting function was chosen to be Voigt, which showed better agreement compared to Lorentzian and Gaussian fits.

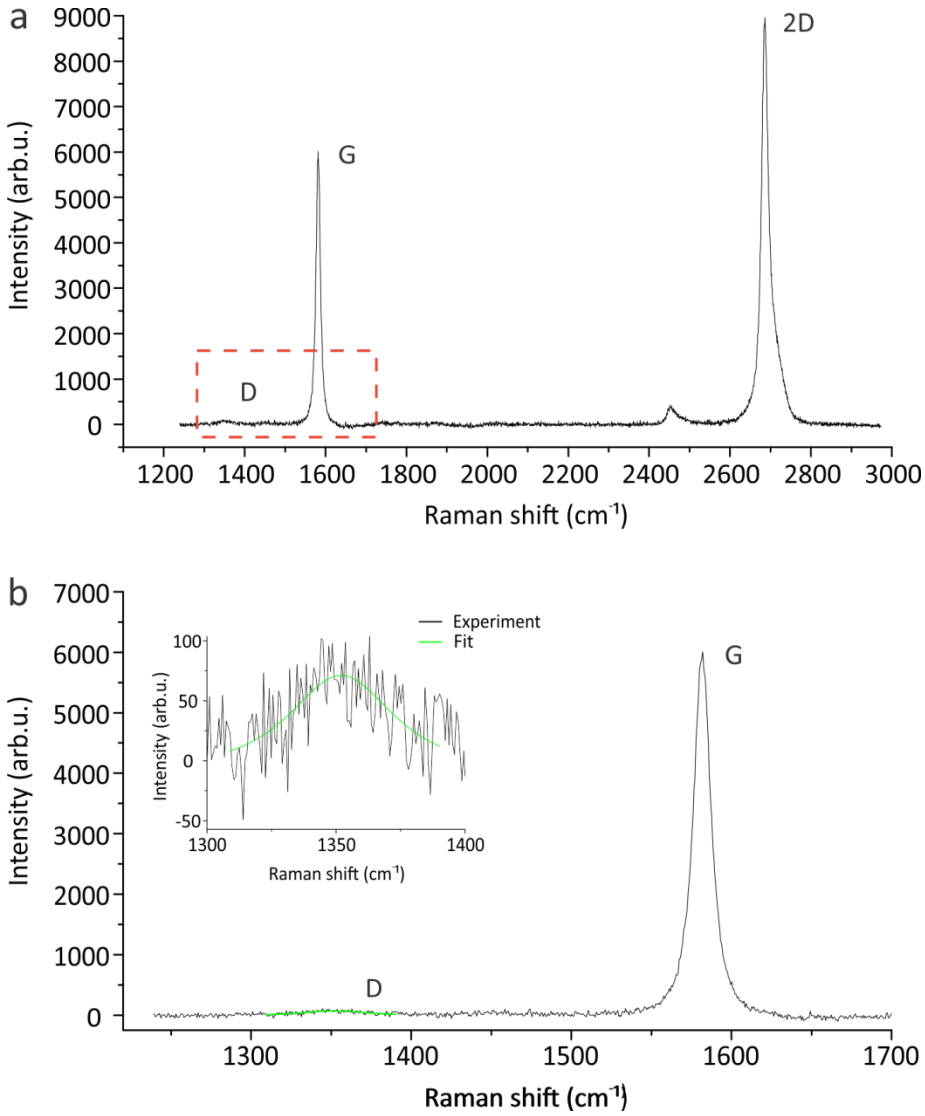

Figure 3.6: Raman spectra taken on top of our graphene/SiO_2/Si device. a) An overview spectra presenting all the characteristic features of single layer graphene. b) Magnification of the range marked with red rectangular in a). Inset: magnification of the D peak and its fit.

Topographic measurements:

The overall quality of the sample surface was characterized by using AFM and STM (figure 3.7). A large scale AFM topography image of the sample (figure 3.7a) exhibits a relatively clean surface; the perturbations on the surface are PMMA residues which remain after the cleaning process. Figure 3.7b presents an STM topographic image showing the graphene surface with atomic resolution. Surface corrugation of about 8 Å, originating from the underlying SiO_2, is clearly visible and will play a critical role in the experiment described in *chapter 4*. Furthermore, several underlying surface

defects and perturbations can be observed on the surface despite further rigorous cleaning and annealing steps under UHV conditions.

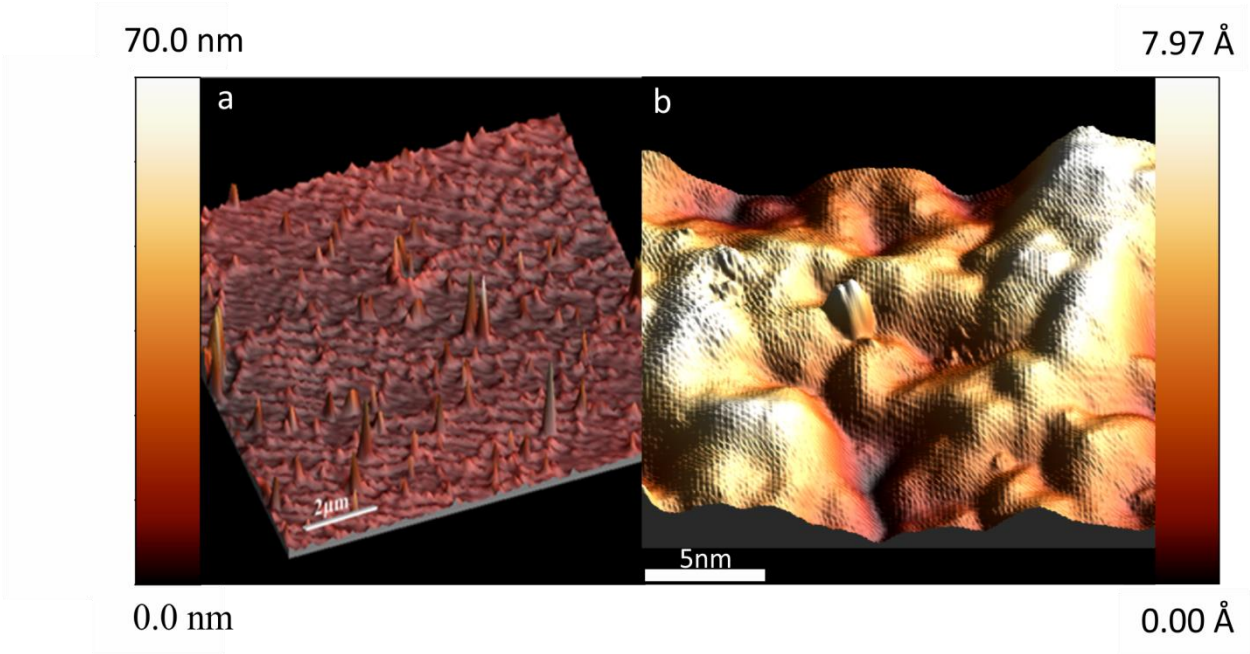

Figure 3.7: a) An AFM topographic image of the graphene/SiO_2/Si device. b) 3D visualization of an STM topographic image showing the graphene corrugation due to the underlying SiO_2, the graphene atomic resolution is visible.

A more close examination of the surface reveals graphene's atomic resolution and the expected hexagonal lattice structure of the pristine graphene layer (figure 3.8a). The same six-fold symmetry can be observed in a Fast Fourier Transform (FFT) spectrum of the surface in the reciprocal lattice (green hexagonal in figure 3.8b) measuring the reflections (marked by white circles) at 2.15 Å (blue dotted line) which is in good agreement to the theoretic value of the graphene lattice constant of 2.40 Å [61].

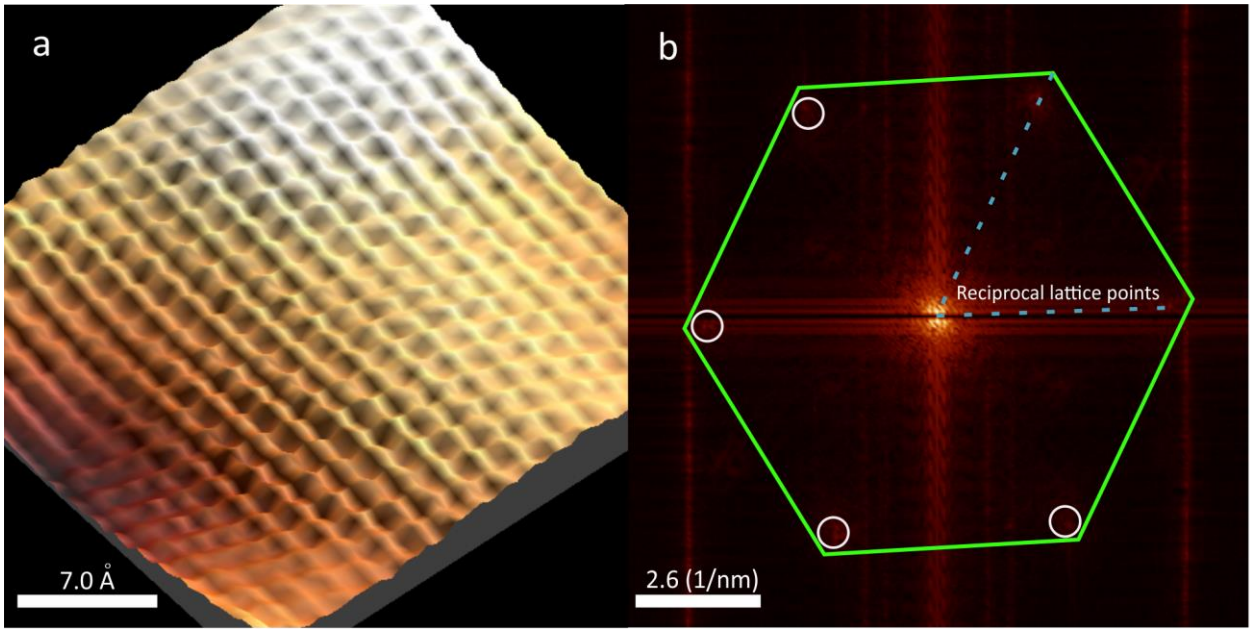

Figure 3.8: a) An Atomic resolution STM image of the surface and b) its corresponding Fast Fourier Transform (FFT). The green hexagon marks the reflections corresponding to the graphene reciprocal lattice.

STS measurements:

To quantify the influence of the gate voltage on the charge distribution of the graphene surface, several differential conductance spectra have been recorded at different gate voltages, enabling the tracking of the Dirac point across the Fermi level (red dot in figure 3.9). Swiping the gate-voltage from –40 V to +40 V alters the graphene doping levels from p-doped to n-doped in a continuous manner. All the spectra exhibit the characteristic V shape DOS of graphene with the expected phonon-induced band gap at the energy range of $-65\ \mathrm{meV} \leq \mathrm{E_{gap}} \leq +65\ \mathrm{meV}$ [30] as was elaborated in *chapter 2.2.2*. As it can be clearly seen in the differential conductance spectra, when no gate voltage is applied (V_g=0 V) our initial graphene surface is p-doped. The relative neutrality point seems to be located around V_g=20 V. The high doping levels can be due to the etching process[62,63] and ion intercalation during the annealing process[64].

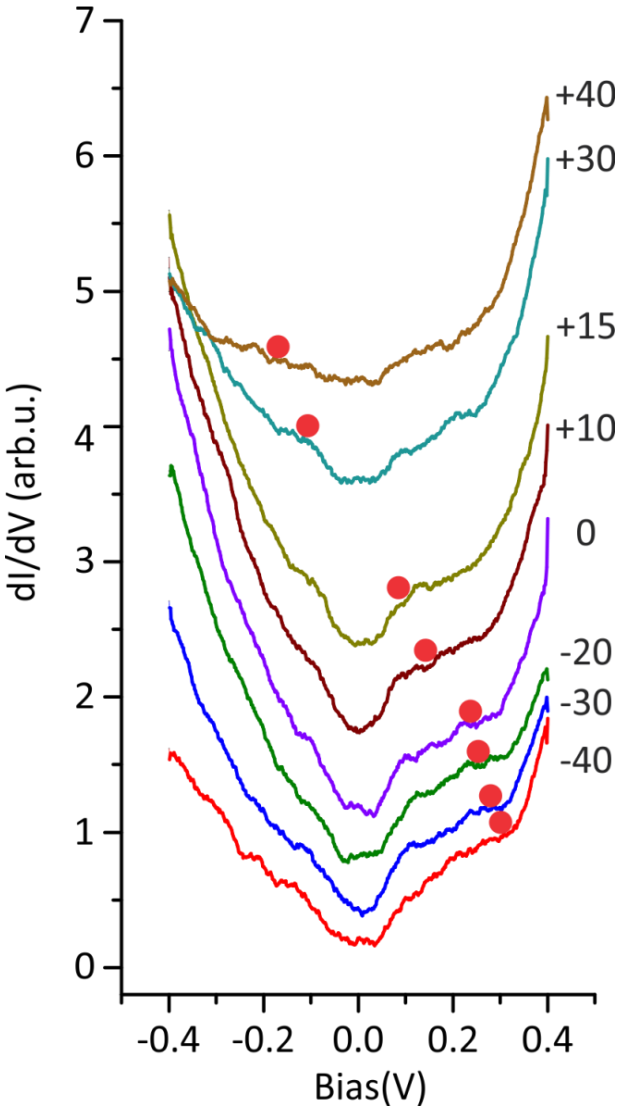

Figure 3.9: dI/dV spectra at different gate voltages show the Dirac point shift. V_b=500 mV, I=10pA.

The Dirac point location (V_D) depends on the gate voltage and one can extract the energetic position of the Dirac point (E_D) and plot it as a function of the applied gate voltage (figure 3.10). The dependency of the Dirac point on the gate voltage can then be confirmed by fitting $E_D(V_g)$ according to *equation 2.8* [53,54] (red curve in figure 3.10).

The graphene charge carrier coupling parameter (α) and the shift in the Dirac point with respect to the Fermi level (V_0) were derived from the fit as $\alpha = 9.8 \cdot 10^{14}\ \frac{1}{\mathrm{m^2V^2}}$ and $V_0 = 19.4\ \mathrm{V}$, which is in good agreement with previous reports [30]. Furthermore, as it was explained in *chapter 2.2.3*, by using the simple plate capacitor model one can utilize α to calculate the estimated thickness of the oxide layer according to *equation 2.7*. The estimated thickness according to our parameters is $d = 220\ nm$ which is in the expected range of our SiO_2 layer expected thickness.

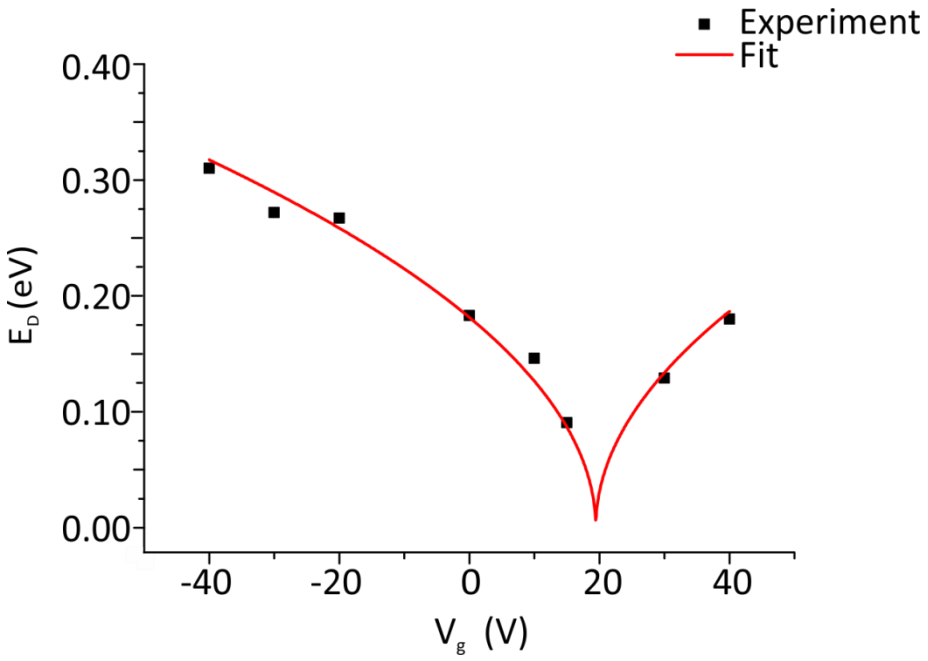

Figure 3.10: The energy position of the Dirac point, E_D, (taken from the deferential conductance spectra taken on the sample) as a function of the applied gate voltage. The red curve is a fit based on the square-root dependence of the Dirac point location on the gate voltage shown in equation 3.1.

3.2.2 Graphene/hBN/SiO_2/Si:

After finishing the first project that utilized the graphene/SiO_2/Si device, the GFET device was improved by adding an additional decoupling layer of hexagonal born nitride (hBN) underneath the graphene sheet.

Preparation:

- A piece of graphene/Cu has was cut by using scalpel and fixed to a plastic support with a duct tape.

- A droplet of poly methyl methacrylate (PMMA) with chain length of 200K and concentration of 3.5% was added and spin-coated. A uniform coating can be achieved by using a spin coater (6000 rpm for 35 sec).

- The PMMA was then dried on top of a hot plate for 4 min at 70°C.

- After the removal of the tape, the Cu foil was etched in an ammonium persulfate (APS-$NH_4S_2O_8$) acid (1M) for 3 h.

- The graphene sheet was transferred into deionized water. The step was repeated twice.

- A piece of hBN/Cu was cut using scalpel and fixed to a plastic support with a duct tape.- The hBN/Cu piece must be bigger than the PMMA/graphene/Cu stack.

- The etched PMMA/graphene was lifted by the hBN/Cu and the stack was blow dried perpendicular to the surface.

- The sample was annealed on a hot plate at 60°C-70°C for 2h in order to remove water residues and enhance the adhesion between the film and the substrate.

- A droplet of poly methyl methacrylate (PMMA) with chain length of 200K and concentration of 3.5% was added and spin-coated.

- The PMMA was dried on top of a hot plate for 4 min at 70°C.

- After the removal of the tape, the Cu foil was etched in an ammonium persulfate (APS-$NH_4S_2O_8$) acid (1M) for 3 h.

- The stack was transferred into deionized water. The step was repeated twice.

- The SiO_2/Si substrate was cleaned by means of oxygen plasma treatment for 10 min.

- The etched PMMA/graphene/ hBN was lifted by the SiO_2/Si substrate and the stack was blow dried perpendicular to the surface.

- The PMMA/graphene/hBN/SiO_2/Si device was annealed on a hot plate at 100°C for 2h in order to remove water residues and enhance the adhesion between the stacked layers and the substrate.

- Removal of PMMA: The sample was bathed in Acetone/N-Ethylpyrrolidone (NEP) at room temperature for 10 min, followed by a second bath in Isopropyl-alcohol (IPA) at room temperature for 10 min.

- The sample was annealed in a tube furnace for 2 hours at 400°C in forming gas flow (around 50L/h=800 sccm) with a ramping rate of 15 °C/min.

- The sample was then transferred into a UHV chamber and annealed at 430^{o} for 12 hours.

Characterization:

Optical microscopy:

As shown earlier the sample was first characterized by means of optical microscope. The green dotted line in figure 3.11 represents the border between an area containing our sample covered with PMMA and an area containing only PMMA. Sure enough after rinsing the sample, one can see that the specific region has been removed entirely (figure 3.11b). This serves as another evidence for the presence of a graphene layer under the PMMA residues shown in turquoise color on the surface. The overall surface looks intact with no visible holes in it. The PMMA residues were removed by several cycles of annealing conducted in ultra-high-vacuum conditions.

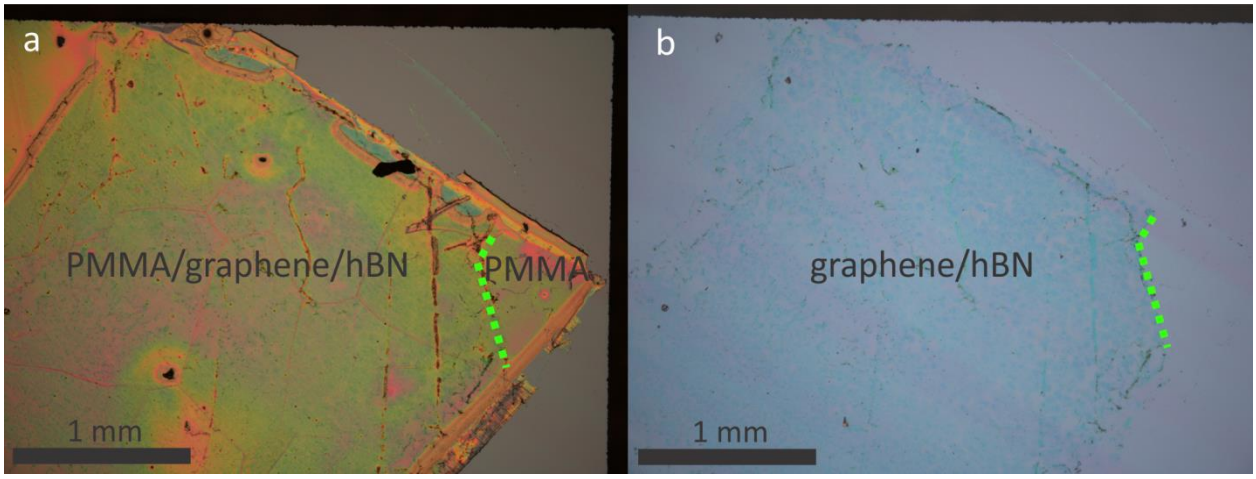

Figure 3.11: Optical microscope images of the graphene/hBN/SiO_2/Si device before a) and after b) PMMA removal.

Raman spectroscopy:

Figure 3.12a presents the overall characteristic features of pristine graphene, with the 2D and G peaks located at $2686\ \mathrm{cm}^{-1}$ and $1596\ \mathrm{cm}^{-1}$ respectively, which is in good agreement with previous reports[60]. Examination of the energy range corresponding to peaks G and D reveals the expected D peak located at $1350\ \mathrm{cm}^{-1}$ (figure 3.12b). The high ratio between the G and the D peak intensities indicates a low defects concertation. A closer look at the D peak revels the existence of a second peak at $1365\ \mathrm{cm}^{-1}$ (figure 3.12c) which is in good agreement with the location of an

expected hBN peak [65]. As mentioned earlier for all of the spectra the noise was subtracted through a spinal manual method and the fitting function was chosen to be Voigt.

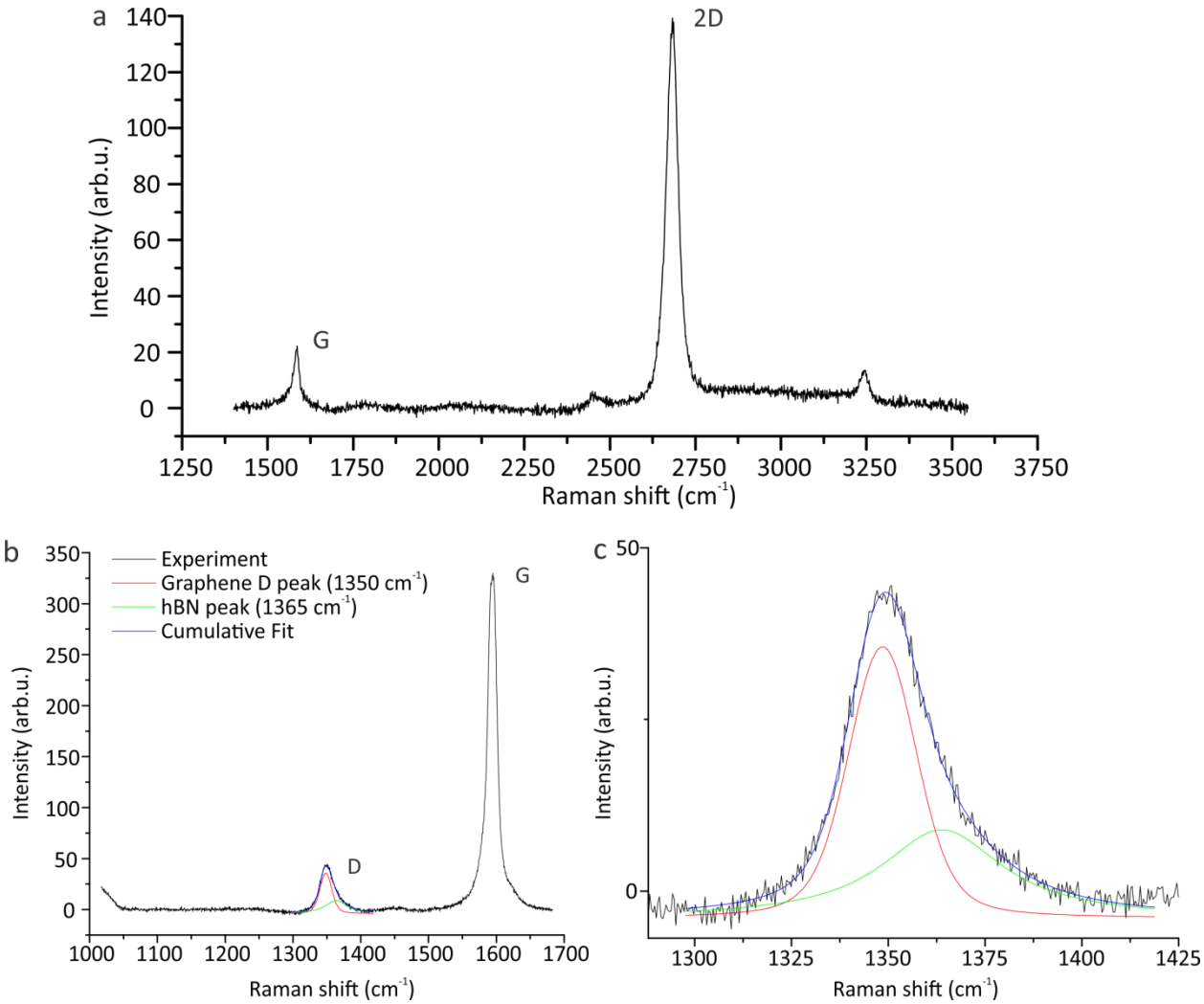

Figure 3.12: Raman spectra recorded on top of our graphene/hBN/SiO_2/Si device. a) An overview spectra presenting the graphene characteristic G and 2D peaks. b) Magnification of the range corresponding to the G and D peaks. c) A magnification and deconvolution of the D peak. The graphene D peak (red) and the hBN peak (green) are clearly observed.

Topographic measurements:

Figure 3.13a presents a large topographic AFM image of the new grapheneh BN/SiO_2/Si device. The sample exhibits an overall cleanliness at the micro-scale compared to the graphene/SiO_2/Si device. We attribute the substantial improvement in the sample conditions to the advancement in our cleaning procedures and to the passivation of the SiO_2 by the hBN layer. SiO_2 is known to induce surface charge traps [66] that can interact with the PMMA residues. Therefore, passivating the dangling bonds should improve the cleaning procedures. After an intensive cleaning and annealing procedure under UHV conditions, the device was characterized by an STM at 5K (Figure 3.13b). A clear moiré pattern originated from the graphene and the underlying hBN can be observed. Furthermore, the graphene atomic resolution is also visible.

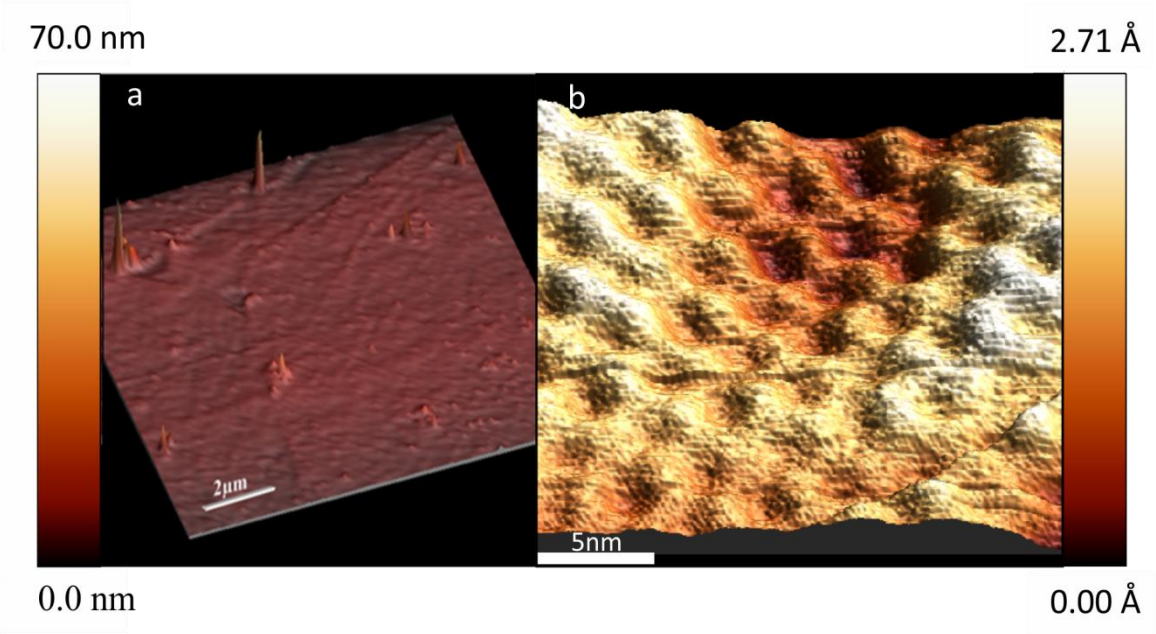

Figure 3.13: a) An AFM topographic image of the graphene/SL-hBN/SiO_2/Si device. b) 3D visualization of an STM topographic image showing a moiré patterns between the graphene and the underlying hBN, the graphene atomic resolution is visible.

Figure 3.14a displays a magnification of the area in figure 3.13b, the graphene atomic structure on top of the moiré pattern is clearly observable. A fast Fourier transform of the area (figure 3.14b) revels the six fold symmetry reflections corresponding to the moiré pattern (marked with turquoise hexagon) and to the graphene atoms (marked with green hexagon). The moiré lattice spacing can be calculated directly from the FFT reflections, $\lambda = 2.4\,nm$ and the graphene lattice constant

$a = 0.214\,nm$ (doted blue lines) which is in good agreement with the theoretical value of suspended graphene layer $a = 0.246\,nm$ [61].

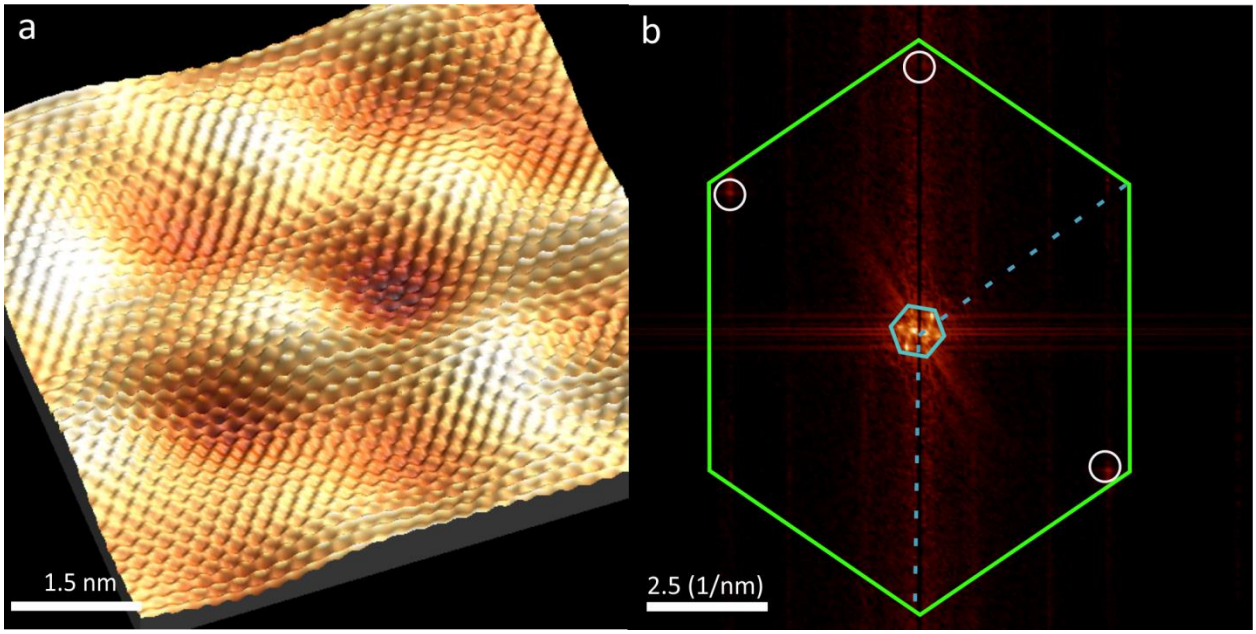

Figure 3.14: a) A magnification of the area shown in figure 3.13b revel the graphene atomic structure and moiré pattern. b) FFT of the magnified area.

By measuring the perturbations caused by the moiré pattern and the top graphene layer, one can calculate the twisting angle between the graphene and the hBN layer [67] according to the relations: (3.1)

$$\lambda = \frac{(1+\delta)a}{\sqrt{2(1+\delta)(1-cos\theta)+\delta^2}}$$

Here, the periodically of the moiré pattern is λ, the lattice mismatch between the graphene and the hBN $\delta = 1.8\%$ [35] and the graphene lattice constant a. Therefore, the twisting angle between the two layered materials is $\theta = 2.56°$.

STS measurements:

In order to quantify the influence of the gate voltage on the charge distribution of the graphene surface, several differential conductance spectra have been taken at different gate voltages, enabling the tracking of the Dirac point across the Fermi level (red dot in figure 3.15). The graphene/hBN/SiO_2/Si device exhibits a much more stable behavior under the influence of the applied gate voltages than the graphene/SiO_2/Si device, which allowed us to augment our gating range to $-70\ V \leq V_g \leq +70\ V$. The graphene/hBN/$SiO_2$/Si device exhibits a higher level of p-doping compared to the graphene/SiO_2/Si device and the relative neutrality point seems to lie around V_g=50 V. The increased dopant level is probably due to the double etching procedure and ion intercalation during the elongated annealing process.

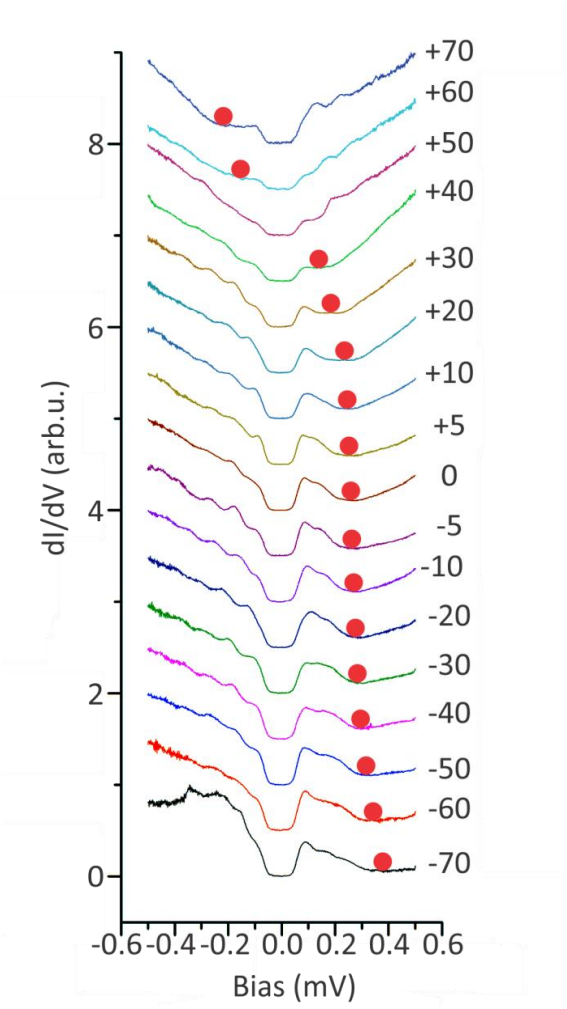

Figure 3.15: dI/dV spectra at different gate voltages show a shifting Dirac point. V_b=500 mV, I=50pA.

As explained above, the energetic position of the Dirac point (E_D) for different gate voltages were extracted from figure 3.15 and plotted as a function of the applied gate voltage (figure 3.16). In accord with the previous device, we can confirm the measurement of our Dirac shift by fitting the experimental results according to *equation 2.8* (figure 3.16). We were able to derive the coupling constant $\alpha = 7.09 \cdot 10^{14} \frac{1}{\mathrm{m^2 V^2}}$ from the fit and the relative neutrality point of $V_0 = 50.7\ \mathrm{V}$, the first is in good agreement with previous reports [34].

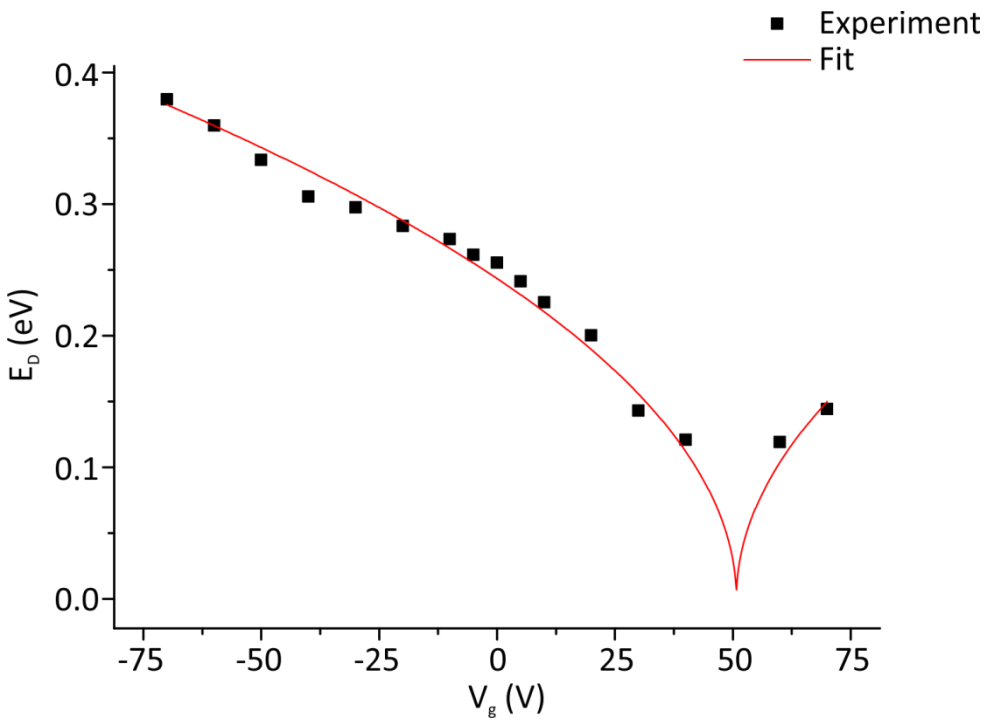

Figure 3.16: The energy position of the Dirac point, E_D, (taken from the deferential conductance spectra in Figure 3.15) as a function of the applied gate voltage. The red curve is a fit based on the square-root dependence of the Dirac point location on the gate voltage shown in *equation 2.8*.

Furthermore, as shown earlier we used the simple plate capacitor model to calculate the estimated thickness of the oxide layer, when we assume the overall permittivity of the dielectric layer as:

(3.2)

$$\varepsilon_{dielectric} = \frac{\varepsilon_{SiO_2} + \varepsilon_{hBN}}{2} = \frac{3.3 + 3.9}{2} = 3.6$$

and computed the value of $d = 280\,nm$, which is in much better agreement with the expected value of 300nm than we calculated for the graphene/SiO_2/Si device.

3.3 Tip preparation on Au(111) surface:

Before conducting any measurements, it is paramount to calibrate the tip on a known reference surface. The calibration of the tip is necessary due to the sensitivity of the STS signal recorded on a graphene surface to contaminations on the tip apex [30,40]. Throughout all experiments we used electrochemically etched Pt/Ir tips (0.8/0.2) that were purchase from *Keysight Technologies*. All tips were calibrated on an Au(111) single-crystal (figure 3.17a).

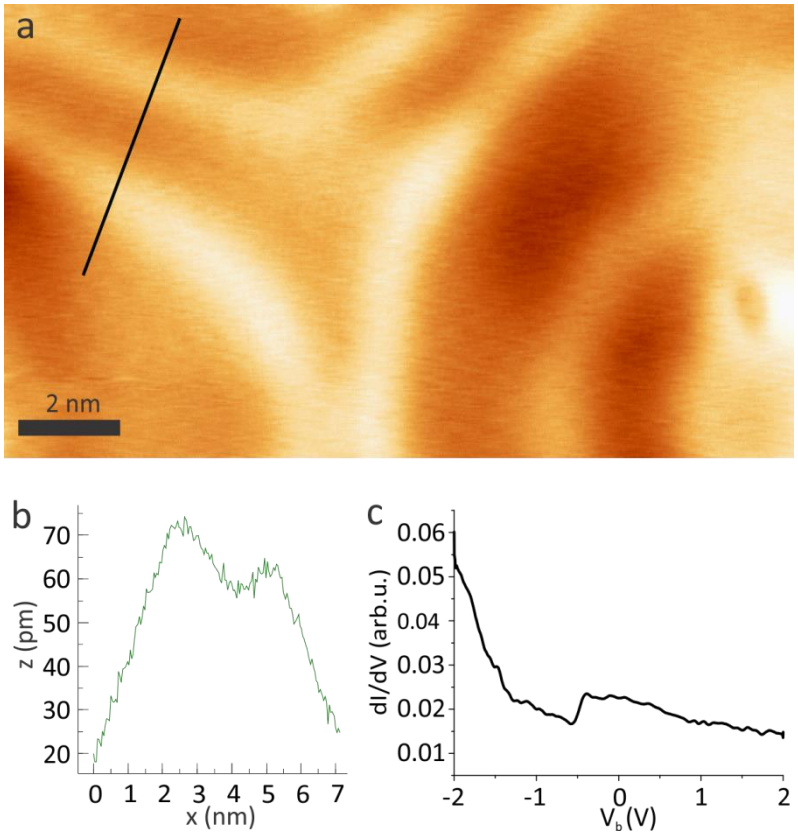

Figure 3.17: a) Pristine Au(111) surface. b) Line scan (black line in a) showing the characteristic herringbones reconstruction c) A characteristic dI/dV spectrum of Au(111).

Before the calibration process the Au(111) crystal was cleaned under UHV conditions by several cycles of Ar-based sputtering followed by 10 min annealing of up to 500℃. The calibration consisted of two evaluations, the tip sharpness which was checked by scanning over the herringbone reconstruction on the Au(111) surface (Figure 3.17b), and the tip condition regarding its composition by performing spectroscopic measurements on the Au(111) sample (Figure 3.17c). The characteristic step observed at V_b=-500 mV is due to the Au surface state [68,69] and indicates a clean tip. Tip treatment consists of a repeated controlled indentation of the tip into the clean surface, followed by

applying a bias pulse between the tip and the surface in the range of –10 V to +10 V. Since in the tunneling regime the tip-sample distance is usually in the angstrom scale the generated electric-fields can exceed 10 V/nm. In specific cases were the tip is heavily contaminated or right after introducing it to the STM chamber from an ambient environment a more aggressive treatment is needed. During the field emission process an external power source is connected directly to the tip and a high voltage of up to 450 V is applied for at least 5 min.

Chapter 4:

Free-Base Phthalocyanine molecules on Graphene:

4.1 Introduction:

During the last few decades there has been particular interest in how electric fields affect adsorbates with respect to their orientations, structures, oxidations states, vibrational modes and molecular orbitals' energies [70-74]. The last phenomenon listed is of special interest because the electric field can be used to alter the activation barriers along the reaction coordinate of a given chemical reaction [73,75 76]. Since the electric field is able to stabilize transition states of ionic or polar character, it can be used to adjust the kinetics and thermodynamics of a chemical reaction in a controlled manner, thereby act as a catalyst or inhibitor for the given reaction.

However, despite great advancements in computational modeling methods that predicts the effect of electric-field to catalyze certain reactions[74]. Designing an experiment that can measure how well-oriented electric fields can induce reactions at the single molecule level is extremely challenging. In particular, creating a well-directed homogeneous electric field is not straightforward. The field strength can vary as a function of the molecule's morphology or its adsorption sites. Therefore, to fully understand the electric field contribution to the overall observed behavior of the molecule, one should utilize surface sensitive instruments to measure its influence in real time. An adequate solution for these problems is to use an STM as the characterization tool as well as the source of the external electric field. Due to the atomically sharp STM tip apex termination, it is possible to apply an oriented, well-defined homogenous electric field to any system of choice[21,76]. Furthermore, in conjunction with the extremely small tip-sample distance ($\sim 9\text{Å}$), electric fields applied by the tip can be strong ($\sim 2\ \mathrm{V/nm}$) and be induced by relatively low voltages ($\sim |1V|$) that are needed to handle fragile molecular systems. Therefore, with the combination of atomic surface sensitivity and an oriented electric field, STM is exceptional in being able to manipulate and measure single molecule reactions at the atomic scale. A prominent example is the work of Argones et al. [76] who performed a Diels-Adler reaction using a well oriented electric field. By approaching a diene functionalized gold tip to a gold surface covered with dienophile molecules, they were able to form

new carbon-carbon bonds between the molecular moieties and monitor the reaction with the current signal.

A disadvantage in STM is the interdependence of its 3 setup parameters: the tunneling current, the bias voltage and the tip-sample distance. Since these parameters are inseparable, one cannot directly measure electric field effects on an observed system. However, our unique apparatus enable us overcome this inherent drawback as modifying the tip height can be done without changing the set point parameters. As elaborated in *chapter 2.2.3*, by applying a back gate voltage to our graphene/SiO_2/Si device we were able to change the local DOS of the graphene. This experimental configuration, in constant current mode, will change the tip height in order to maintain the initial current set point, which subsequently modifies the tip-applied electric field (figure 4.1). The capability to untangle the tip z-position from the tunneling current and the bias voltage is especially crucial when discussing chemical reactions which depend on the number and energy of the injected electrons.

In this chapter we demonstrate our ability to modify the tip-applied electric field which is then used to catalyze a proton-transfer reaction. This process was observed and analyzed within several molecules in a monolayer of free-base phthalocyanine molecules deposited on our gate-tunable graphene device. The well-oriented electric field reduces the activation barrier of the reaction which subsequently increases the hydrogen's switching frequency. Our conclusions were further substantiated through DFT calculations. The dependency between the applied electric field and the activation barrier raises the potential of the system or its related motifs to be used in future implementations of molecular electronics.

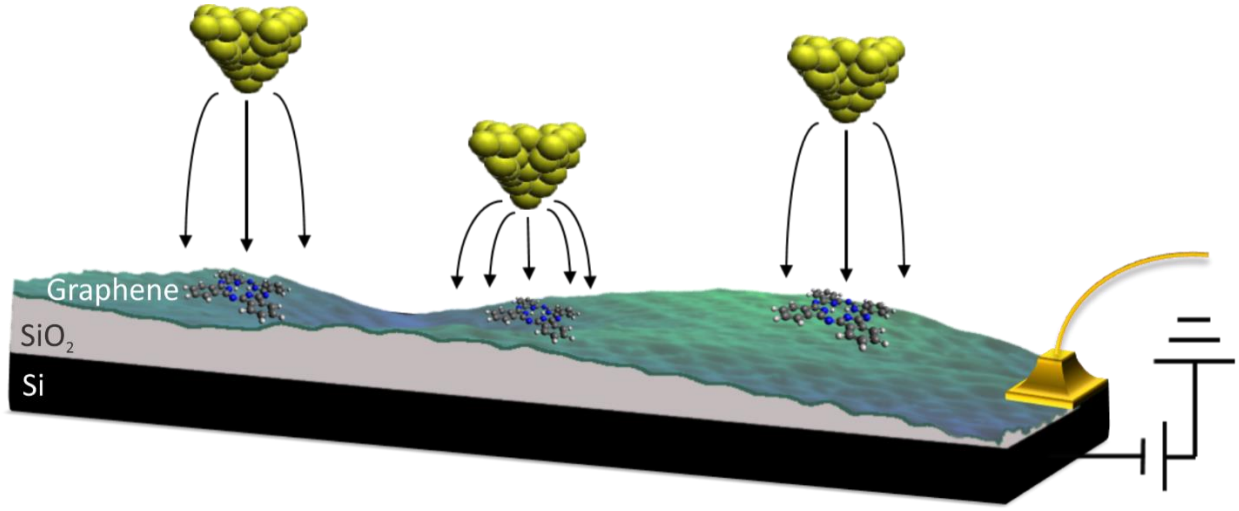

Figure 4.1: A schematic of the controlled gating of a single molecule in a tunnel junction. The tip induced electric field can be varied without changing the set-point bias voltage or tunneling current.

4.2 Tautomerization of H_2Pc:

H_2Pc molecules can be triggered to tautomerize [77]. That is, the two H atoms of H_2Pc can hop between two pyrrolic N atoms in the macrocycle cavity within the molecule, transitioning from one trans state to another (figure 4.2a). According to our DFT calculations, the DOS of the two tautomers is asymmetric. The calculated DOS for both the *trans* configurations at the energy corresponding to the molecule's HOMO resonance exhibit a four-fold symmetry (figure 4.2b up), thus it is identical for both configurations. The calculated DOS for both the trans configuration at the energy corresponding to the molecule's LUMO exhibit a two-fold symmetry (figure 4.2b down). Thus, they are equivalent to each other with a rotation of 90^o. Therefore, in order to track the tautomerization by recording the change in the current trace underneath the tip, we performed all measurements at a resonance corresponding to the molecule's LUMO.

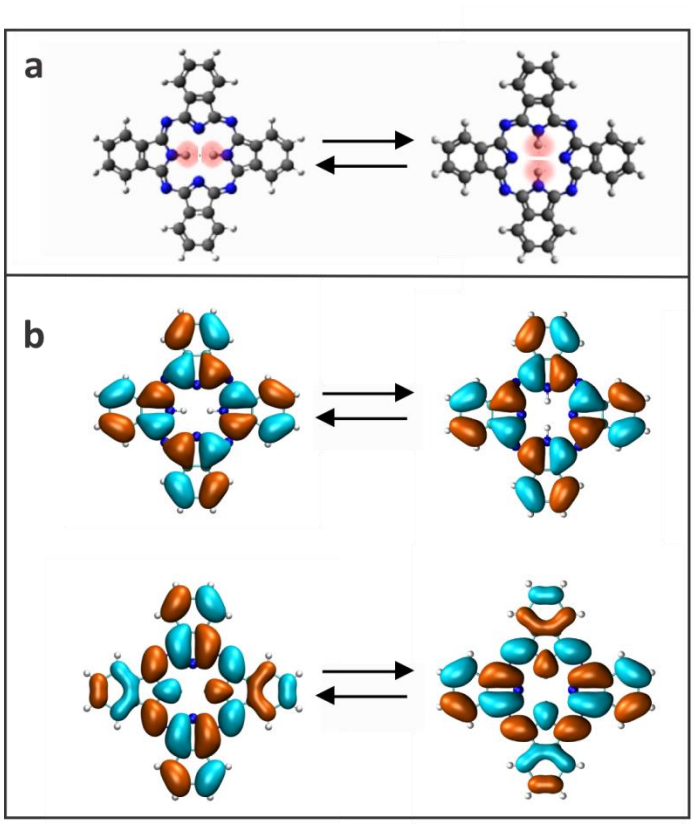

Figure 4.2: a) Ball and stick model showing the tautomerization reaction within the H_2Pc molecule. The locations of the hydrogen atoms are highlighted in red. b) DFT calculations of the H_2Pc molecule's frontier orbitals in the gas phase. HOMO and LUMO shown in the top and bottom half of the panel, respectively.

4.3 Inelastic excitation of the tautomerization reaction:

Although many instances of STM-induced tautomerization in aromatic tetrapyrrolic macrocycles have been shown in previous studies, [16,78-83] the exact mechanism remained obscure. The common belief is that the tautomerization occurs due to an inelastic tunneling process of the injected electrons. Previously, Kugel et el. suggested that the electrons enter the molecule and excite the N-H stretching mode, which subsequently induces the tautomerization [77]. According to their model, the energy of the first harmonic stretching mode $(\nu_1 = 1)$ lies just below the tautomerization barrier. Therefore, once the tunneled electron excites this mode, it could tunnel through the barrier of the tautomerization and induce the proton transfer. Another indication for an inelastically induced process, which was confirmed in our system as well, is a defined threshold voltage for the reaction induction and an observation of the same process for both bias polarities [78,83].

4.4 Probing the parameters to induce tautomerization:

As was explained in *chapter 4.3*, in order to trigger the tautomerization reaction in H_2Pc with STM, one should use tunneling electrons whose energies are sufficient to induce the tautomerization reaction. In order to locate the LUMO and the HOMO positions we performed dI/dV measurements on the adsorbed molecules. The repeated measurements reveal the location of the HOMO at –1.8 V and the LUMO at 0.9 V (figure 4.3). The main consideration for our choice of bias voltage and tunneling current was the stability of the signal during the measurements. Since the tautomerization switching frequency have shown to increase along with the applied current and bias voltage [77]. One would incline to apply the highest possible parameters. Albeit, since the H_2Pc molecules and the surface interact through week $\pi - \pi$ stacking, they are more susceptible to diffuse due to the tip induced electric field which is directly connected to the tip-sample distance and the bias voltage. In order to balance the inverse requirements for sufficient switching counts and the overall stability during the measurements several voltages and tunneling currents set-points have been tested. We conclude that our set-point parameters of 1.6 V and 10 pA have proven to provide the best balance of sufficient switching counts and a stable system. An example for the measurements sensitivity to the tip-sample distance is provided in figure 4.5.

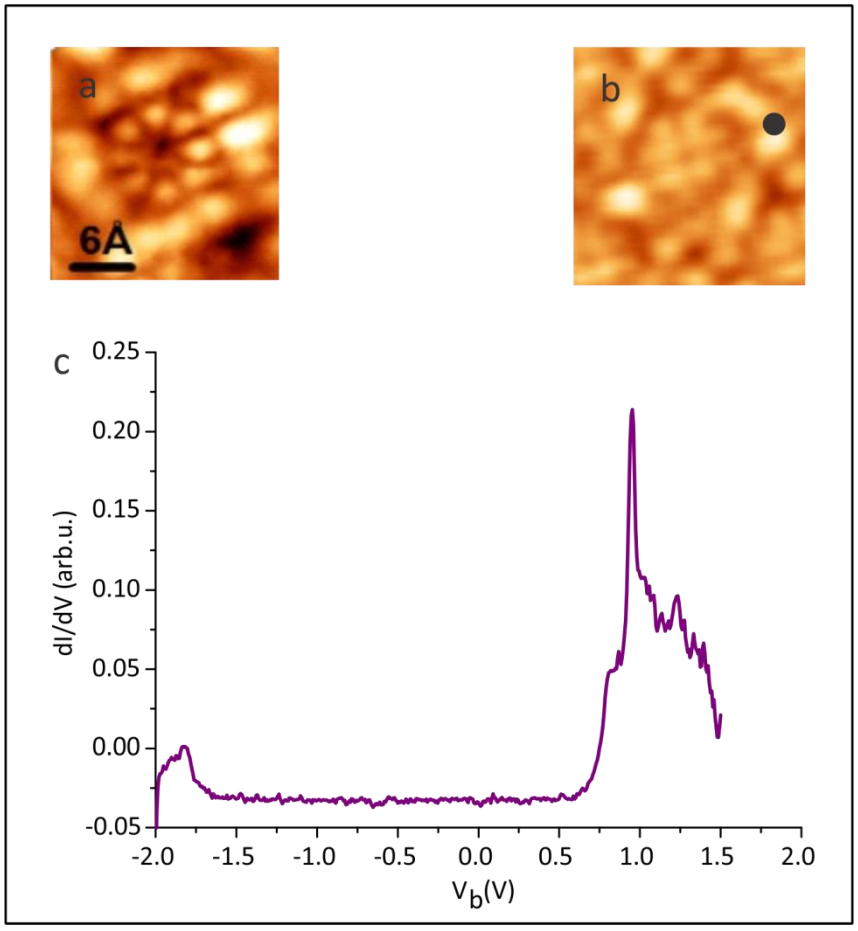

Figure 4.3: The H_2PC molecule's HOMO (a) and LUMO (b) and it differential conductance spectrum (c). The black dot represents the tip location.

4.5 Measuring the tautomerization frequency:

The tautomerization reaction is tracked by maintaining the tip in constant height mode (feedback loop off) and recording the fluctuations in the current as a function of time *t*. Since the molecules are physisorbed on the graphene and only interact through π-π stacking, the molecules are easily deflected by the electric field applied by the tip. In order to overcome this tendency, a stable and homogeneous molecular monolayer was formed on top of our graphene surface so that the molecular diffusion was greatly suppressed (figure 4.4a). Moreover, the monolayer raises the energetic barrier for molecular rotation around its center because this movement is hindered by the adjacent molecules. The monolayer was formed with organic molecular beam epitaxy (OMBE). The molecules were evaporated from a Knudsen cell onto the graphene surface held at $380\,°C$ for 50 minutes. Due to the strong spatial dependence between the position of the electron's injection into the molecule and the tautomerization rate, several injection locations have been examined [77,78]. For

each specific location the switching frequency was analyzed. In order to perform an accurate statistical analysis a high switching frequency is preferred; the location with the highest number of switching events was chosen for all measurements (black dot in figure 4.4a).

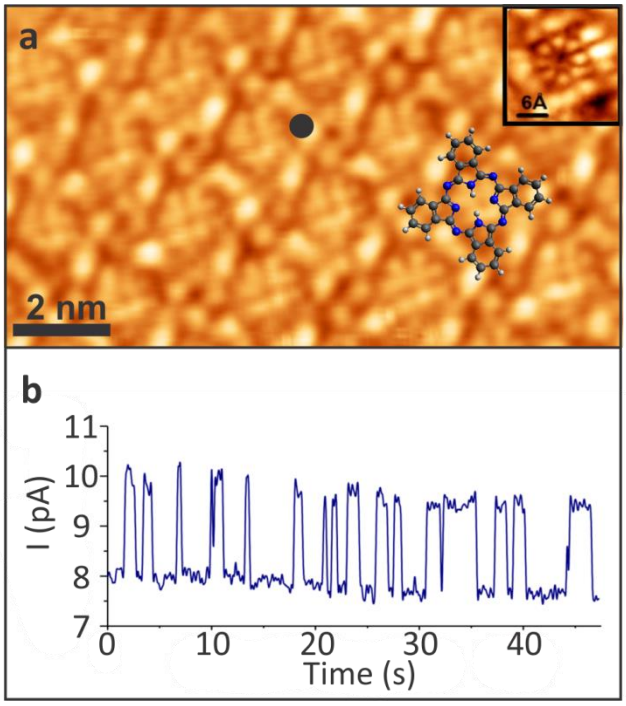

Figure 4.4: a) STM topography image of the H_2Pc monolayer on our graphene-FET device at an energy corresponding to the LUMO resonance state (V_b=1.6V). Inset: An H_2Pc molecule at an energy corresponding to the HOMO resonance state (V_b=-2.1 V). b) A telegraphic noise trace measured at the specific location marked by the black dot. Set-up parameters: I=10pA V_b=1.6V, V_g=0V.

During the tautomerization reaction, the DOS at the LUMO resonance will change (figure 4.2b). After positioning the tip, the feedback loop was switched off and the current signal trace was recorded in constant height mode. This way we were able to track the tautomerization switching frequency by relating it to the rate of transitioning between two clearly distinguishable state signals (figure 4.4b). To ensure the signal was always recorded at the same spot, between each measurement the molecules were rescanned to ensure that the tip position above the molecule had not been changed [78].

4.5.1 Telegraphic noise vs. tip height:

While measuring the current vs. time, the feedback loop is turned off. At this instant, the tip height is fixed according to the DOS beneath the tip. Figure 4.5 is a plot of the telegraphic noise being

recorded at the same exact location above a molecule. The white current trace was recorded when the feedback loop was turned off above a “lower” LDOS. In order to maintain its set point of 10 pA the tip approached closer to the surface and the feed-back loop was turned off. Therefore, during the reaction the current trace is switching between 10 pA and 18 pA, the latter corresponding to the current when the tautomerization occurred and the LDOS switched to a higher value. On the other hand, the red current trace was recorded when the feed-back loop was turn off above a “higher” LDOS. Hence, in order to maintain it set point of 10 pA the tip retracted further from the surface and the feed-back loop was then turned off. Therefore during the reaction the current trace is switching between 10 pA and 6 pA, where here the 6 pA correspond to lower LDOS after tautomerization.

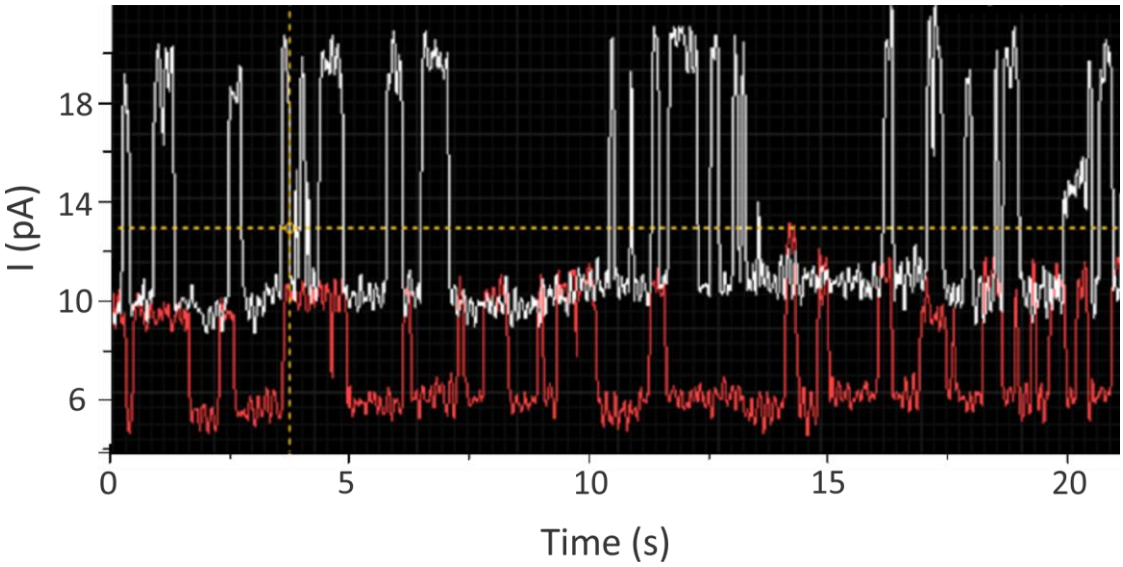

Figure 4.5: Two different current traces recorded at the same location above the molecule. The difference between the two traces depends on the location of the hydrogen atoms in the cavity when the feedback loop is turned off.

In all experiments the main considerations were tip stability and its ability to clearly resolve two-level telegraphic noise. Therefore, we always recorded the current trace corresponding to turning off the feed-back loop above a “high” density of states (red current trace in figure 4.5) since it has a higher stability.

4.5.2 Translating the RTN into frequency:

The next step in the analysis is translating the measured RTN signals into the switching frequency of the molecules. Since the signals are switching between two defined states one can calculate the

switching frequency (f) simply by dividing the total amount of transitions between the two states (s_w) in the total time of the measurement period (t_{tot}), according to $f = \frac{s_w}{t_{tot}} \frac{1}{s}$.

Due to the high number of measurements, a Matlab code was used to assist with the calculations. We used the provided *Signal Processing Toolbox*, specifically the pulse width function, in order to measure the number of transitions and the" lengths" of those states (figure 4.6).

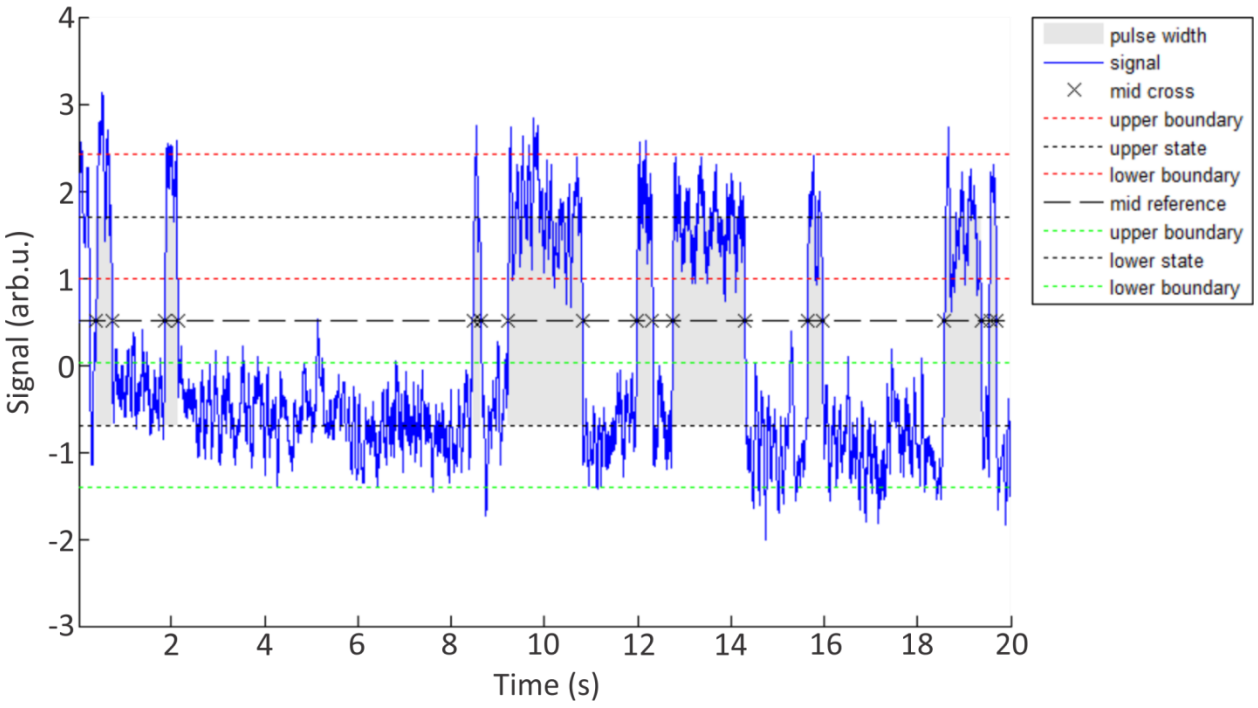

Figure 4.6: Image of a telegraphic noise trace analyzed by the Matlab function "pulse-width" from the "Signal Processing Toolbox" which we in use in our code.

For each measurement the upper and the lower telegraphic states were restricted to a top and bottom boundaries (red and green lines respectively) which could be varied. Any signal that crossed both of the borders (green to red or red to green) was counted as transition (marked as a cross) and any segment in between two transitions was notated as a pulse width (gray area in figure 4.6). To remove drift, a linear background signal was subtracted from some measurements.

4.6 The tautomerization switching frequency as a function of the applied gate voltage:

The switching frequencies were measured for several molecules across the monolayer at different positions with several tips. For each molecule, we recorded the tautomerization switching frequencies under the influence of different applied gate voltages ranging from -40 V to +40 V. When plotting the un-normalized measurements against the applied gate voltage the underlining trend is obscured by the effect of surface corrugation and its inert impurities. The amount and the gradient of the switching frequencies seem to differ from molecule to molecule, as well as the location of the maximum signal (Figure 4.7a). However, once the frequencies were normalized to its corresponding maximum value, a clear trend can be observed (figure 4.7b). The maximal frequency value measured when no (or small) gate voltage is applied and the switching frequency is reducing in a symmetrical fashion as the gate voltage is increased. The variation in the location of the maximal frequency is attributed to a local doping of the surface. The symmetric reduction is a clear indication for the influence of the tip-induced electric field on the reaction, since we assume that any charge effect will show a linear effect.

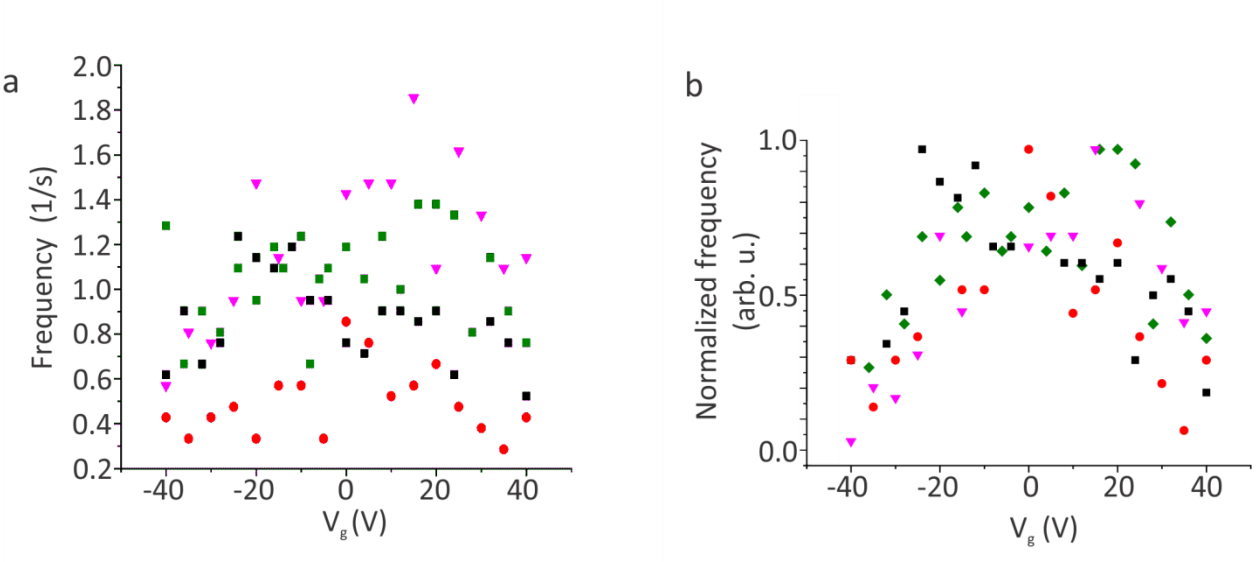

Figure 4.7: a) The un-normalized and b) normalized tautomerization frequency as a function of the applied gate voltage for each molecule. The different colors represent different molecules.

4.7 Potential mechanisms:

4.7.1 Modifying the tip-sample distance by sweeping the Fermi level with respect to the Dirac point:

By applying back-gate voltage to the Si layer we are able to change the DOS of the graphene substrate. That, in constant current mode, will adjust the tip-sample distance without any need to change the tunneling current or the bias potential between the sample and the tip, thus, isolating the electric field effect on the reaction. For each measurement, we recorded the shift in the tip location during the tautomerization frequency measurements. By calibrating our piezo we were able to record the initial location above the monolayer before we applied the gate voltage and the location after we turn on the back-gate voltage. The shift in the z direction of the tip (notated with Δz) was plotted against the gate voltage for all the molecules (figure 4.8). When applying the back gate voltage we are actually following the Dirac point with respect to the Fermi energy, changing the local DOS below the tip according to the DOS of the graphene. One should expect to see some correlation between the tip movement and the underlying graphene DOS. The inset in figure 4.8 presents a characteristic differential conductivity spectrum of a p-doped graphene/SiO_2/Si sample. A closer look reveals the high similarity between the measured frequencies and the spectrum. Sweeping the Dirac point with respect to the Fermi energy is equivalent to a shifting of the accessible states for the tip in a certain bias voltage [30]. The shift shown in figure 4.8 is the tip response to those changes in order to maintain the same set-point current, convoluted with the screening effects of the molecules and local surface conditions. Therefore, we showed the ability to control the tip-sample distance without changing the set-points conditions. By showing the same trend for all the molecules in a repetitive way, we are demonstrating our ability to control the tip-sample distance without changing the set-point bias voltage and tunneling current.

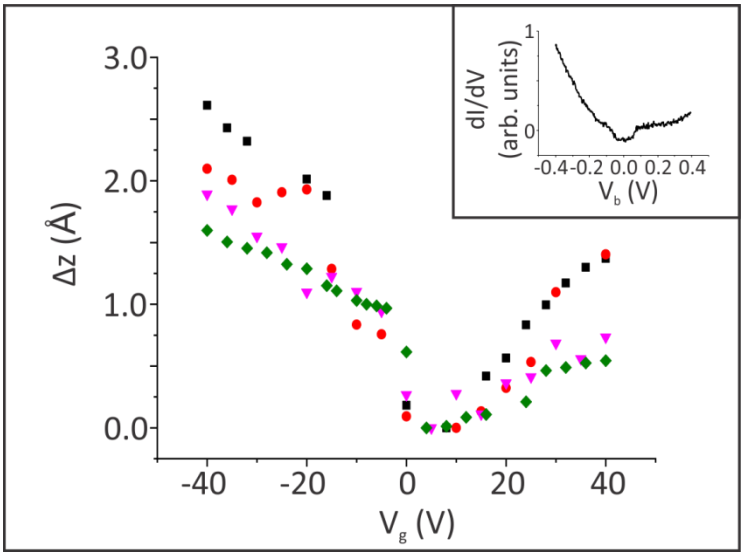

Figure 4.8: The relative shift in the vertical tip position plotted as a function of the applied gate voltage for each molecule. The different colors represent different molecules. Inset: Differential conductivity spectrum of our bare graphene device.

An immediate result of the shift in the tip vertical position is the consecutive change in the electric field applied by the tip. By using a simple plate capacitor model, where the surface and the tip are modeled as two conducting plates separated by a vacuum barrier which acts as a material with a constant dielectric, one can calculate the shift in the electric field applied between the tip and the sample as a function of the shift in the tip vertical position.

(4.1)

$$E_{\text{eff}} = \frac{U_{bias} + (\phi_{tip} - \phi_{substrate})}{d}$$

where E_{eff} is the effective electric field applied by the tip, U_{bias} is the potential applied between the tip and the sample, $\phi_{tip}$and $\phi_{substrate}$ are the work functions of the tip and the substrate correspondingly and *d* is the distance between the tip and the sample. For each measurement the initial location was set as a reference point and was subtracted from the location recorded after applying the gate voltage. After the electric field was calculated for all the molecules at each gate voltage, we plotted the switching frequencies as a function of the change in the effective electric field (figure 4.9). A clear correlation can be observed between the behavior of the switching frequencies and the calculated effective electric field. As we reduced the electric field applied by the tip (correlated to increasing the tip-sample distance) the switching frequencies is reduced. This is

also follows the correlation between the switching frequencies and the applied gate voltage. The gap in the electric field spectrum between $0\ \frac{V}{nm}$ and $-0.2\ \frac{V}{nm}$ at the section correlated to the negative gate voltage is assigned to the abrupt step in the DOS around 0 V.

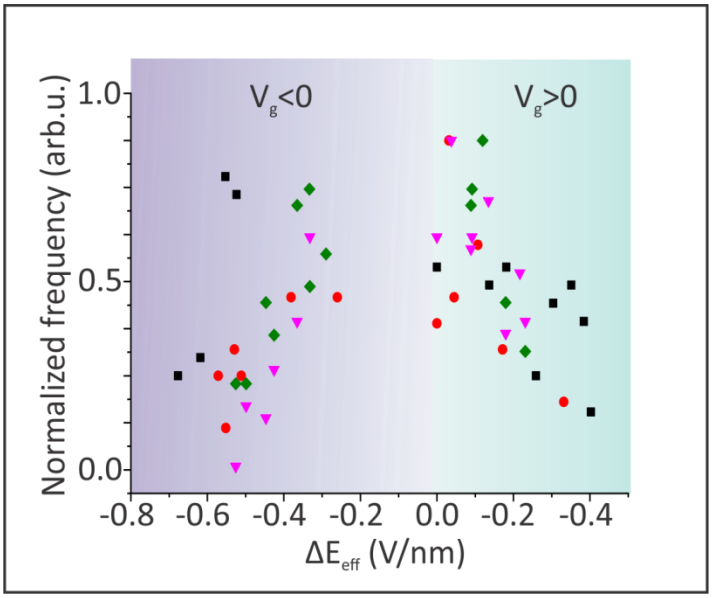

Figure 4.9: The normalized switching frequency as a function of the change in the tip induced effective electric field. The right side represents the positive gate voltage and the left side the negative gate voltage. The different colors represent different molecules.

Controlling the activation barrier energy as a function of the molecules tilting angles:

The clear dependency between the tip applied electric field and the adsorbed molecules indicates the existence of an intrinsic molecular dipole emerging during the tautomerization. It is known that in the presence of an electric field, a molecular dipole moment P will develop that will align with the field direction and reduce the overall energy of the system [73]. When the molecular dipole is aligned with the electric field a torque is being created and can be simplified to a cross product between the electric field and the dipole moment:

(4.2)

$$\tau = p \times E_{\text{eff}} = p \cdot E_{\text{eff}} \cdot \sin\alpha$$

The potential energy of the dipole in a uniform electric field will be:

(4.3)

$$E_p = -p \cdot E_{eff} \cdot \cos\alpha$$

Therefore the lowest potential energy in the system will occur when the dipole moment and the electric field are aligned to each other. Since H_2Pc is a planar molecule, any molecular dipole will be within the molecule plane. In order to cause some interaction between the electric field and the molecular dipole, some tilting angle must be involved in the process. That is compatible with our system in which the corrugation of graphene on top of the SiO_2 substrate is a known problem [33,34].

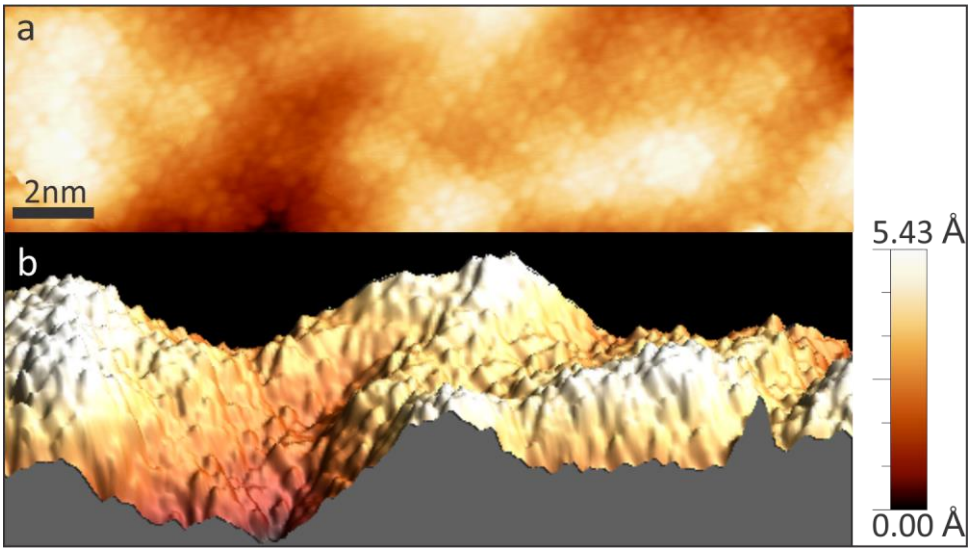

Figure 4.10: Two-dimensional (up) and three-dimensional interpretation of an STM topography image of an H_2Pc monolayer on top of our graphene device, the corrugation of the underling substrate is obvious in the latter.

In the case of a corrugated graphene surface we will expect the single molecular monolayer to follow the underlining roughness of the surface. Figure 4.10a shows a topographic image of the molecular network on our device recorded in constant current mode. By rendering the contrast variations in the image into a 3D image (figure 4.10b) it unveils a corrugated monolayer in which the molecules are oriented at a variety of angles. Thus, in the presence of a molecular dipole one should expect a strong dependency between the electric field effect and the molecules' tilting angles. Moreover, the diversity of the tilting angles together with the presence of underlying defects are probably the primary causes for the variation in the absolute values of the switching frequencies between different molecules (figure 4.7a).

Defining the Minimal Energy Path (MEP) and the activation barrier energy:

In order to understand the effect of the electric field applied by the tip on the tautomerization frequency, a more comprehensive understanding of the reaction path and its transitions is needed. Therefore, DFT calculations were performed by using the nudged-elastic-band (NEB) method [84] implemented in Quantum Espresso [85] in order to find the minimum-energy-reaction path between the two trans states. The calculations have been done both for a direct transition that bypasses the cis state, (thus two Hydrogen atoms are moving in the cavity together from one trans configuration to another, red curve in figure 4.11a) and for a path passing through a cis configuration (black curve in figure 4.11a). As it can be clearly seen from figure 4.11 the energetic barrier of a direct transition is 5 times higher than that of an indirect one which passes through one of the two cis configuration. Therefore we conclude the latter is the more probable reaction path.

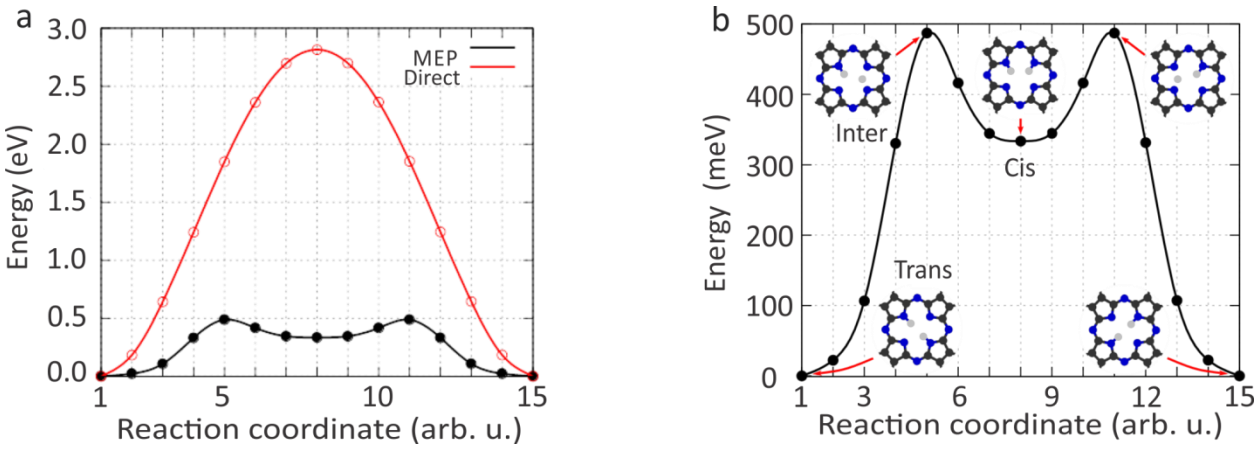

Figure 4.11 a) Comparison between the minimum energy path (MEP) for a passing through a cis configuration and the "direct" for a path that bypass the cis configuration (involving the simultaneous motion of the two H atoms between the trans states). b) The minimal energy path with the corresponding molecular configuration along the reaction path.

A closer look at the minimal energy path (figure 4.11b) reveals an intermediate complex between the trans and the cis conformations. The existence of transitions through the cis and the intermediate states is in accord with our initial assumption of the presence of a molecular dipole within the molecule. If we denote the initial state trans with energy of E_{trans} and the intermediate complex with the maximal energetic barrier as Inter with energy of E_{Inter}, one can define the activation barrier as $E_a = E_{Inter} - E_{trans}$with respect to the reference energy E_{trans}.

Defying the activation barrier from the minimal energy path, allow us to calculate the variation in it under the influence of external electric fields in ranges corresponding to the ones applied by our tip during the experiments for various angles.

Examining the influence of the molecular orientation on the activation barriers:

Before calculating the variation in the activation barrier as a function of the applied electric field, one should examine the adsorption configuration of the molecules on the graphene surface and its effect on the reaction. First, we examined the case in which the molecules adsorbed on the graphene in a configuration in which both of the trans states are geometrically equivalent with respect to the tilting axis (figure 4.12a). Thus, even in the existence of a tilting angle and an electric field, they will be energetically degenerate and any effect of the electric field on one of the trans states will also occur for the other. In the experiment, the molecular rotation due to the electric field is inhibited by van der Waals forces between the molecules and the graphene. Therefore the boundary conditions were simulated in our calculations by restraining the z-coordinates of the four carbon atoms encircled in green. We noted this configuration as "symmetric". Next we calculated the effect of a unified electric field on the tautomerization activation barrier as it was defined earlier in chapter 4.11, i.e. the direction of the electric field was taken always as parallel to the z-axis. The variations in the activation barrier were examined for several tilting angles in the range of $0^o \leq \alpha \leq 20^o$ (figure 4.12b). As it expected for $\alpha = 0^o$ (the molecule is lying flat on the surface) no significant variation is observed in the activation barrier as we vary the electric field. However, once we integrated the presence of tilting angles in our system a clear trend can be observed in the reaction's activation barrier. As we increase the applied electric field one can observed a clear reduction in the energetic barrier. Furthermore, the reduction become more prominent as we increase the tilting angles. We attribute the reduction in activation barrier to the increased interaction between the electric field and the dipole moment of the molecule during the intermediate state, as it was explained previously in chapter 4.10. When we increased the tilting angle of the molecule from the surface (inset figure 4.12b) the torque between the dipole moment and the electric field is increased, trying to align the dipole with the electric field direction, reducing the overall energy of the system.

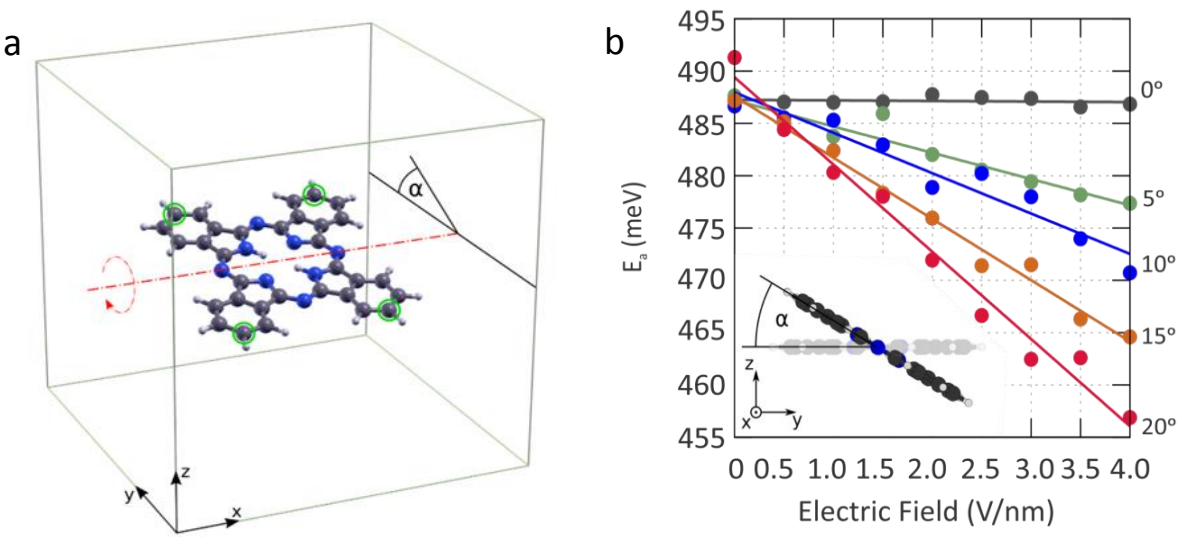

Figure 4.12: a) Simulated unit cell for the "symmetric" configuration. The tilting axis is represented by a dotted red line. In the experiment, the rotation of the molecule on graphene in the applied electric field is naturally suppressed by the stabilizing van der Waals interaction between the molecule and graphene. Thus, the z-coordinates of those four C atoms marked with green circles were fixed. b) The variation of the activation barrier as a function of the electric field and the tilting angle, for the "symmetric" configuration, extracted from the MEP calculations. The electric field is applied along the *z*-axis.

However, one should take into account also the possibility in which the molecule is adsorbed on the surface in an orientation in which the energetic levels of the trans states are not degenerate. That can lead to an interaction between the electric field and an induced dipole in the molecule, changing the energetic level alignment. Therefore, we next examined the adsorption configuration equivalent to a rotation of 45^o around the z-axis through the center point of the molecule. For consistency reasons we restrained the z coordinate of the four encircled carbon atoms. In this configuration noted as "asymmetric", in the presence of a tilting angle and an electric field the two trans states are not degenerated anymore. Therefore we differentiate them as trans 1, in which the hydrogen atoms are on the tilting axis (figure 4.13a) and trans 2, in which the hydrogen atoms are lying on an axis perpendicular to the tilting axis. In the trans 2 state the gradient between the z coordinates of the hydrogen atoms is maximal. Thus if we expect any variation in the energetic level of trans 2 and trans 1 states, it should be manifested here due to the interaction between the electric field and the molecular dipole. The calculations revealed that variation in the energy levels of trans 1and trans 2 were minor and achieved a maximal value of 2.8 meV. Therefore we conclude that the adsorption orientation on the graphene should not affect our initial observation. Indeed, further calculations of the variation in the activation energy as a function of a unified electric field for various tilting angels for the "asymmetric" configuration exhibit the same trend has been observed for the "symmetric"

configuration. Thus, as we increase the applied electric field we can observe a monotonic decrease in the reaction's activation barrier. The activation barrier seems less susceptible to the presence of the electric field. We attribute it to the minor variations in the energetic levels discussed previously.

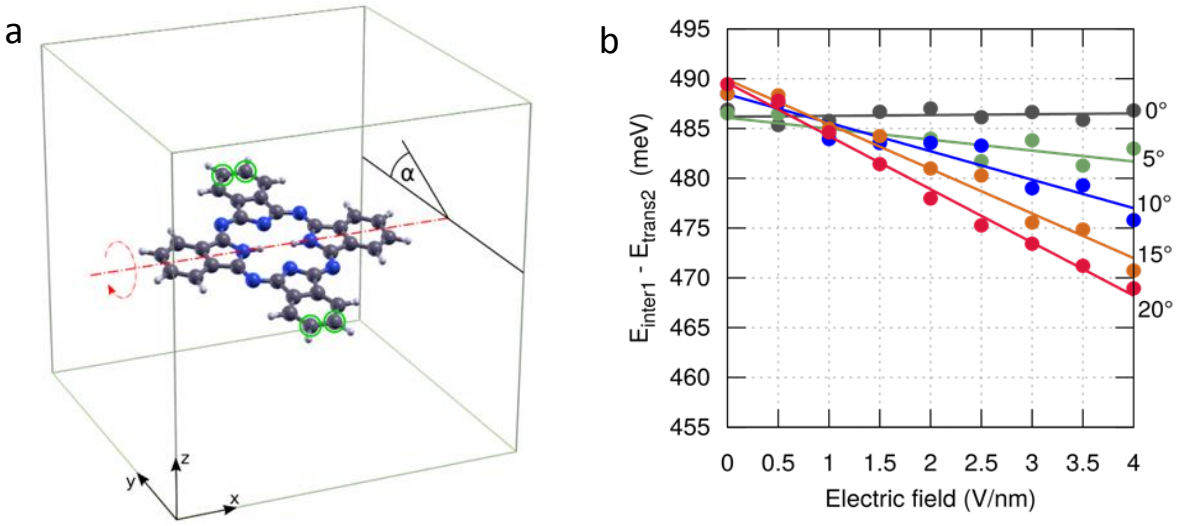

Figure 4.13: a) Simulated unit cell for the "asymmetric" configurations. The tilting axis is represented by a dotted red line. In the experiment, the rotation of the molecule on graphene in the applied electric field is naturally suppressed by the stabilizing van der Waals interaction between the molecule and graphene. Thus, the z-coordinates of those four C atoms marked with green circles were fixed. b) The variation of the activation barrier with the electric field and the tilting angle, for the "asymmetric" configuration, extracted from the MEP calculations. The electric field is applied along the *z*-axis.

4.7.2 The charging effect on the activation barrier:

In order to verify that the change in the switching frequency is due to the variation in the tip applied electric field, we examined all other plausible effects in our system that can influence the switching frequency. First, we analyzed the direct influence of the graphene charging on the reaction by measuring the Dirac point shifting with gate voltage (has been shown in *chapter 3.2.1*). From there, using DFT calculations, one can derive the correlation between the Dirac shift and the accumulated charges per atom on a graphene primitive cell (figure 4.14a). For a maximal applied gate-voltage of 40 V we can observe a shift of around 0.3 eV in the Dirac point location. This is equivalent to an overall charge of 0.002 e per graphene primitive cell (figure 4.12a).

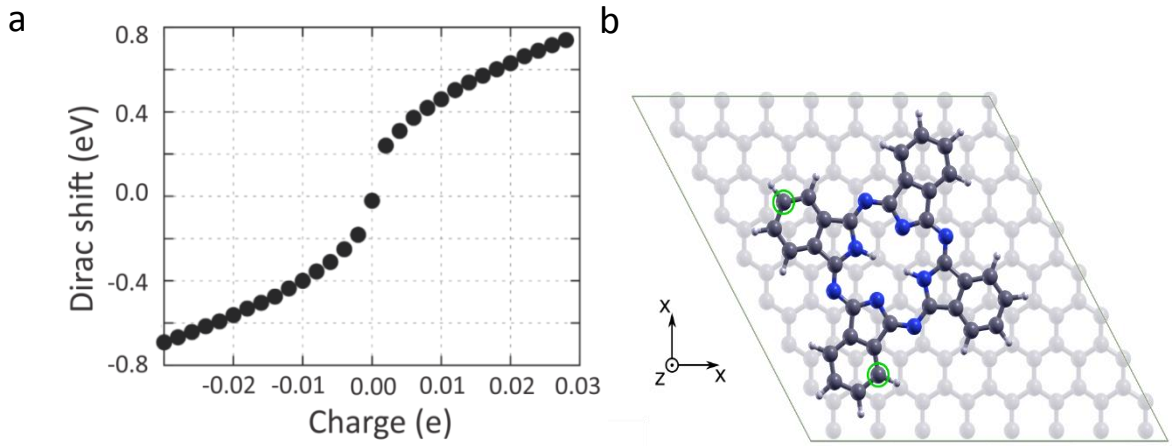

Figure 4.14: a) DFT calculation showing the Dirac shift as a function of the charging of the graphene surface. b) Simulated unit cell containing the H_2Pc molecule on top of a graphene sheet. The simulated cell contain 64 primitive graphene cells.

A closer look at our simulated unit cell (figure 4.14b) reveals that there are 64 graphene primitive cells in our simulated unit cell, therefore, the maximum charge which we can expect is 0.128 e per simulated unit cell. Thus, we examined the variations in the activation barrier for a range of charges per unit cell from +0.2e to -0.2e. We examined the charging effect on both activation barriers, from trans to cis (figure 4.15a) and from cis to trans (figure 4.15b). The calculations have been done in the absence of an electric field and in the presence of a field of strength of $2.5\ \frac{V}{nm}$ (red and green curves in figure 4.15 respectively). As it can be clearly seen, the change in the activation barriers is minor. For both conditions (with or without external electric field) the change in the activation barrier does not exceed 4 meV. Therefore we can conclude that the influence of the graphene charging on the activation barrier is not the determent factor in our experiments.

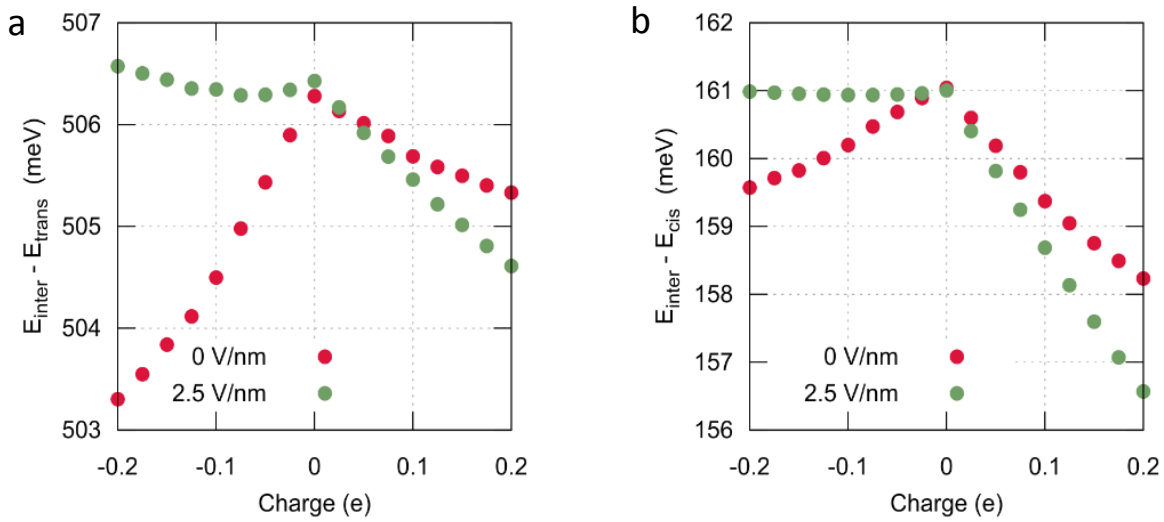

Figure 4.15: The variation of the activation barriers as a function of the total charge in the simulated unit cell at electric field strengths of $0\ \frac{V}{nm}$ (red dots) and $2.5\ \frac{V}{nm}$ (green dots) for transitions from trans to cis (a) and from cis to trans (b).

4.7.3 The shifting of the DOS:

Our second phenomenon in the system that we addressed was the possible shift in the molecule's DOS due to the gate voltage. By applying a back gate voltage to the sample one can shift the DOS of the molecules on the surface [38] [39], and consequently change the number of injected electrons which activate the reaction. Therefore, several DFT calculations have been done to examine the influence of the electric field on the molecules DOS (figure 4.16). From the three simulated spectra it is clear the DOS is shifting in a monotonic way with respect to the applied gate voltage, for a positive gate voltage the LUMO orbital of the molecule is shifted to higher energies and for negative gate voltage to lower energies. Since we observed a symmetric behavior of the switching frequencies around Vg=0 V we conclude that the shift in the energy levels cannot be the determining factor in the observed reduction of the frequency.

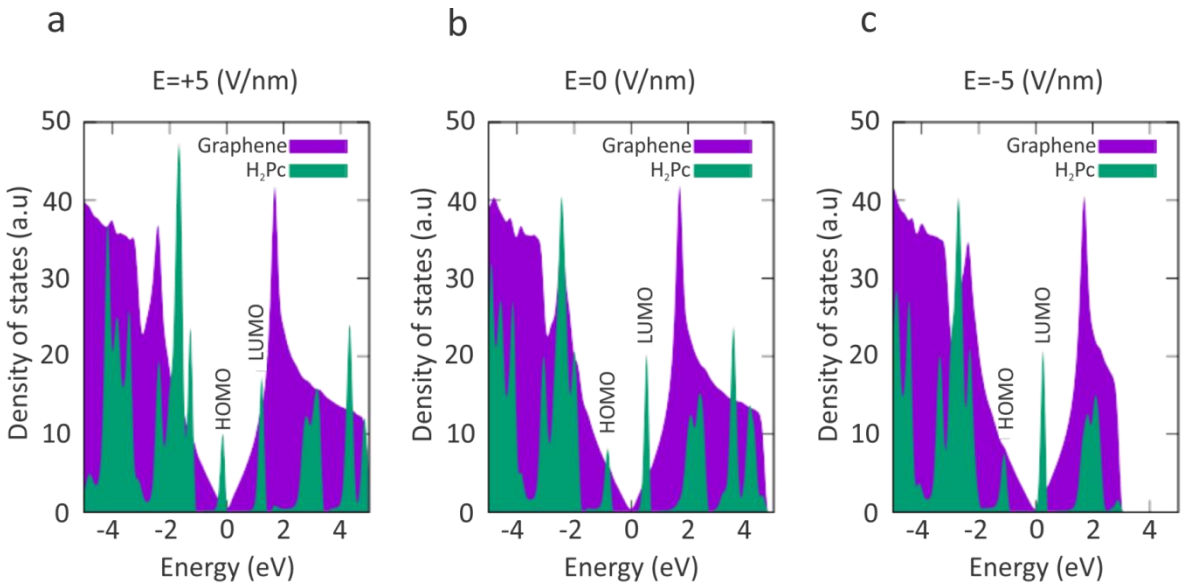

Figure 4.16: DFT calculations comparing the influence of an applied electric field in strength of $+5\frac{V}{nm}$ (a), $0\ \frac{V}{nm}$ (b) and $-5\frac{V}{nm}$ (c) on the molecules DOS.

4.8 Conclusions:

Based on the reasons written in chapter 4.7, DFT calculations agree well with our conclusions and clarify the relationship between the reduction in the activation barrier, the angle between the molecule's plane and the well-defined electric field. We not only showed for the first time the effect of an electric field on a reaction on the single molecule scale, but also exhibited a control over a reaction without changing its immediate surroundings.

In this chapter we demonstrated our ability to control the electric field applied by the tip by changing the tip position above the surface without changing the bias voltage or the tunneling current set point. This is possible through the combination of a graphene FET and a gate-tunable STM. This capability is unique to our device and can be used to isolate and examine the influence of a well-defined, strong electric field when its dependency on other parameters is present. Moreover, as a proof of concept we controlled the tautomerization switching frequency in Phthalocyanine molecules, only by varying the tip applied electric field. This is of particular importance since the tautomerization process is a prominent candidate to be used as molecular switches in future electronic devices as it describes a transition between two defined states without any external structural change to the molecule or to its local environment. We conclude that the corrugations of the surface together with the tip-applied electric field are the defining factors in the reaction

catalysis. As we increase the tilting angle of the molecules on the surface one should expect an increase in the oriented electric field influence on the activation barrier due to a stabilizing of partially charged transitions states.

Chapter 5:

Control over the bond length of molecular hydrogen on a G-FET through graphene charging:

5.1 Introduction:

Hydrogen, the lightest element in the universe, is a prominent candidate for future clean-energy sources where fossil fuels are replaced. Therefore, a lot of effort has been invested in recent years to examine its adsorption conditions on different substrates [86]. In recent years there is an increasing interest in graphene-based systems as plausible candidates for hydrogen storage [87], due to its advantages compared to other candidates such as good mechanical properties, high surface area and weight. Albeit, due to the molecular hydrogen low affinity it is extremely challenging to trap and examined, especially on graphene which is known to be inert. While Natterer et al. had presented measurements of adsorbed molecular hydrogen on a graphene layered device, they were performed in the presence of an underlying metal substrate [47]. Thus, the molecular hydrogen DOS was not fully decoupled from the surface. A measurement of the molecular hydrogen DOS that is maximally decoupled from the substrate is still sought after. In the following chapter we will demonstrate how we were able to achieve this, and in addition, through surface modification, induce the physisorption of H_2 molecules and manipulate their bond length by means of electrostatically doping the graphene surface with a back-gate voltage. In order to achieve our goals a new layered device with the structure graphene/SL-hBN/SiO_2/Si has been constructed. The new layered device was produced accordingly to the apparatus portrayed in *chapter 3.2.2*. Our improved procedure allowed us to transfer and clean CVD grown hBN with a thickness of 1-8 atomic layers on top of a SiO_2/Si substrate, sequentially capping it with a home-grown graphene layer. The device was then characterized by means of topographic and spectroscopic measurements as elaborated in *chapter 3.2.2*. The device exhibits negligible leakage current which enabled the surface to be charged without any increase in the device temperature. This allowed us to perform the experiment without experiencing any thermal drift. An illustration of our experimental system is presented in figure 5.1.

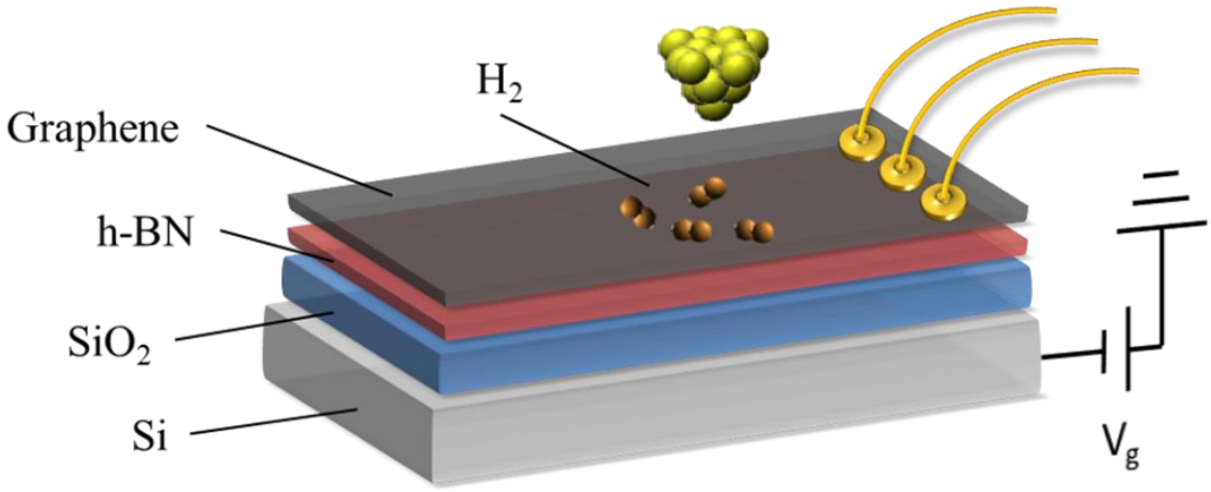

Figure 5.1: A schematic of our graphene/SL-hBN/SiO_2/Si device with the physisorbed hydrogen molecules.

In order to trap the H_2 molecules on top of the graphene surface, certain favorable adsorption sites are needed. Since the graphene and hBN have different thermal expansion coefficients, during the annealing and cooling process one can form nano-wrinkles on the surface [88]. Those nano-wrinkles are known to vary the surface work-function [89] which creates local regions that are more favorable for adsorbates. To create these regions, the sample was annealed under UHV conditions at 720K and then cooled down to a temperature of 4.8K. This substantial temperature gradient was sufficient to form the aforementioned nano-wrinkles. Next, the STM chamber was then warmed up to 27K in the presence of hydrogen molecules and swiftly cool down back to 4.8K. With this procedure, we were able to induce the adsorption of molecular hydrogen at those purposefully made 1D line defects.

5.2 Detection of H_2 molecules on graphene:

Figure 5.2a presents a 3D rendering of a topographic scan of the periodic nano-wrinkles. The black square (figure 5.2a) frames the region of interest (ROI) where our measurements were done. By examining the differential conductance channel outside the ROI (figure 5.2b) one can observe strong perturbations which are not present in the ROI (figure 5.2c). Furthermore, repeated spectroscopic measurements inside the wrinkle revealed strong negative differential resistance (NDR) features (figure 5.2d). Repeated measurements away from the wrinkles exhibited the characteristic spectrum of a pristine graphene surface (figure 5.2e). The NDR features appeared at $V_b = \approx \pm 50\, mV$ and at $V_b = \approx \pm 10\, mV$ and are characteristic of a saturated inelastic tunneling process through physisorbed H_2 molecules [46 90 47].

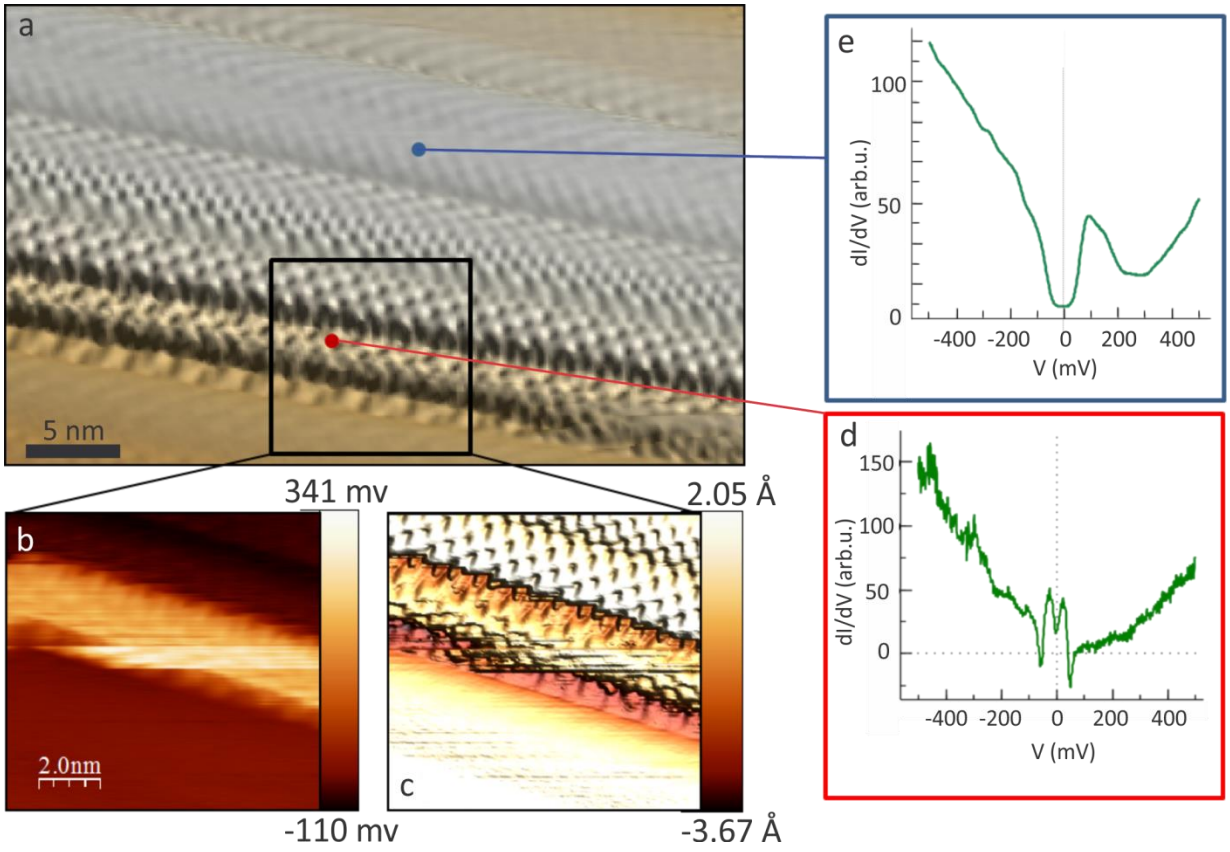

Figure 5.2: a) H_2 molecules are trapped within a graphene nano-wrinkle formed due to graphene and its underlying hBN having different thermal expansion coefficients. Saturated IETS indicates presence of H_2 molecules (red frame) while outside of the wrinkles the device exhibits the characteristic graphene spectrum (blue frame).b) The dI/dV channel and the c) topographic image were acquired with V_b=500 mV, I=50 pA, V_g=0 V, the bias spectra were taken with I=50 pA, V_g=0 V. d) dI/dV spectrum measured inside the wrinkle, exhibiting NDR features. e) dI/dV spectrum measured outside of the wrinkle exhibiting a pristine graphene spectrum.

Figure 5.3 shows the numerical derivative of a differential conductance spectrum taken on top of the molecular hydrogen. The weaker feature at $V_b = \approx \pm 10\, mV$ appears at energies corresponding to the molecular hydrogen vibrational mode according to the relation:

(5.1)

$$E_{vib} = \hbar\nu\left(n + \frac{1}{2}\right) \equiv \Phi$$

where $\hbar$ is the reduced Planck constant, ν is the vibrational excitation energy and n is the vibrational quantum number. The hydrogen vibrational mode is usually located at $\Phi = 5\, meV - 20 meV$ and changes according to the local environment.

The more prominent feature at $V_b \approx \pm 50\, mV$ corresponds to the rotational mode of molecular hydrogen and obeys the relationship:

(5.2)

$$E_{rot} = \frac{\hbar^2 J(J+1)}{2I} \equiv \Omega \equiv V_{rot}$$

where J is the rotational mode quantum number and I is the molecule's moment of inertia, defined as $I = \mu d^2$, where μ is the reduced mass and d is the molecular distance in a homonuclear diatomic molecule. For molecular hydrogen the rotational excitation transition $J = 0 \rightarrow 1$ is forbidden and therefore cannot be observed [91]. Therefore, the lowest allowed rotational transition is $J = 0 \rightarrow 2$ which in gas phase, corresponds to $\Omega = 44.2\, meV$ [47,92,93].

In the following chapter we will address the stronger rotational mode features Ω and analyze their shift as a function of the tip-sample distance and electrostatic doping of the surface.

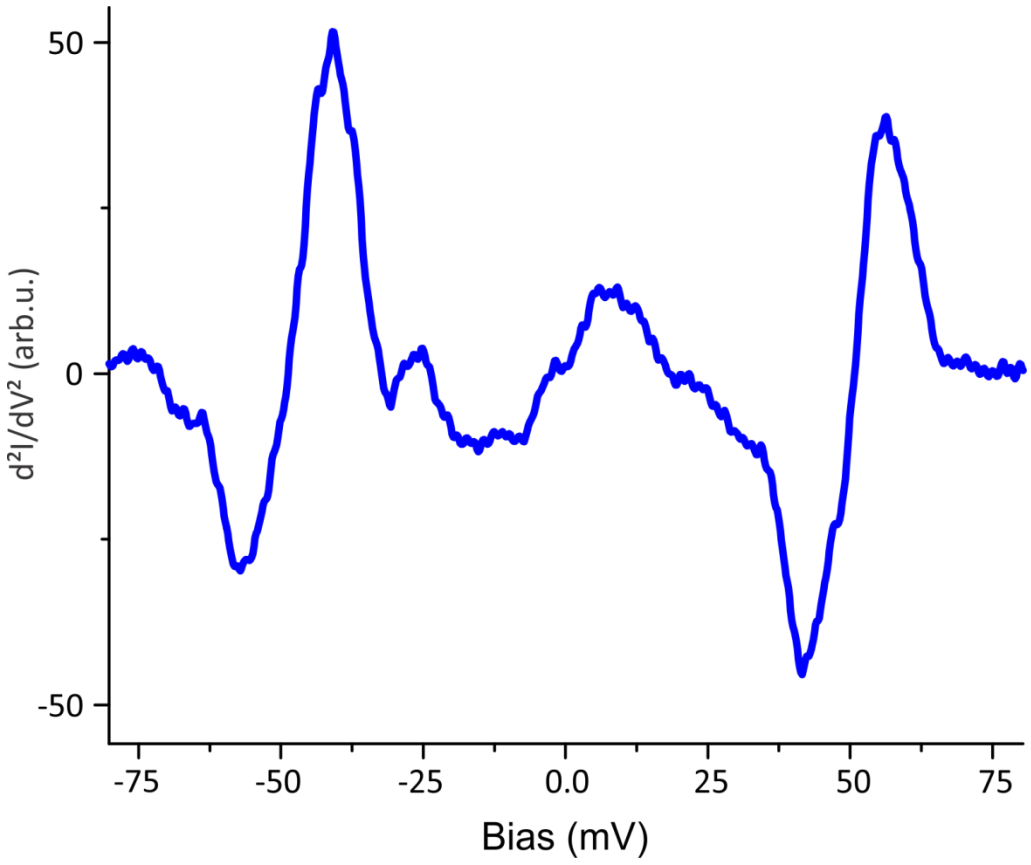

Figure 5.3: A d^2I/dv^2 spectrum reveals the characteristic saturated-IETS features of molecular hydrogen. The spectrum was taken at V_b=500 mV, I=50 pA, V_g=0 V.

In order to gain more a comprehensive understanding of our measurements, we employed two different models to describe our observations. The Baratoff-Persson model elaborates on the interaction between the tip and the adsorbed molecule, allowing us to deduce information about the coupling of the molecule to the surface. The Gupta model paints a similar picture, but puts emphasis on the interaction between the molecule and the surface, allowing us to deduce information regarding the charge transfer between the molecule and the surface. Therefore both models can be seen as describing different aspects of the same system.

In the following we will provide a brief explanation of both models.

5.3 Applying the Baratoff-Persson model:

The Baratoff-Persson model presented first in 1987 [94] [95], suggests that under specific conditions, an interaction between the STM tip and a molecular resonance on the surface can result in resonant tunneling with enhanced vibrational excitation. As illustrated in figure 5.4, the specific model consists of an STM tip terminating with a single atom, that acts as an s-orbital denoted here as $|b\rangle$ with a DOS of ρ_b, and a single molecular orbital on the surface notated as $|a\rangle$ with a DOS of ρ_a. The potential difference between the tip and the molecule-sample complex with their corresponding energies of ε_F and $\bar{\varepsilon}_F$ give rise to a molecular resonance centered at ε_a. Once the electron is tunneled through the vacuum barrier it can become trapped in the broad molecular resonance while losing an energy quantum of Ω, with a lifetime on the order of $\tau \sim \frac{\hbar}{\Gamma}$ where Γ is the molecular resonance width. The inelastic process is manifested as dips in the dI/dV curve at energies corresponding to $\pm\Omega$.

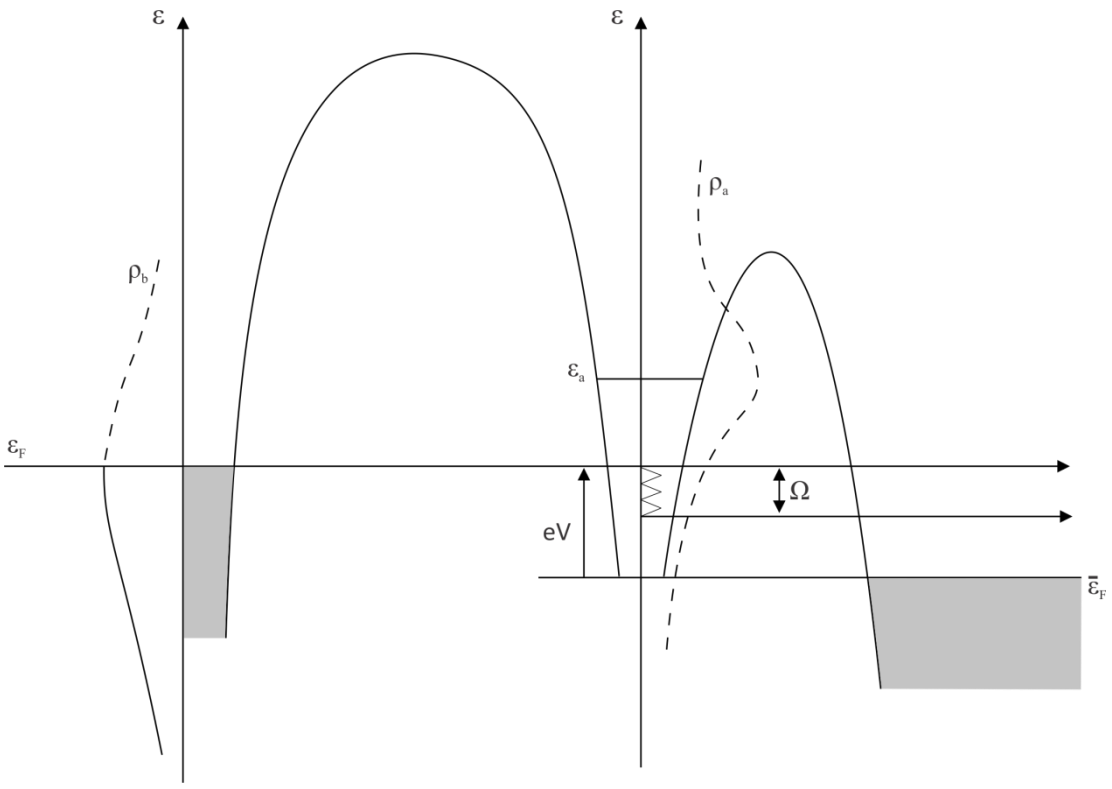

Figure 5.4: An illustration of the energy diagram describing the tip and the adsorbed molecular orbitals and their respective DOS ρ_b and ρ_a , as well aselastic and inelastic tunneling processes.

The resulted dI/dV spectrum can be described according to:

(5.3)

$$\sigma = \frac{(\delta\varepsilon)^2}{(\varepsilon_a + eV_t)^2 + \left(\frac{\Gamma}{2}\right)^2} \cdot \left\{ \begin{array}{l} \dfrac{(\varepsilon_a + eV_t - \Omega)^2 - \left(\frac{\Gamma}{2}\right)^2}{(\varepsilon_a + eV_t - \Omega)^2 + \left(\frac{\Gamma}{2}\right)^2} \cdot \Theta \cdot (eV_t - \Omega) \\ -\dfrac{\Gamma}{\pi} \cdot \dfrac{\varepsilon_a + eV_t - \Omega}{(\varepsilon_a + eV_t - \Omega)^2 + \left(\frac{\Gamma}{2}\right)^2} ln \left| \dfrac{eV_t - \Omega}{\Delta} \right| \end{array} \right\}$$

where $\delta\varepsilon$ is the coupling factor, ε_a is the energetic location of the molecular resonance, eV_t is the electron initial energy, Ω is the excitation threshold frequency and Δ is the cutoff energy which defined as $\Delta \ll \Gamma$ in order to ensure the integrability of the model and Θ is the broadening function which imitates the thermal broadening and the lock-in modulation. While the model was originally proposed to describe the process of inelastic tunneling into vibrational modes of a chemisorbed molecule on a metal surface, as it was later shown by Natterer et al. that the model can also be applied to energies corresponding to the rotational modes [47] of physoisorbed molecular hydrogen. Since variations in the conductance spectrum due to inelastic tunneling can be small, it is preferable to also examine the second derivative where these small differences are accentuated. These considerations are shown in figure 5.5.

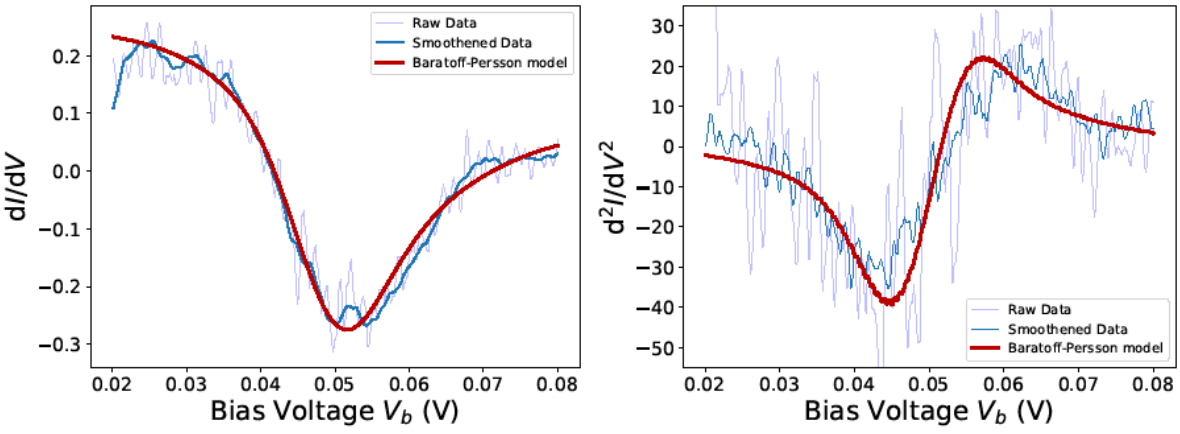

Figure 5.5: The recorded dI/dV (left) and its numerical derivative d^2I/dV^2 (right) and their fits, based on the Baratoff-Persson model. The extracted parameters for the excitation energy, molecular resonance and coupling parameter are: $\Omega = 49.13$ meV, $\varepsilon_a = -163.7\ meV$ and $\delta\varepsilon = 222\ meV$.

The fit is in good agreement with both the first and second derivatives. According to the model parameters, the NDR features appear whenever the molecular resonance ε_a is at a negative energy with respect to its Fermi level. This arrangement of energy levels is in agreement with Natterer et al. for molecular hydrogen physisorbed on hBN/Rh. In their work the authors measured the rotational excitation energies of hydrogen molecules on different surfaces. In particular, they observed NDR features for H_2 on a hBN/Rh substrate, whose molecular resonance was located near $\varepsilon_a = -200\ meV$, in contrast to $\varepsilon_a = +1\ eV$ seen in other systems. The authors attribute this pronounced shift in the energy position to a local variation in the surface work function due to its moiré pattern. Furthermore, the authors suggested this this specific molecular system is a prominent candidate for molecular gating which can be observed via its excitation energy. Thus, in order to further understand and analyze the nature of the NDR features here, a second more specific model was employed.

5.4 Applying the Gupta model:

This model was introduced in 2005 by Gupta et al. [46]. In their work they analyzed the differential conductance spectrum of physisorbed H_2 molecules on a metal substrate. Their modeling of its non-linear conductance was treated with a two state system, in which the conductance of the elastic channel is diminished due to the presence of an inelastic channel. Thus, if σ_o is the initial conductance of the elastic channel and σ_1 is the conductance of the elastic channel in the presence of an inelastic channel, the relation between the two conductances satisfies $\sigma_o > \sigma_1$. The contribution of the elastic channel to the total conductance is a function of the saturated inelastic channel occupation.

A schematic of the Gupta model is illustrated in figure 5.6, with the four notated energetic states as follows: 1- the tip, 2- the molecule's ground state, 3- the molecule's excited state and 4- the surface. The different conductances are defined in which: σ_{up} is the conductance from the molecule's ground state to its excited state, σ_{down} is the conductance from the molecule's excited state to the sample (i.e. relaxation conductance) and V_{rot} is the excitation threshold (notated here as the threshold to the excitation of the molecule's rotational modes). In the extreme case of $\sigma_o \gg \sigma_1$, the quantity $\frac{dI}{dV} < 0$ i.e. NDR features will appear in the conductance spectrum.

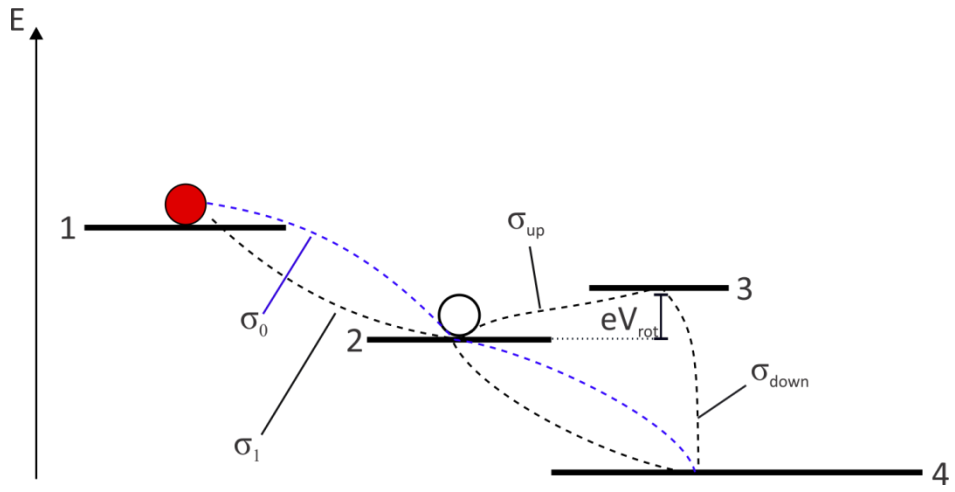

Figure 5.6: Energy levels diagram illustrating the elastic and inelastic tunneling processes according to the model suggested by Gupta et al.

The differential conductance spectrum can be described according to:

(5.4)

$$\frac{\mathrm{dI}}{dV} = \begin{cases} \sigma_0, & V < V_{rot} \\ A + \dfrac{B}{\left(1 + \dfrac{V - V_{rot}}{C}\right)}, & V \geq V_{rot} \end{cases}$$

where A, B and C are defined as:

$$A = \frac{\sigma_{up}(\sigma_1 + \sigma_{down}) + \sigma_{down}(\sigma_0 + \sigma_{up})}{\sigma_{up} + \sigma_{down}}$$

$$B = \sigma_{up} \frac{(\sigma_{up} V_{rot} - eS)(\sigma_1 - \sigma_0) + 2\sigma_{up}\sigma_{down} V_{rot} + eS(\sigma_{up} - \sigma_{down})}{(\sigma_{down} V_{rot} + eS)(\sigma_{up} + \sigma_{down})}$$

$$C = \frac{\sigma_{down} V_{rot} + eS}{\sigma_{up} + \sigma_{down}}$$

Here, S is the spontaneous relaxation rate of the excited state.

Next, we employ this model to fit our measurements (figure 5.7).

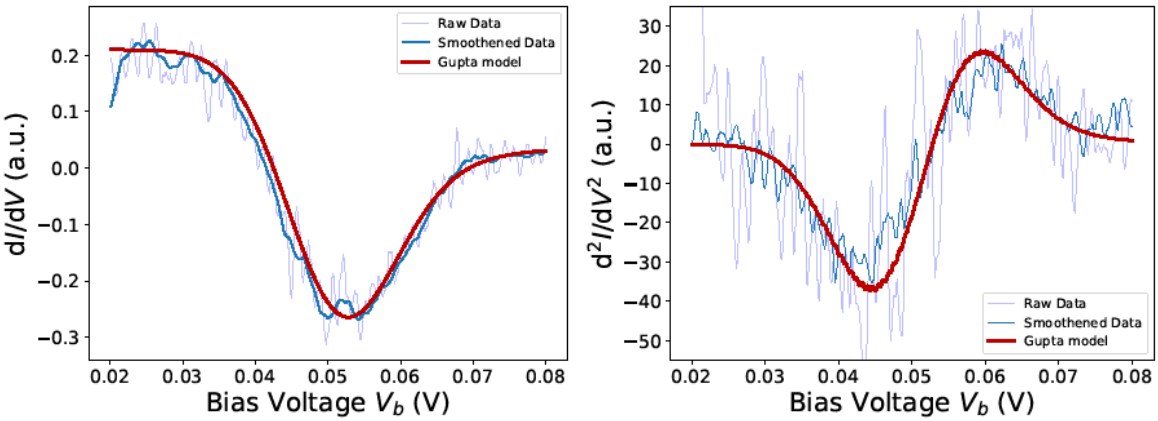

Figure 5.7: The recorded dI/dV (left) and its numerical derivative d^2I/dV^2 (right) spectra and their fit, based on the Gupta model. The extracted parameters for the excitation energy and the relaxation conductance are: $V_{rot} = 49.6\ \text{meV}, \sigma_{down} = 18.5\ \frac{mA}{V}$.

The model also fits well with our measurements. Since our measurements can be described by both the Baratoff-Persson and the Gupta model, in the following we compare their parameters by analogy to get an accurate and unprecedented picture of the process.

5.5 Adsorption configuration of the molecular hydrogen on top of the graphene:

As explained in chapter 4, measuring with an STM introduces a well oriented electric field into the system being studied. This field is known to change the adsorption conformation of hydrogen molecules on the surface. Wang et al. [92] have previously shown by means of DFT that on Au(110), under the influence of the STM tip, the hydrogen molecules prefer to have a vertical adsorption geometry over a horizontal one. As the interactions of hydrogen on graphene are also mainly through weak van-der-Waals interactions and have low adsorption energies, it stands to reason that hydrogen on graphene will also prefer a vertical geometry. While previous theoretical work examining the molecular hydrogen adsorption configuration on graphene showed that a horizontal configuration is favorable [96], those calculations were also done in the absence of a well-oriented electric field. Therefore, several calculations were carried by our collaborators from Ludwig-Maxmilians-University (LMU) in Munich by Prof. Christian Ochsenfeld and Dr. Jörg Kussmann in order to examine how H_2 adsorbs on the graphene surface under the influence of an electric field (figure 5.8).

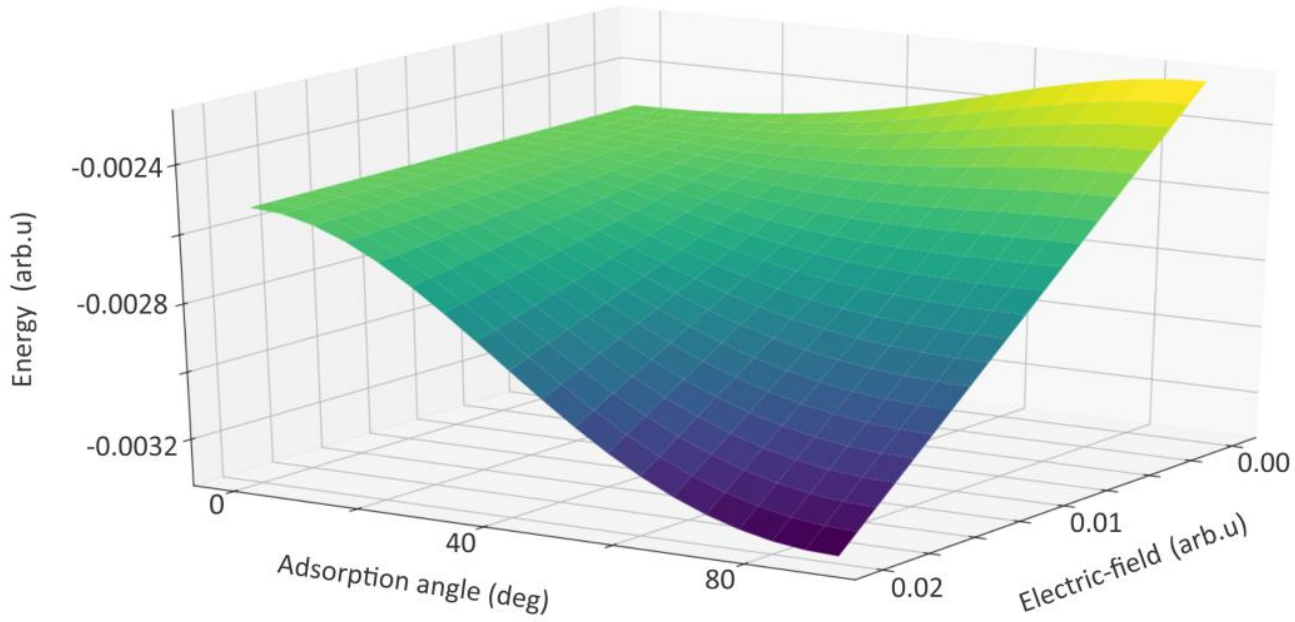

Figure 5.8: The energy landscape of the molecular hydrogen adsorption angle on the graphene surface as a function of the applied electric field.

The calculations shown in figure 5.8 reveals that under the influence of electric fields comparable to that in our system, the molecular hydrogen adsorption configuration will be vertical since the induced dipole in the molecule tends to align with the electric field direction.

5.6 Analyzing the current dependence:

During the experiment all measurements had been repeated for several tunneling-current set points i.e. I=30 pA, 60 pA, 100 pA and 200 pA. For each set point, both the first and second derivative had been fitted with both the Baratoff-Persson and the Gupta models with excellent agreement. The good fits allowed us to deduce the coupling factor between the molecule and the surface (from the Baratoff-Persson model) and the relaxation conductance of an electron from the molecule to the surface (the Gupta model). This will enable us to gain a deeper understanding of the interaction between the molecule and the graphene.

Recall that as the current set-point is increased the tip-sample distance is decreased due to the inverse relation between the current and the tip height. When reducing the tip-sample distance, the vertically adsorbed hydrogen molecule which is trapped in the cavity between the tip and sample undergoes a sort of “squeezing” effect that increases the interaction of the lower H atom with the metal surface, which subsequently elongates the molecular bond length due to the change in its

electrons density [93] [92]. Therefore, one should expect a similar process to occur in our system and expressed in both models. Figure 5.9 displays the relationship between the Gupta model's relaxation-conductance of an electron from the molecule's excited state into the surface (blue), and the Baratoff-Persson model's coupling factor (black) as a function of different tunneling-currents. A similar trend can be seen in both models, namely that the conductance/coupling increases together with the tunneling-current in a linear manner. As we "squeeze" the molecule in the cavity more towards the surface we increase the overlapping of the molecule and the surface orbitals, which is then being reflected in both parameters. This behavior is not only in good agreement with previous reports but also demonstrates the strength of utilizing both models in portraying a fuller picture of the physical processes that are occurring on the surface.

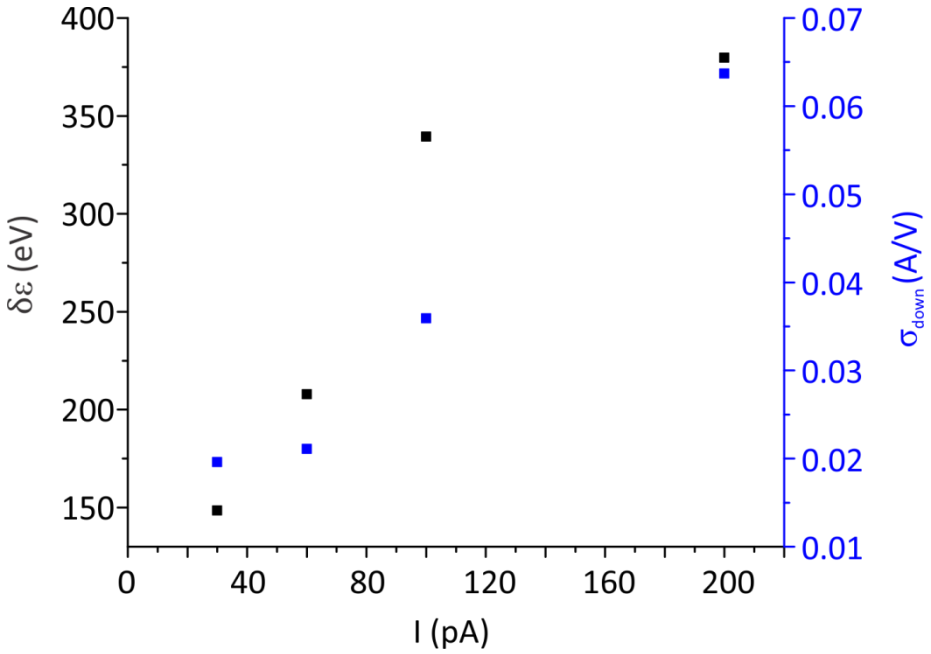

Figure 5.9: The coupling coefficient $\delta\varepsilon$ from the Baratoff-Persson model (black) and the relaxation conductance σ_{down} from the Gupta model (blue) as a function of different tunneling-currents (I=30 pA, 60 pA, 100 pA and 200 pA).

5.7 Graphene charging effect on H_2 adsorption:

Next we examined the influence of electrostatically doping the surface on which the molecules reside via a back-gate voltage. In order to observe only the influence of the doping effect and to eliminate any variation in the tip-induced electric field, in the following experiments the back-gate voltage was applied after the feedback loop was turn off. In doing this, the tip height is kept fixed throughout, thus the electric-field is constant across the full set of measurements presented here.

Therefore, if one would sweep the gate voltage from –40V to +40 V, one should expect a change in the tunneling current according to the shift of the graphene DOS. Figure 5.10 is a plot describing the relationship between the tunneling current and the applied gate voltage. As expected, as we sweep the gate voltage from –40V to +40 V we see a decrease in the tunneling current down to a minimum point at a critical voltage and then an increase in the current beyond it. The minimum represents the gate-voltage needed to align the graphene Dirac point to the tip Fermi level at a bias voltage of 100 mV. Since the graphene is highly p-doped, a positive gate-voltage needs to be applied to compensate for the surface intrinsic doping levels.

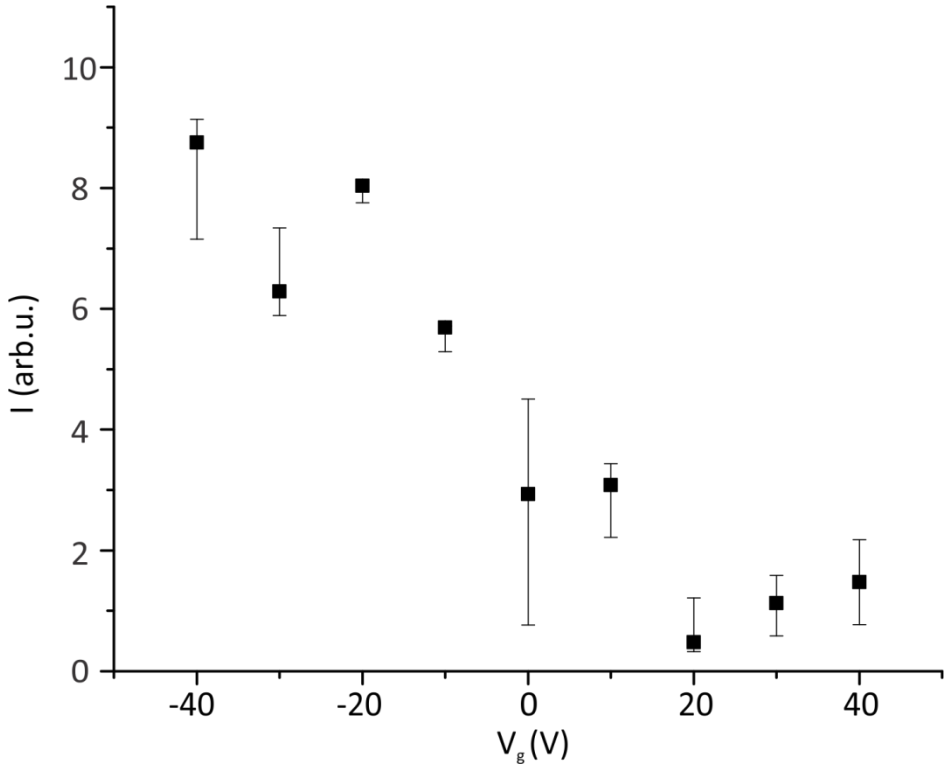

Figure 5.10: The tunneling current as a function of V_g in a constant height mode. All measurements were repeated several time and the median value has been taken.

For each set point, dI/dV spectra have been recorded while applying back-gate voltages in the range of $-40\ V \leq V_g \leq +40\ V$. Since the signal recorded in IETS measurements is relatively weak, in order to monitor the influence of the back-gate voltage on the NDR features the numerical derivative of the differential conductance, i.e. d^2I/dV^2, is also measured. Figure 5.11a is a waterfall diagram of several d^2I/dV^2 spectra under the influence of a back gate voltage, where a small but notable monotonic shift can be observed in the Fano-shape feature of the rotational excitation energy. In order to present the shifts more clearly a heat map of the same spectra is provided as well (figure

5.11b). A clear monotonic shift is observed in the threshold excitation energies towards higher values as we sweep the back-gate voltage from $-40\ V \leq V_g \leq +40\ V$.

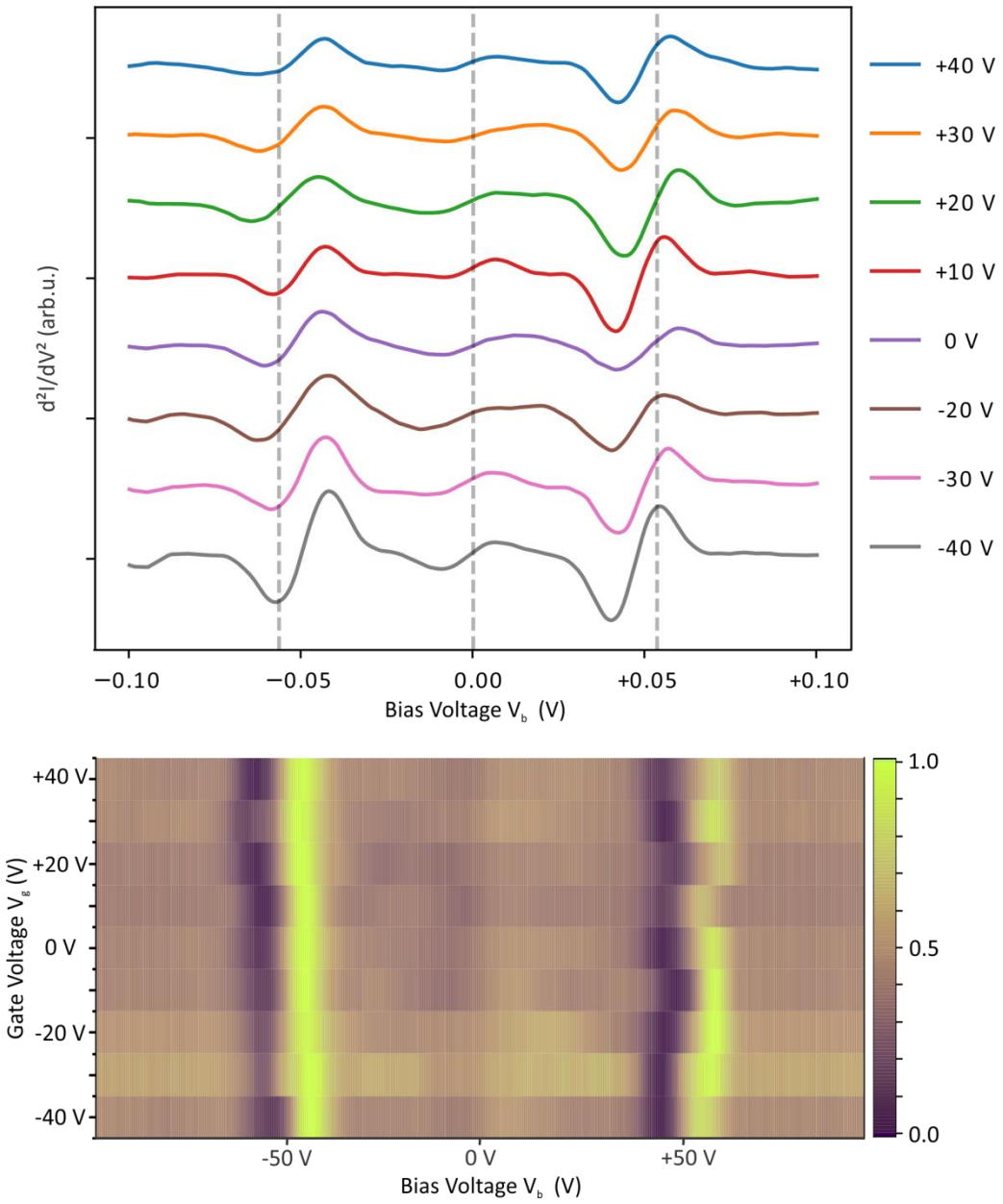

Figure 5.11: a) a waterfall diagram of several d^2I/dV^2 spectra under the influence of different back gate voltages b) a heat map of the d^2I/dV^2 spectra as a function of the gate-voltage.

In order to show the shift in the excitation energy in a clearer way, both the Baratoff-Persson and Gupta models were again employed, whose fitted excitation energies were plotted against the applied gate-voltage for different the set-points (figure 5.12). For the Baratoff-Persson model, the rotational energy is Ω (figure 5.12a) and for the Gupta model the analogous parameter V_{rot} (figure5.12b) was plotted. Both models exhibit the same trend, in which the rotational excitation

threshold energies of the molecules are shifting in a monotonic manner towards higher values as we increase the gating from –40 V to +40 V.

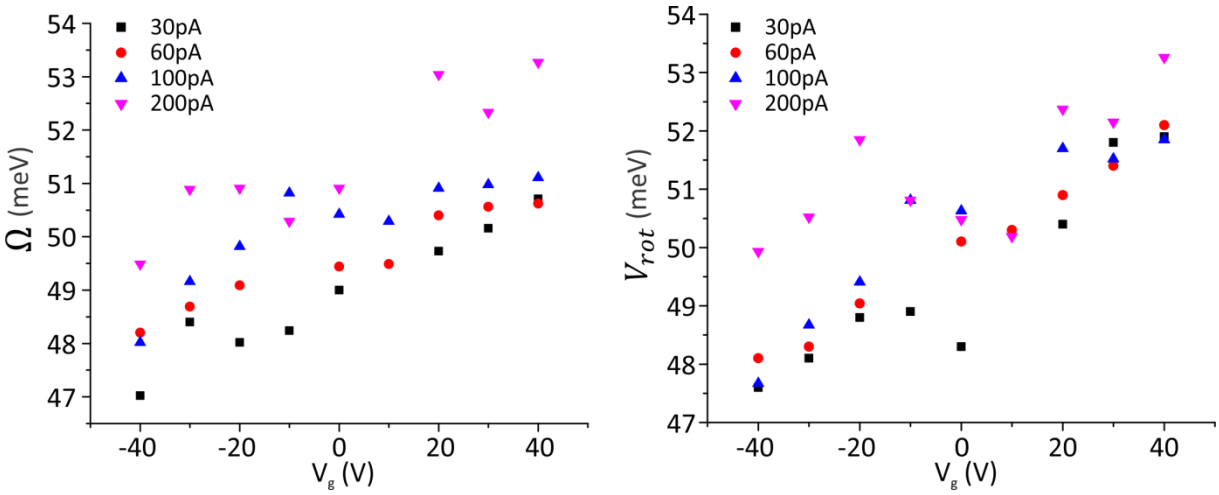

Figure 5.12: a) the excitation energies Ω from the Baratoff-Persson model and b) the excitation energies V_{rot} from the Gupta model as a function of the gate-voltage for different set points.

By substituting the moment of inertia of a homodiatomic molecule $I = \mu d^2$, into equation 5.2, we can obtain the relationship:

(5.7)

$$E_{rot} \equiv \Omega \equiv V_{rot} = \frac{\hbar^2 J(J+1)}{2I} = \frac{\hbar^2 J(J+1)}{2\mu d^2} = \frac{c}{d^2}$$

As it can be clearly seen the energy of the rotation and consequently its position in the spectrum in Figure 5.11 is inversely related to the square of the bond length of the molecule d^2. Thus, any changes in the bond length will be expressed in the energetic location of the rotational peak. The rotational excitation peak shifting to higher energies indicates that the molecular hydrogen bond length is reduced as we sweep the gate-voltage from -40 V to +40 V. A closer look at figure 5.12 reveals a change in the inclination of the shift for $V_g \geq 20\,V$, where the slope is attenuated. In order to explain this observation, one should have a second look at figure 5.10 which describes the change in the tunneling current as a function of the applied gate-voltage during our measurements. Once we cross the minimum point $(V_g \geq 20\,V)$, the current increases but with a smaller slope than the values obtained when $V_g < 20\,V$. This effect originates from the shape of the LDOS of the graphene at the vicinity of the Dirac point. Similarly, figure 3.15 shows that the curve is not symmetric around the Dirac point. This asymmetry means that the LDOS changes slower for $V_g \geq 20\,V$ than for

$V_g < 20\ V$, thus the charging of the surface for $V_g \geq 20\ V$ is reduced, which explains the attenuated slope in the shift of the rotational excitation peaks.

Moreover, all the measurements portrayed in figure 5.12 have been repeated for different tunneling currents. For both Ω and V_{rot}, as we increase the tunneling current, i.e. reducing the tip-molecule tunneling-junction, we can observe an increase in the values of the rotational peaks. This is in good agreement with our observation in chapter 5.6 and directly corresponds to our conclusions that derive from figure 5.9, suggesting that both of the effects occur in our system at the same time. Therefore, we have shown that by modifying the doping level of our device we were able to tune the hydrogen molecules bond length as a function of our applied gate-voltage.

In order to verify these assumptions, the coupling coefficient of the molecule to the surface ($\delta\varepsilon$) from the Baratoff-Persson model and the conductivity of the relaxation channel of the molecule's excited state (σ_{down}) from the Gupta model were extracted and plotted as a function of the gate-voltage (figure 5.13 a and b respectively). Since both of the analogous parameters relate to the electron transfer process from the molecule to the surface, plotting them against the gate-voltage should give us an indication of any change due to the charging effect. Both parameters show a decrease in their values as we sweep the gate-voltage from $-40\ V$ to $+40\ V$. This is in excellent agreement with our assumptions, that as we sweep the gate-voltage from negative values to more positive values we are altering the surface from p-doped to n-doped by changing its charge carrier density in a continuous manner. Thus, by tuning the molecule's interaction with the graphene, it manifests as a reduction in the coupling/charge-transfer between the molecule and the surface. The same attenuation in the slope can be observed for $V_g \geq 20\ V$, which originates in the structure of the DOS in the vicinity of the Dirac point. As expected, the monotonic trend is observed for all the measured tunneling currents. By this we have verified our assumptions about our abilities to tune the interaction of the molecules with the graphene surface.

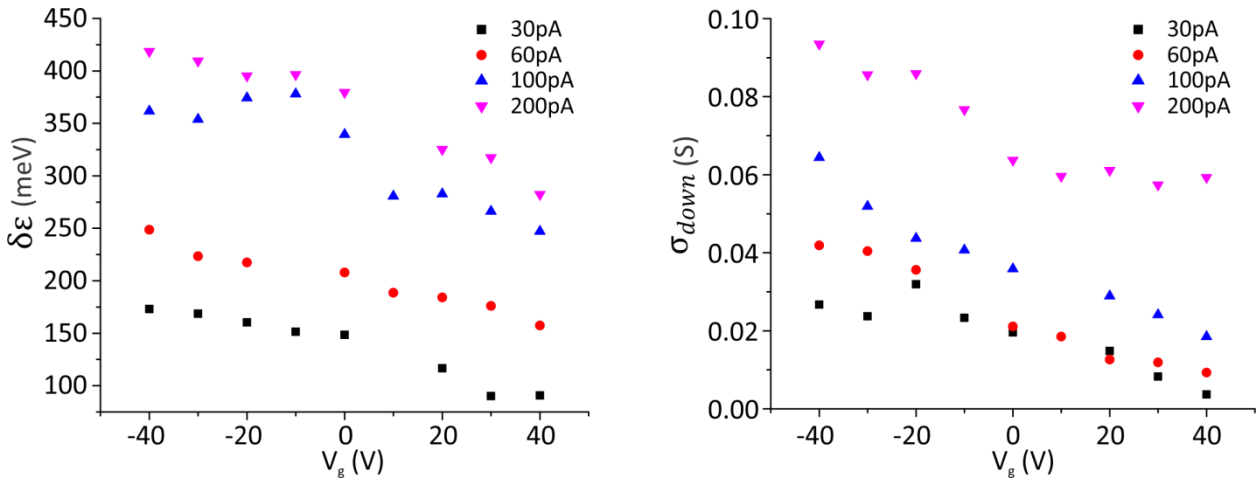

Figure 5.13: The coupling coefficient $\delta\varepsilon$ from the Baratoff-Persson model (left) and the relaxation conductance σ_{down} from the Gupta model (right) as a function of the gate-voltage for different set points.

5.8 Conclusion:

To conclude, we have shown that we trap molecular hydrogen on graphene by surface modification and manipulate its bond length by means of electrostatic doping via back-gate voltage application. Our measurements were reinforced and supported by utilizing two well-known theoretical models, which by combining them, resulted in additional insight into the physical process that occur between adsorbed molecules and the surface. As explained earlier in *chapter 2.2.3*, applying a back gate voltage changes the charge carrier concentration on the graphene layer, which subsequently changes the interaction between the adsorbed molecules and the surface. We had demonstrated how the change in the tip-sample distance due to the change in the tunneling-current changes the interaction of the molecules with the surface. This causes a decrease in the charge density of the molecule's bond, leading to a change in its bond length. We are demonstrating here that the same can also be accomplished by charging the surface. When a negative back-gate voltage is applied, the graphene becomes more positive which increases the interaction between the hydrogen "lower" atom with the surface, reduces the charge density in the molecule's bond, therefore elongating it, as is exhibited in the H_2 excitation shift towards lower energies. The reverse process also occurs when a positive bias is being applied through the back-gate voltage, which increases the bond charge density and therefore reduces the bond length and shifts the excitation energies towards higher values. The observed shifts in the energies are substantial and can reach up to a 10% change. Furthermore, the increase in the set-point value is also examined and shows the same trend as explained earlier. In summary, we demonstrated that our device enables unique capabilities in

manipulating and observing molecular reactions by means of electrostatic doping of the graphene surface.

Chapter 6:

Conclusions:

In this thesis we have demonstrated a new method to control reactions at the single molecule level by combining tailor-made G-FETs and a home-built Gate-STM. When a back-gate voltage is applied to the bottom of the G-FET, charge is accumulated on the graphene layer which results in a shifted DOS. The accumulated charge can be detected in two different ways. In the first method, the gate-voltage is applied when the STM's feedback loop is turned on. The tip will then adjust its distance from the surface in order to maintain the same set-point tunneling current. By doing so, it is possible to control the tip induced electric field by modifying the tip-sample distance without changing the bias voltage or the tunneling current. In the second method, the feedback loop is turned off prior to applying the gate voltage. This way, the tip maintains its initial distance from the surface, and thus, the electric field remains constant. By fixing the tip-sample distance one can exclude the influence of the tip-induced electric field and observe only the influence of the graphene's charging.

In *chapter 4* the first method was employed in order to demonstrate the effect of a highly oriented electric field on the tautomerization reaction of H_2Pc. We deposited a monolayer of H_2Pc on top of a graphene/SiO_2/Si device and monitored the H_2Pc tautomerization reaction by recording the current. Then, we tuned the tip-induced electric field by applying an additional back-gate voltage. We observed a systematic reduction in the switching frequency of the tautomerization as we increased the gate-voltage. With the support of DFT calculations we concluded that the activation barrier of the tautomerization reaction is reduced due to the tip-generated electric field. Moreover, the result showed that if the tilting angle of the molecule is increased due to some increased surface corrugation, a greater influence of the electric field on the reaction barrier is expected. Thus, we have demonstrated for the first time, our capacity to probe the effect of a highly oriented external electric field on a reaction at the single molecule scale.

In *chapter 5* the second method was employed to demonstrate the effects of graphene charging on adsorbed hydrogen. We induced the physisorption of molecular hydrogen on top of a graphene/SL-hBN/SiO_2/Si device through surface modification. A NDR arising from physisorbed hydrogen was detected through STS measurements. The IETS spectra were fitted to the Barattof-Persson and Gupta models. Both models described the same physical phenomena but from different aspects. The

Barattof-Persson model focuses on the interaction between the tip and the molecule, while the Gupta model focuses more on the interaction between the molecule and the surface. In our fitting, both models show good agreement with the experimental data. When a negative gate voltage was applied, the graphene became charged with positive charge carriers, which increased the interaction of the surface with the “lower“ hydrogen atom and reduced the charge density in the molecule’s bond and elongated it. That change is manifested as a shift of the NDR features to lower energies. When a positive gate-voltage was applied, the system experienced the inverse process, in which the bond length decreased, and manifested as a shift of the NDR features to higher energies. The observed shifts were significant and reached up to 10% change. The results clearly show that the charging of the graphene shifted the NDR features which indicated that a change in the bond strength of the adsorbed hydrogen molecule had occurred.

Chapter 7:

Outlook: Towards atomically layered transistors:

A G-FET device is based on a gate-electrode, an insulating dielectric material, a source electrode, a graphene channel and a drain electrode. The same components implemented in an STM setting are constructed from a highly doped Si wafer, whose bulk is used as the gate electrode, its naturally grown ~300 nm oxide layer is used as the dielectric material, a graphene sheet added on top is used as the conductance channel, and the bias-voltage contacts and tip acts as the source and drain electrodes (*figure 2.7*). Throughout this thesis we have characterized several devices that overcome several inherent flaws of this device motif. The most prominent problem involved the SiO_2 dielectric layer. As was shown in *chapter 4*, the presence of SiO_2 induces surface corrugations which then create local charge puddles in the graphene [33] [34] [35]. They result in an inhomogeneous charging of the surface. We have shown in *chapter 3.2.2* that adding another buffer layer of CVD-grown hBN between the SiO_2 and the graphene notably improves the overall device properties in terms of surface cleaning, corrugation and charging. Furthermore, we expect that eliminating the presence of the thick SiO_2 as the dielectric material and replacing it with an atomically thin hBN will enhance the back-gating effects that include surface charging, energy level shifts and tip-induced electric fields. To date, atomically thin hBN-graphene heterostructure devices have been mostly explored by relying on exfoliation methods that produce hBN flakes on the order of a few dozen micrometers in diameter. However, these devices have been proven to be challenging to explore using STM due to the difficulty of approaching these small devices with an STM tip.

New developments in the field of large scale growth of multi-layer hBN via CVD [97] have now opened opportunities to construct a new layered device which is substantially thinner and STM compatible. Therefore, in the current chapter we will present our endeavors to develop a new layered graphene based device with the general structure of graphene/ hBN/metal (Fe, Cu, Mo). Our goal is to construct several G-FET devices with different hBN thicknesses so they can be characterized by following the Dirac point shift as a function of the applied back-gate voltage.

The construction of the devices was mainly divided into two approaches: 1. lifting a single stack of multi-layer hBN onto a polished metal substrate, and 2. several consecutive lifting procedures of transferring single hBN layers onto a polished metal substrate. Both methods have their advantages

and disadvantages. The single layer hBN is of higher quality than the multi-layer hBN with respect to its coverage, cleanliness and its surface conditions. However, in order to prevent the formation of any leakage current between the graphene surface and the back-gate electrode, a thickness of at least 5nm of hBN is needed [98]. Therefore, in order to produce an isolating layer of at least 5nm thickness of hBN, several consecutive lifting procedures are needed. However, multilayer lifting procedures also increase the chances of encountering metal and organic-solvents residues in between the layers, whose presence can induce corrugations and increase the probability of forming a leakage current. Therefore, a 3rd approach has been developed, in which a multilayer hBN stack is lifted to construct the leakage current barrier which is then subsequently capped with a single layer of hBN. Since ML-hBN is usually grown on a thin Fe film instead of the commonly used Cu film, a modification of the etching process is needed. We have found that the Fe film is more robust to etching than the Cu film. Therefore, the concentration of the APS etching solution was increased to 2 M and the etching time was elongated to 36 h. The remaining procedure was kept identical as described in *chapter 3.2.2*.

All the preliminary results presented in this thesis were taken on a device produced via the 3rd approach which has shown the most promising results. The large scale AFM topographic scan of the sample (figure 7.1a) exhibits a clean surface, with substantially less PMMA residues than has been observed in previous devices. However, we observed several areas on the device that were corrugated due to wrinkles originating from the metal thin film and the transfer process. The STM image presented in figure 6.1b reveals a moiré pattern caused by the mismatch in lattice constants between the graphene and the underlying hBN. As expected, the surface corrugation has been reduced drastically due to the absence of SiO_2 and it is in the sub-angstrom range. Furthermore, as was mentioned in *chapter 3.2.2* the cleaning procedure (under UHV conditions) seems to be far more efficient than in SiO_2 based devices, as we eliminated the presence of any dangling bonds and surface traps originated from the SiO_2. A closer look at the large scale STM image reveals an atomic resolution of graphene. A fast reverse Fourier transform has been done on the sample in which the reflections originated from the moiré pattern (turquoise hexagon) and the reflections correspond the graphene (green hexagon) are all visible in the inset of figure 7.1b.

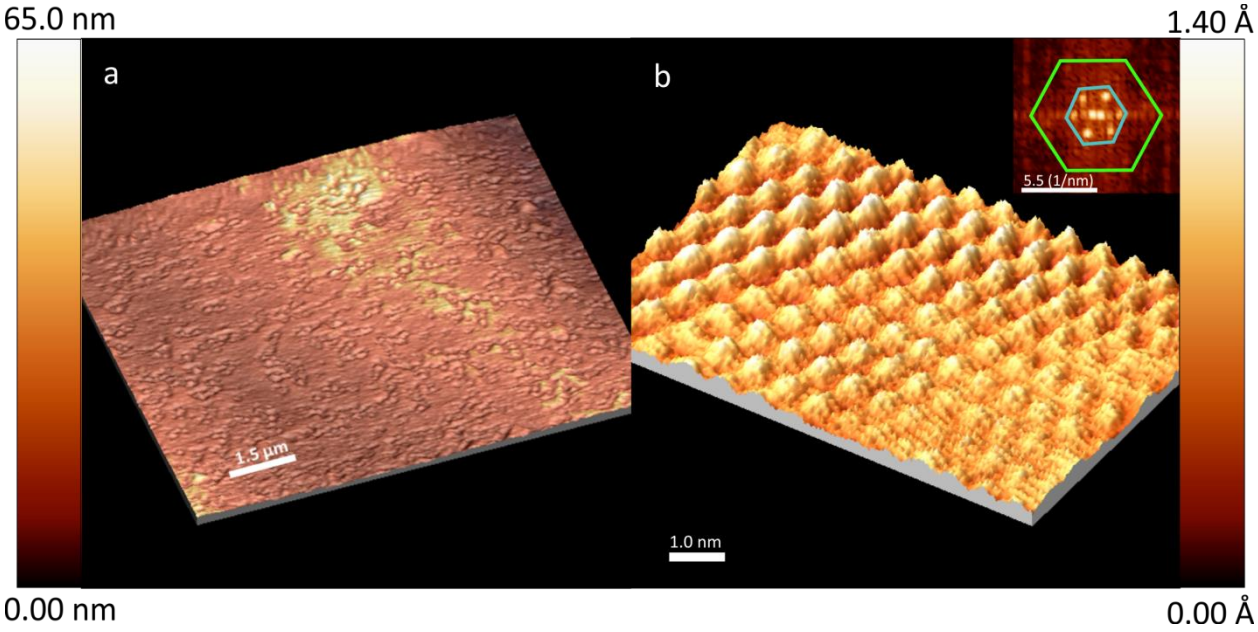

Figure 7.1: a) An AFM topographic image of the graphene/hBN/Cu system. b) 3D visualization of an STM topographic image showing Moiré patterns between the graphene and the underlying hBN; the graphene atomic resolution is visible .Inset: A Fast Fourier Transform (FFT) of the magnified area.

By measuring the perturbations caused by the moiré pattern and the top graphene layer, one can calculate the twisting angle between the graphene and the hBN layer based on *equation 3.1*. Here, the periodically of the moiré pattern is $\lambda = 0.7\ nm$. Therefore, we calculated the twisting angle between the two layered materials to be $\theta = 10.89°$.

While we were able to achieve a clean and flat sample with good adhesion between the graphene and the underlying hBN, we could not apply a gate-voltage to these samples due to the presence of a high leakage current. We believe that the observed leakage current could arise from the following three scenarios: 1) Damage caused by the etching process. 2) Poor quality of the provided hBN and 3) Due to the fragility of the hBN, once it is fixed to the sample holder with glue, this procedure by itself may damage the structural integrity of the hBN, which then causes leakage-channels to form along the device. Therefore, in our last endeavors we will focus on further optimization of the etching procedure and the use of home-grown graphene, which consists of isolated large patches of the material. Through these means we hope to substantially reduce the probability of forming a leakage current. Due to our recent progress I am confident that we will be able to produce a viable device in the near future.

Appendix A:

Optical camera calibration:

Since most of our devices use a SiO_2/Si or hBN/SiO_2/Si substrate it is crucial for us to approach the tip in a controlled manner above an area covered with graphene in order to prevent our tip from crashing into the dielectric material. Therefore, throughout the Ph.D. a high resolution ($R{\sim}50\mu m$) camera has been used in order to facilitate faster approach to the sample and revisiting high-quality areas. The coarse approach procedure in our STM is done by an Attocube based piezo (Attocube Systems AG, type: ANPz101) which is mounted with a z-scan piezo (EBL Products Inc., type: EBL #3). The lateral approach is performed by using 6 stacks of shear piezoelectric actuators (PI Ceramic GmbH, type: PAXY+ 0048) which leads to a maximal lateral resolution of $\sim 1\ \mu m$. The calibration has been done by defining the lateral movement of the tip through the camera and a set of fixed values entered into the Nanonis control system (Specs, type: SBP 5).

Figure A1 portrays the calibration process, the first row displays the initial position of the tip, then a specific value is input into the Nanonis control system and a second image is taken (2nd row), then the same value is entered to the system but to the opposite direction and a 3rd image is taken (3rd row). Therefore, we were able to correlate the approximate lateral movement of the tip with the entered values. Furthermore, one can notice the presence of two non-bonded Au/Cr pads on top of our sample that have been used for tip preparation. By this we were able to position our tip across the sample and prepare it while keeping the system isolated and at a temperature of 5K.

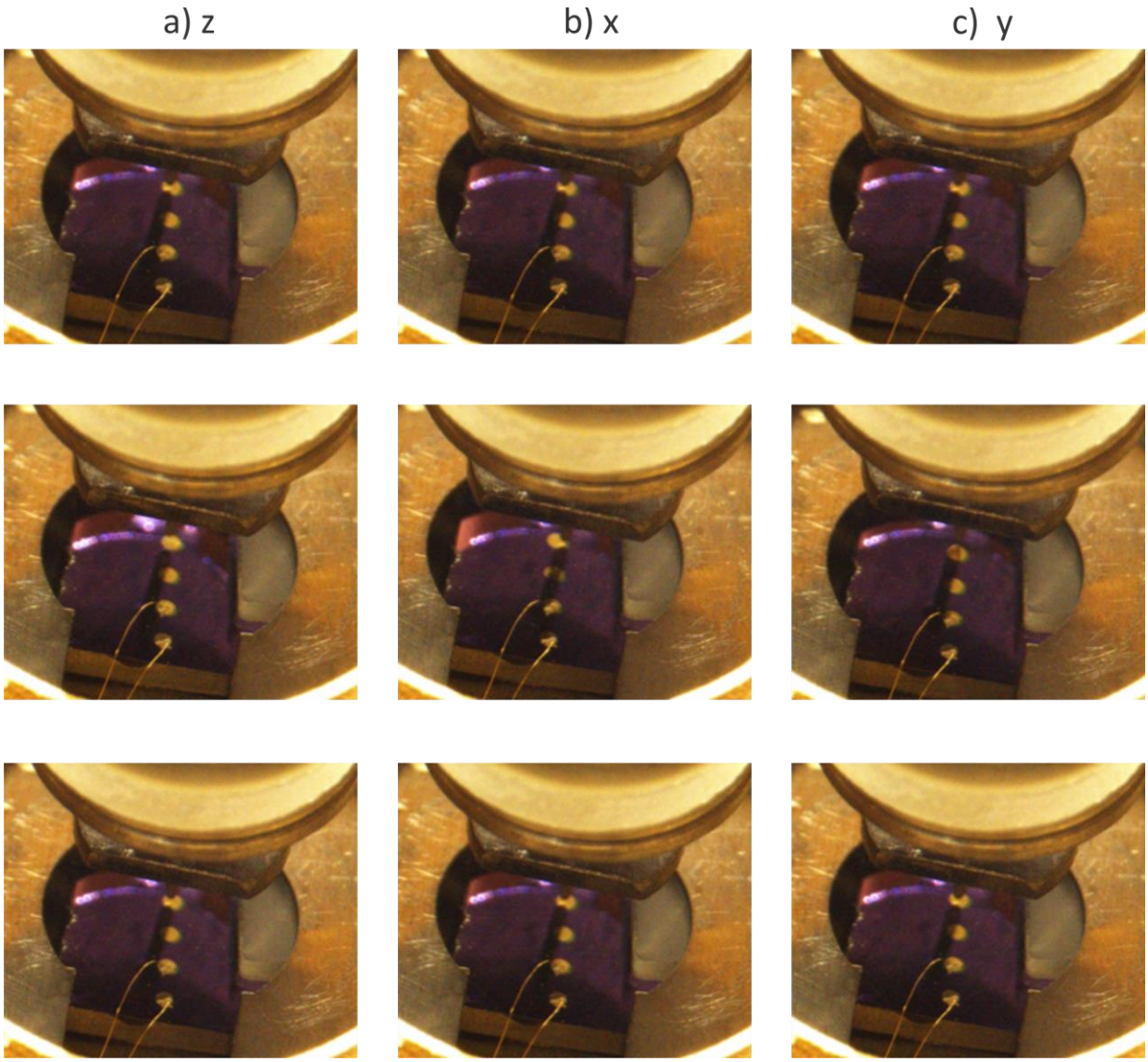

Figure A1: A set of optical images of the STM tip over the sample describing the calibration process for all three directions. a) From top to bottom. Initial position, +1000 steps and -1000 steps. Same procedure was repeated for b) the x direction and c) the y direction.

Appendix B:

Automation of the annealing process:

As it was mentioned throughout the thesis, the cleaning procedure of the G-FET devices is of outmost importance. Particularly important is the cleaning procedure performed in our preparation chamber under UHV conditions. Since the cleaning procedure in the preparation chamber is being done on the device in its final form it also includes the Au wires bonding the graphene to the bias electrode on the sample holder (as can be seen in figure A1) which can detached in the presence of a high temperature gradient. Therefore, during the annealing process one should take under consideration not only the absolute temperature of the annealing process but also the heating and cooling rates. Furthermore, since our devices are constructed from several materials with different thermal expansion coefficients, heating and cooling down the device in a non-controlled manner may induce defects and leakage current channels throughout the device. Even though the procedure can be carried out manually by a human operator the resolution of control that can be achieved with an automated system is far better. Moreover, an automated system will allow us to perform a much longer annealing procedure while maintaining a stable temperature. Therefore, a Python code has been used in order to automate the annealing procedure. Our annealing set-up is constructed of a filament and a high-voltage source which accelerates the emitted electrons towards the sample holder. Since the filament fluctuates through the measurements a constant PID feedback loop was implemented in the automation in order to maintain both the filament current and the accelerating voltage stable. Figure B1 presents our annealing apparatus and a schematic profile for both the filament current and overall temperature ramping.

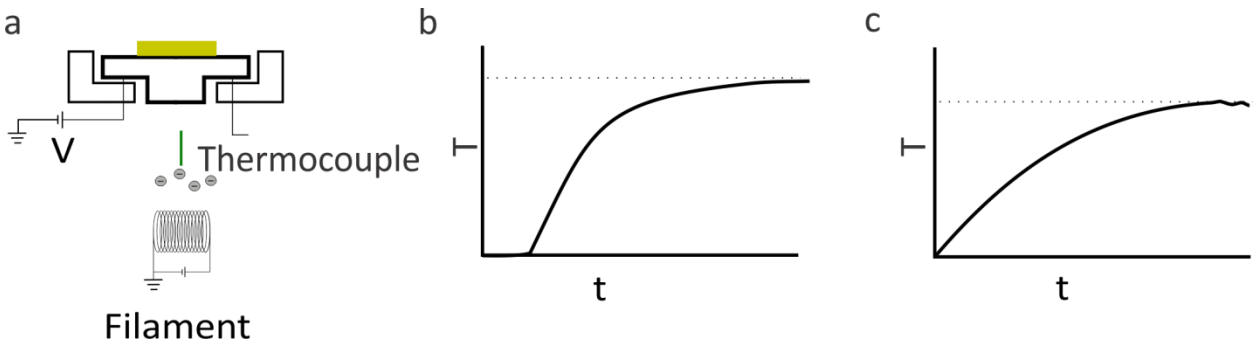

Figure B1: a) An illustration of the annealing procedure, through electron bombardment of the sample holder b) A schematic temperature profile of our system. c) A schematic current profile of the filament.

References:

(1) Mathew, P. T.; Fang, F. *Engineering* **2018**, *4*, 760.

(2) Ratner, M. *Nature Nanotechnology* **2013**, *8*, 378.

(3) Dell, E. J.; Capozzi, B.; Xia, J.; Venkataraman, L.; Campos, L. M. *Nature Chemistry* **2015**, *7*, 209.

(4) Kong, J.; Franklin, N. R.; Zhou, C.; Chapline, M. G.; Peng, S.; Cho, K.; Dai, H. *Science* **2000**, *287*, 622.

(5) McAlpine, M. C.; Agnew, H. D.; Rohde, R. D.; Blanco, M.; Ahmad, H.; Stuparu, A. D.; Goddard, W. A.; Heath, J. R. *Journal of the American Chemical Society* **2008**, *130*, 9583.

(6) Ceze, L.; Nivala, J.; Strauss, K. *Nature Reviews Genetics* **2019**.

(7) Sanvito, S. *Chemical Society Reviews* **2011**, *40*, 3336.

(8) Rocha, A. R.; García-suárez, V. M.; Bailey, S. W.; Lambert, C. J.; Ferrer, J.; Sanvito, S. *Nature Materials* **2005**, *4*, 335.

(9) Binnig, G.; Rohrer, H.; Gerber, C.; Weibel, E.; H., F. R.; L., N. *Applied Physics Letters* **1982**, *40*, 178.

(10) Binnig, G.; Rohrer, H.; Gerber, C.; Weibel, E. *Physical Review Letters* **1982**, *49*, 57.

(11) Binnig, G.; Rohrer, H. *Reviews of Modern Physics* **1987**, *59*, 615.

(12) Binnig, G.; Quate, C. F.; Gerber, C. *Physical Review Letters* **1986**, *56*, 930.

(13) Hapala, P.; Temirov, R.; Tautz, F. S.; Jelínek, P. *Physical Review Letters* **2014**, *113*, 226101.

(14) Nguyen, G. D.; Tsai, H.-Z.; Omrani, A. A.; Marangoni, T.; Wu, M.; Rizzo, D. J.; Rodgers, G. F.; Cloke, R. R.; Durr, R. A.; Sakai, Y.; Liou, F.; Aikawa, A. S.; Chelikowsky, J. R.; Louie, S. G.; Fischer, F. R.; Crommie, M. F. *Nature Nanotechnology* **2017**, *12*, 1077.

(15) Martinez-Blanco, J.; Nacci, C.; Erwin, S. C.; Kanisawa, K.; Locane, E.; Thomas, M.; von Oppen, F.; Brouwer, P. W.; Folsch, S. *Nat Phys* **2015**, *advance online publication*.

(16) Kumagai, T.; Hanke, F.; Gawinkowski, S.; Sharp, J.; Kotsis, K.; Waluk, J.; Persson, M.; Grill, L. *Nat Chem* **2014**, *6*, 41.

(17) Nacci, C.; Erwin, S. C.; Kanisawa, K.; Fölsch, S. *ACS Nano* **2012**, *6*, 4190.

(18) Stipe, B. C.; Rezaei, M. A.; Ho, W. *Science* **1998**, *280*, 1732.

(19) Stipe, B. C.; Rezaei, M. A.; Ho, W. *Physical Review Letters* **1998**, *81*, 1263.

(20) Tersoff, J.; Hamann, D. R. *Physical Review B* **1985**, *31*, 805.

(21) Alemani, M.; Peters, M. V.; Hecht, S.; Rieder, K.-H.; Moresco, F.; Grill, L. *Journal of the American Chemical Society* **2006**, *128*, 14446.

(22) Qiu, X. H.; Nazin, G. V.; Ho, W. *Physical Review Letters* **2004**, *93*, 196806.

(23) Imada, H.; Miwa, K.; Imai-Imada, M.; Kawahara, S.; Kimura, K.; Kim, Y. *Nature* **2016**, *538*, 364.

(24) Kurnosikov, O.; de Nooij, F. C.; LeClair, P.; Kohlhepp, J. T.; Koopmans, B.; Swagten, H. J. M.; de Jonge, W. J. M. *Physical Review B* **2001**, *64*, 153407.

(25) Kitaguchi, Y.; Habuka, S.; Okuyama, H.; Hatta, S.; Aruga, T.; Frederiksen, T.; Paulsson, M.; Ueba, H. *Scientific Reports* **2015**, *5*, 11796.

(26) Warshel, A.; Sharma, P. K.; Kato, M.; Xiang, Y.; Liu, H.; Olsson, M. H. M. *Chemical Reviews* **2006**, *106*, 3210.

(27) Warshel, A. *Accounts of Chemical Research* **1981**, *14*, 284.

(28) Saggu, M.; Fried, S. D.; Boxer, S. G. *The Journal of Physical Chemistry B* **2019**, *123*, 1527.

(29) Pham, V. D.; Ghosh, S.; Joucken, F.; Pelaez-Fernandez, M.; Repain, V.; Chacon, C.; Bellec, A.; Girard, Y.; Sporken, R.; Rousset, S.; Dappe, Y. J.; Narasimhan, S.; Lagoute, J. *npj 2D Materials and Applications* **2019**, *3*, 5.

(30) Zhang, Y.; Brar, V. W.; Wang, F.; Girit, C.; Yayon, Y.; Panlasigui, M.; Zettl, A.; Crommie, M. F. *Nat Phys* **2008**, *4*, 627.

(31) ionBrar, V. W.; Decker, R.; Solowan, H.-M.; Wang, Y.; Maserati, L.; Chan, K. T.; Lee, H.; Girit, C. O.; Zettl, A.; Louie, S. G.; Cohen, M. L.; Crommie, M. F. *Nat Phys* **2011**, *7*, 43.

(32) Wang, Y.; Brar, V. W.; Shytov, A. V.; Wu, Q.; Regan, W.; Tsai, H.-Z.; Zettl, A.; Levitov, L. S.; Crommie, M. F. *Nat Phys* **2012**, *8*, 653.

(33) Zhang, Y.; Brar, V. W.; Girit, C.; Zettl, A.; Crommie, M. F. *Nature Physics* **2009**, *5*, 722.

(34) Decker, R.; Wang, Y.; Brar, V. W.; Regan, W.; Tsai, H.-Z.; Wu, Q.; Gannett, W.; Zettl, A.; Crommie, M. F. *Nano Letters* **2011**, *11*, 2291.

(35) Xue, J.; Sanchez-Yamagishi, J.; Bulmash, D.; Jacquod, P.; Deshpande, A.; Watanabe, K.; Taniguchi, T.; Jarillo-Herrero, P.; LeRoy, B. J. *Nat Mater* **2011**, *10*, 282.

(36) Wong, D.; Velasco Jr, J.; Ju, L.; Lee, J.; Kahn, S.; Tsai, H.-Z.; Germany, C.; Taniguchi, T.; Watanabe, K.; Zettl, A.; Wang, F.; Crommie, M. F. *Nature Nanotechnology* **2015**, *10*, 949.

(37) Velasco, J.; Ju, L.; Wong, D.; Kahn, S.; Lee, J.; Tsai, H.-Z.; Germany, C.; Wickenburg, S.; Lu, J.; Taniguchi, T.; Watanabe, K.; Zettl, A.; Wang, F.; Crommie, M. F. *Nano Letters* **2016**, *16*, 1620.

(38) Riss, A.; Wickenburg, S.; Tan, L. Z.; Tsai, H.-Z.; Kim, Y.; Lu, J.; Bradley, A. J.; Ugeda, M. M.; Meaker, K. L.; Watanabe, K.; Taniguchi, T.; Zettl, A.; Fischer, F. R.; Louie, S. G.; Crommie, M. F. *ACS Nano* **2014**, *8*, 5395.

(39) Wickenburg, S.; Lu, J.; Lischner, J.; Tsai, H.-Z.; Omrani, A. A.; Riss, A.; Karrasch, C.; Bradley, A.; Jung, H. S.; Khajeh, R.; Wong, D.; Watanabe, K.; Taniguchi, T.; Zettl, A.; Neto, A. H. C.; Louie, S. G.; Crommie, M. F. *Nature Communications* **2016**, *7*, 13553.

(40) Mamin, H. J.; Ganz, E.; Abraham, D. W.; Thomson, R. E.; Clarke, J. *Physical Review B* **1986**, *34*, 9015.

(41) Bardeen, J. *Physical Review Letters* **1961**, *6*, 57.

(42) Tersoff, J.; Hamann, D. R. *Physical Review Letters* **1983**, *50*, 1998.

(43) Smith, D. P. E.; Binnig, G.; Quate, C. F. *Applied Physics Letters* **1986**, *49*, 1641.

(44) Lauhon, L. J.; Ho, W. *Physical Review B* **1999**, *60*, R8525.

(45) Lee, H. J.; Ho, W. *Science* **1999**, *286*, 1719.

(46) Gupta, J. A.; Lutz, C. P.; Heinrich, A. J.; Eigler, D. M. *Physical Review B* **2005**, *71*, 115416.

(47) Natterer, F. D.; Patthey, F.; Brune, H. *ACS Nano* **2014**, *8*, 7099.

(48) Lyo, I.-W.; Avouris, P. *Science* **1989**, *245*, 1369.

(49) Gaudioso, J.; Lauhon, L. J.; Ho, W. *Physical Review Letters* **2000**, *85*, 1918.

(50) Castro Neto, A. H.; Guinea, F.; Peres, N. M. R.; Novoselov, K. S.; Geim, A. K. *Reviews of Modern Physics* **2009**, *81*, 109.

(51) Novoselov, K. S.; Geim, A. K.; Morozov, S. V.; Jiang, D.; Zhang, Y.; Dubonos, S. V.; Grigorieva, I. V.; Firsov, A. A. *Science* **2004**, *306*, 666.

(52) Wallace, P. R. *Physical Review* **1947**, *71*, 622.

(53) Novoselov, K. S.; Geim, A. K.; Morozov, S. V.; Jiang, D.; Katsnelson, M. I.; Grigorieva, I. V.; Dubonos, S. V.; Firsov, A. A. *Nature* **2005**, *438*, 197.

(54) Zhang, Y.; Tan, Y.-W.; Stormer, H. L.; Kim, P. *Nature* **2005**, *438*, 201.

(55) Kim, S. M.; Hsu, A.; Araujo, P. T.; Lee, Y.-H.; Palacios, T.; Dresselhaus, M.; Idrobo, J.-C.; Kim, K. K.; Kong, J. *Nano Letters* **2013**, *13*, 933.

(56) Choi, W.; Shehzad, M. A.; Park, S.; Seo, Y. *RSC Advances* **2017**, *7*, 6943.

(57) Choi, W. J.; Chung, Y. J.; Park, S.; Yang, C. S.; Lee, Y. K.; An, K. S.; Lee, Y. S.; Lee, J. O. *Advanced Materials* **2014**, *26*, 637.

(58) Shautsova, V.; Gilbertson, A. M.; Black, N. C. G.; Maier, S. A.; Cohen, L. F. *Scientific Reports* **2016**, *6*, 30210.

(59) Ferrari, A. C.; Basko, D. M. *Nature Nanotechnology* **2013**, *8*, 235.

(60) Ferrari, A. C.; Meyer, J. C.; Scardaci, V.; Casiraghi, C.; Lazzeri, M.; Mauri, F.; Piscanec, S.; Jiang, D.; Novoselov, K. S.; Roth, S.; Geim, A. K. *Physical Review Letters* **2006**, *97*, 187401.

(61) Forbeaux, I.; Themlin, J. M.; Debever, J. M. *Physical Review B* **1998**, *58*, 16396.

(62) Bae, S.; Kim, H.; Lee, Y.; Xu, X.; Park, J.-S.; Zheng, Y.; Balakrishnan, J.; Lei, T.; Ri Kim, H.; Song, Y. I.; Kim, Y.-J.; Kim, K. S.; Özyilmaz, B.; Ahn, J.-H.; Hong, B. H.; Iijima, S. *Nature Nanotechnology* **2010**, *5*, 574.

(63) Yang, X.; Peng, H.; Xie, Q.; Zhou, Y.; Liu, Z. *Journal of Electroanalytical Chemistry* **2013**, *688*, 243.

(64) Costa, S. D.; Weis, J. E.; Frank, O.; Fridrichová, M.; Kalbac, M. *RSC Advances* **2016**, *6*, 72859.

(65) Gorbachev, R. V.; Riaz, I.; Nair, R. R.; Jalil, R.; Britnell, L.; Belle, B. D.; Hill, E. W.; Novoselov, K. S.; Watanabe, K.; Taniguchi, T.; Geim, A. K.; Blake, P. *Small* **2011**, *7*, 465.

(66) Krishna Bharadwaj, B.; Chandrasekar, H.; Nath, D.; Pratap, R.; Raghavan, S. *Journal of Physics D: Applied Physics* **2016**, *49*, 265301.

(67) Cheng, B.; Wang, P.; Pan, C.; Miao, T.; Wu, Y.; Taniguchi, T.; Watanabe, K.; Lau, C. N.; Bockrath, M. *Applied Physics Letters* **2015**, *107*, 033101.

(68) Chen, W.; Madhavan, V.; Jamneala, T.; Crommie, M. F. *Physical Review Letters* **1998**, *80*, 1469.

(69) Crommie, M. F.; Lutz, C. P.; Eigler, D. M. *Nature* **1993**, *363*, 524.

(70) Madenach, R. P.; Abend, G.; Mousa, M. S.; Kreuzer, H. J.; Block, J. H. *Surface Science* **1992**, *266*, 56.

(71) Lee, V.-J. *Science* **1966**, *152*, 514.

(72) Vanselow, R.; Howe, R. *Chemistry and Physics of Solid Surfaces VIII*; Springer Berlin Heidelberg, 1990.

(73) Shaik, S.; Mandal, D.; Ramanan, R. *Nature Chemistry* **2016**, *8*, 1091.

(74) Che, F.; Gray, J. T.; Ha, S.; Kruse, N.; Scott, S. L.; McEwen, J.-S. *ACS Catalysis* **2018**, *8*, 5153.

(75) Meir, R.; Chen, H.; Lai, W.; Shaik, S. *ChemPhysChem* **2010**, *11*, 301.

(76) Aragonès, A. C.; Haworth, N. L.; Darwish, N.; Ciampi, S.; Bloomfield, N. J.; Wallace, G. G.; Diez-Perez, I.; Coote, M. L. *Nature* **2016**, *531*, 88.

(77) Kügel, J.; Klein, L.; Leisegang, M.; Bode, M. *The Journal of Physical Chemistry C* **2017**, *121*, 28204.

(78) Liljeroth, P.; Repp, J.; Meyer, G. *Science* **2007**, *317*, 1203.

(79) Kumagai, T.; Hanke, F.; Gawinkowski, S.; Sharp, J.; Kotsis, K.; Waluk, J.; Persson, M.; Grill, L. *Physical Review Letters* **2013**, *111*, 246101.

(80) Ladenthin, J. N.; Grill, L.; Gawinkowski, S.; Liu, S.; Waluk, J.; Kumagai, T. *ACS Nano* **2015**, *9*, 7287.

(81) Böckmann, H.; Liu, S.; Mielke, J.; Gawinkowski, S.; Waluk, J.; Grill, L.; Wolf, M.; Kumagai, T. *Nano Letters* **2016**, *16*, 1034.

(82) Ladenthin, J. N.; Frederiksen, T.; Persson, M.; Sharp, J. C.; Gawinkowski, S.; Waluk, J.; Kumagai, T. *Nat Chem* **2016**, *8*, 935.

(83) Auwarter, W.; Seufert, K.; Bischoff, F.; Ecija, D.; Vijayaraghavan, S.; Joshi, S.; Klappenberger, F.; Samudrala, N.; Barth, J. V. *Nat Nano* **2012**, *7*, 41.

(84) Henkelman, G.; Uberuaga, B. P.; Jónsson, H.; H., E. *The Journal of Chemical Physics* **2000**, *113*, 9901.

(85) Giannozzi, P.; Andreussi, O.; Brumme, T.; Bunau, O.; Buongiorno Nardelli, M.; Calandra, M.; Car, R.; Cavazzoni, C.; Ceresoli, D.; Cococcioni, M.; Colonna, N.; Carnimeo, I.; Dal Corso, A.; de Gironcoli, S.; Delugas, P.; DiStasio, R. A.; Ferretti, A.; Floris, A.; Fratesi, G.; Fugallo, G.; Gebauer, R.; Gerstmann, U.; Giustino, F.; Gorni, T.; Jia, J.; Kawamura, M.; Ko, H. Y.; Kokalj, A.; Küçükbenli, E.; Lazzeri, M.; Marsili, M.; Marzari, N.; Mauri, F.; Nguyen, N. L.; Nguyen, H. V.; Otero-de-la-Roza, A.; Paulatto, L.; Poncé, S.; Rocca, D.; Sabatini, R.; Santra, B.; Schlipf, M.; Seitsonen, A. P.; Smogunov, A.; Timrov, I.; Thonhauser, T.; Umari, P.; Vast, N.; Wu, X.; Baroni, S. *Journal of Physics: Condensed Matter* **2017**, *29*, 465901.

(86) Schlapbach, L.; Züttel, A. In *Materials for Sustainable Energy*, p 265.

(87) Tozzini, V.; Pellegrini, V. *Physical Chemistry Chemical Physics* **2013**, *15*, 80.

(88) Deng, S.; Berry, V. *Materials Today* **2016**, *19*, 197.

(89) Long, F.; Yasaei, P.; Sanoj, R.; Yao, W.; Král, P.; Salehi-Khojin, A.; Shahbazian-Yassar, R. *ACS Applied Materials & Interfaces* **2016**, *8*, 18360.

(90) Natterer, F. D.; Patthey, F.; Brune, H. *Physical Review Letters* **2013**, *111*, 175303.

(91) Critchley, A. D. J.; Hughes, A. N.; McNab, I. R. *Physical Review Letters* **2001**, *86*, 1725.

(92) Wang, H.; Li, S.; He, H.; Yu, A.; Toledo, F.; Han, Z.; Ho, W.; Wu, R. *The Journal of Physical Chemistry Letters* **2015**, *6*, 3453.

(93) Li, S.; Yu, A.; Toledo, F.; Han, Z.; Wang, H.; He, H. Y.; Wu, R.; Ho, W. *Physical Review Letters* **2013**, *111*, 146102.

(94) Persson, B. N. J.; Baratoff, A. *Physical Review Letters* **1987**, *59*, 339.

(95) Baratoff, A.; Persson, B. N. J. *Journal of Vacuum Science & Technology A* **1988**, *6*, 331.

(96) Henwood, D.; Carey, J. D. *Physical Review B* **2007**, *75*, 245413.

(97) Kim, S. M.; Hsu, A.; Park, M. H.; Chae, S. H.; Yun, S. J.; Lee, J. S.; Cho, D.-H.; Fang, W.; Lee, C.; Palacios, T.; Dresselhaus, M.; Kim, K. K.; Lee, Y. H.; Kong, J. *Nature Communications* **2015**, *6*, 8662.

(98) Britnell, L.; Gorbachev, R. V.; Jalil, R.; Belle, B. D.; Schedin, F.; Katsnelson, M. I.; Eaves, L.; Morozov, S. V.; Mayorov, A. S.; Peres, N. M. R.; Castro Neto, A. H.; Leist, J.; Geim, A. K.; Ponomarenko, L. A.; Novoselov, K. S. *Nano Letters* **2012**, *12*, 1707.

Acknowledgements:

In the following part I would like to thank all the people that contributed to my work and made this whole experience as special as it was:

First and foremost I am very grateful to my thesis advisor Prof. Klaus Kern who gave me the opportunity to work in the *Nanoscale department* at the Max Planck Institute for Solid State Research in Stuttgart, Germany. In that, I had the opportunity to work in the Precision Lab, which allowed me to perform experiments at the best conditions possible.

I am thankful to Prof. Jürgen Brugger, Prof. Harald Brune, Prof. Thomas Weitz, and Dr. Takashi Kumagai for being part of my thesis committee.

I am especially thankful to the people of the Gate-STM subgroup which I was part of in the last 4 years and who contributed to the success of our subgroup. Special thanks to Dr. Soon Jung Jung who was my group leader, gave me good scientific input and engaged me in numerous discussions. I am glad to have had the chance to work with Dr. Christian Dette who introduced me to our STM system. I also want to thank Tobias Wollandt and Katharina Polyudov for the friendly atmosphere at the Gate-STM and their support and help during our joint projects.

I am grateful for my collaborators from the theory group of Prof. Fabian Pauly from the University of Konstanz, Dr. Dongzhe Li and Maxim Skripnik for their excellent work and fertile discussions. On the same note I would also like to thank the group of Prof. Christian Ochsenfeld from LMU, specifically Dr. Jörg Kussmann for their help in my final project.

I would also want to thank the non-scientific staff that helped me tremendously throughout the years and allowed me to perform my research. I want to name Wolfgang Stiepany, Peter Andler and Marko Memmler. I would like to specially thank Sabine Birtel, without your support and guidance I would have not survived the Journey.

I was blessed to have worked in a great and supportive atmosphere where everyone is always willing to help and engaged in lively scientific discussions. For this I want to thank my office mates who were not only colleagues for me but also friends: Dr. Anna Roslawska, Tomasz Michnowicz, Dr. Matthias Muenks, Abhishek Grewal and Haonan Huang. I also want to thank Alessio Scavuzzo for the hours upon hours we spend in and out of the clean room and for the rest of the amazing people at the Max Planck Institute that inspired, helped, and motivated me over the years.

I would also want to acknowledge the support and willingness of the senior scientists in my department that bestowed me with their knowledge and helped me whenever they could, namely Dr. Klaus Kuhnke, Dr. Christian Ast, Dr. Markus Etzkorn, Dr. Markus Ternes, Dr. Marko Burghard, Dr. Robert Drost and Dr. Christopher Leon, thank you all.

Special thanks are in place for Dr. Rico Gutzler and Dr. Jacob Senkpiel, your support and guidance throughout my thesis both as friends and as scientists were eminent, and lay the foundations for friendships that I am sure will last for years to come.

Last but not least, I would like to thank my family and friends for the support throughout the years. In particular, I would like to thank my parents, your support, encouragement and education have made me the man I am today (for good and for worse) therefore I owe it all to you, *Besababa mevarech Shai*!

Stuttgart, June 2019

Curriculum Vitae

Name: Shai Mangel

Nationality: Israeli, Romanian.

E-mail: s.mangel@fkf.mpg.de

Education

- **2015-2019:** Ph.D., Material science, the Department of Materials Science and Engineering, Specializing in Solid State Physics, EPFL (École polytechnique fédérale de Lausanne), Switzerland. Title: *Gate-tunable Scanning Tunneling Microscope as a tool for performing single-molecule chemistry*. Supervisor: Prof. Klaus Kern.

- **2012-2014:** MSc., Physical Chemistry, the Department of Chemistry, Ben-Gurion University of the Negev, Beer-Sheva, Israel. Title: *A 3D characterization of a CdSe\CdS single particle.* Supervisor: Dr. Maya Bar-Sadan.

- **2009-2012:** Bachelor of Science, the Department of Chemistry, specializing in Physical Chemistry and Nano Chemistry, Ben-Gurion University of the Negev, Beer-Sheva, Israel.

Professional experience

- **2015-2019: Research Assistant in the department of Prof. Klaus Kern,** Solid State Science, The department of Nanoscale Science, Max-Planck Institute for Solid State Research, Stuttgart, Germany**.**

- **2014-2015: Research Assistant in the laboratory of Prof. Maya Bar-Sadan,** Physical Chemistry, the Department of Chemistry, Faculty of Natural Sciences, Ben-Gurion University of the Negev, Beer-Sheva, Israel.

- **2011-2012: Undergraduate Research Assistant in the laboratory of Prof. Maya Bar-Sadan,** Physical Chemistry, the Department of Chemistry, Faculty of Natural Sciences, Ben-Gurion University of the Negev, Beer-Sheva, Israel.

- **2010-2011: Undergraduate Research Assistant in the laboratory of Prof. Ehud Pines,** Physical Chemistry, the Department of Chemistry, Faculty of Natural Sciences, Ben-Gurion University of the Negev, Beer-Sheva, Israel.

Awards and fellowships

- *Summer Research Program Scholarship for Academic Excellent Students*, Ben- Gurion University of the Negev, 2012.

- *Dean of Natural Sciences Excellence Award for M.Sc. Students for Academic and Research Accomplishments,* Ben- Gurion University of the Negev, 2014.

Publications

1. **Mangel, S.;** Wollandt, T.; Kussmann, J.; Scavuzzo, A.; Burghard, M.; Jung, S.J.; Ochsenfeld, C.; Kern, K.; *Control over the bond length of molecular hydrogen on GFET through graphene charging.* (In preparation)

2. **Mangel, S.;** Skripnik, M.; Polyudov, K.; Dette, C.; Punke, P.; Li, D.; Urcuyo, R.; Pauly, F.; Jung, S.J.; Kern, K.; *Electric-field control of single-molecule tautomerization.* (submitted)

3. Dette, C.; Pérez-Osorio, M.A.; **Mangel, S.;** Giustino, F.; Jung, S.J.; Kern, K.; *Trellises of Molecular Oxygen on Anatase TiO_2(101)*. (submitted)

4. Scavuzzo, A.; **Mangel, S.;** Park, J.H; Lee, S.; Duong, D.L.; Strelow, C; Mews, A.; Burghard, M; Kern, K; *Electrically tunable quantum emitters in an ultrathin graphene–hexagonal boron nitride van der Waals heterostructure. Appl. Phys. Lett.* (114, 062104 , 2019)

5. Dette, C; Pérez-Osorio, M.A.; **Mangel, S.;** Giustino, F.; Jung S.J.; Kern, K.; *Atomic Structure of Water Monolayer on Anatase TiO_2(101) Surface. J. Phys. Chem. C* (122, 22, 11954-11960, 2018)

6. Dette, C; Pérez-Osorio, M.A.; **Mangel, S.;** Giustino, F.; Jung S.J.; Kern, K.; *Single-Molecule Vibrational Spectroscopy of H_2O on Anatase TiO_2 (101). J. Phys. Chem. C* (121 , 2, 1182-1187, 2017)

7. **Mangel, S.;** Houben, L.; Bar-Sadan, M.; *The effect of atomic disorder at the core–shell interface on stacking fault formation in hybrid nanoparticles. Nanoscale,* (8, 17568-17572, 2016)

8. Aronovitch, E.; Kalisman, P.; **Mangel, S.;** Houben, L.; Amirav, L.; Bar-Sadan, M.; *Designing Bimetallic Co-catalysts: A Party of Two. J. Phys. Chem. Lett.* (6, 3760-4, 2015)

9. **Mangel, S.;** Houben, L.; Bar-Sadan, M.; *Revealing Growth Schemes of Nanoparticles in Atomic Resolution: Mapping Stacking Fault Formation and Distribution. Crystal Growth & Design,* (7, 15, 3114-3118, 2015)

10. **Mangel, S.;** Aronovitch, E.; Enyashin, A.; Houben, L.; Bar-Sadan, M.; *Atomic-scale evolution of a growing core-shell nanoparticle. JACS,* (36, 136, 12564-12567, 2014)